CR-168190
PWA 5891-18

SENSOR FAILURE DETECTION FOR JET ENGINES
FINAL REPORT

by

E. C. Beattie (PWA-CPD)
R. F. LaPrad (PWA-CPD)
M. M. Akhter (SCT)
S. M. Rock (SCT)

May 1983

Commercial Engineering
Pratt & Whitney
United Technologies Corporation

Prepared for

NATIONAL AERONAUTICS AND SPACE ADMINISTRATION
Lewis Research Center
Contract NAS3-23282

Page Intentionally Left Blank

TABLE OF CONTENTS

TABLE OF CONTENTS

LIST OF FIGURES

LIST OF FIGURES

LIST OF FIGURES

LIST OF FIGURES

LIST OF FIGURES

LIST OF FIGURES

LIST OF FIGURES

LIST OF TABLES

LIST OF TABLES

SECTION 1

SUMMARY

The objective of this program was to develop refinements to the sensor failure detection, isolation and accommodation (DIA) algorithm developed under NASA Contract NAS3-22481, "Sensor Failure Detection System". Participants in the program were the Commercial Products Division of Pratt & Whitney Aircraft Group, and Systems Control Technology (SCT), Inc., with sponsorship provided by NASA Lewis Research Center.

Refinements were developed for the simplified non-linear F100 engine simulation, which is used as a model for the filter in the DIA algorithm, to improve the algorithm's transient accuracy over the flight envelope. A stand-alone non-proprietary version of the simplified non-linear simulation was also developed.

Three potential revisions to the DIA algorithm were evaluated relative to their ability to minimize or eliminate the effect of estimation biases and to improve detection, isolation, and accommodation performance. The selected revision feeds back the estimator outputs to the linear regulator portion of the control all the time. In the case of no failures, the sensor outputs are fed to the integral control. When a sensor failure occurs, the estimate of the failed parameter is fed back to the integral portion. In the course of making the refinements, an underlying goal was to reduce the algorithm's complexity, where possible, for future implementation on NASA's microprocessor system.

The resulting revised DIA algorithm was evaluated over the flight envelope on the non-linear F100 dynamic simulation. The evaluation showed that the improved DIA algorithm eliminated the estimation error with no failures induced while improving the capability to detect, isolate, and accommodate sensor failures.

SECTION 2

INTRODUCTION

The "Sensor Failure Detection System for Jet Engines" program, NASA Contract NAS3-23282, developed refinements to the sensor failure detection, isolation and accommodation (DIA) algorithm developed under NASA Contract NAS3-22481, "Sensor Failure Detection System" program. This included refinements to improve accuracy of the simplified non-linear engine model used in the filter for the DIA algorithm. The DIA algorithm itself was revised to eliminate the effect of filter biases on steady state operating point accuracy.

This follow-on program was conducted by a team consisting of Pratt & Whitney Aircraft Commercial and Government Products Divisions and Systems Control Technology Inc., (SCT) of California, with Pratt & Whitney Aircraft Commercial Products Division (CPD) being the prime contractor. Figure 2-1 shows the team members' primary responsibilities for this program. The program consisted of three technical tasks; Task I - "Simplified Simulation Refinement" described in Section 3, Task II - "Detection, Isolation, and Accommodation Algorithm Improvement" described in Section 5, and Task III - "Non-Linear Simulation Evaluation" described in Section 6.

Under the "Sensor Failure Detection System" Program (NAS3-22481), which was completed in August 1981 [1], the applicability of advanced detection, isolation, and accommodation concepts to sensor failure detection for gas turbine engine control systems was demonstrated. The configuration of the engine with the multivariable control and the fault detection logic is shown in Figure 2-2. Five advanced concepts were evaluated for detecting, isolating, and accommodating sensor failures. A screening process led to the selection of an advanced concept (summarized in Table 2-1) that uses a steady state Kalman filter to generate residuals for failure detection. The weighted sum squared residual (WSSR) technique was used to detect soft failures, Likelihood Ratio testing of a bank of steady state Kalman filters (each designed with one input missing) was used for isolation, and reconfiguring of the normal mode Kalman filter by eliminating the failed input was used to accommodate the failure. The detection, isolation, and accommodation (DIA) concept is shown in Figure 2-3. This program utilized the F100 engine simulation and F100 Multivariable Control (MVC) logic developed under the F100 Multivariable Control System program (Air Force contract F33615-75-C-2053) [2,3], as the test bed system for concept evaluation.

The estimation filters employed in the detection, isolation, and accommodation concept required the implementation of a dynamic model of the engine. In the referenced program, simplified linear engine models were developed based upon sixteenth order linear models which were available from the F100 Multivariable Control System program. A set of steady state Kalman filter gain matrices were designed based upon these linear models. Curve fits of the coefficients of the linear model matrices and filter gain matrices were then calculated to provide continuous operation of the model and filters throughout the flight envelope. The curve-fit set of linear models resulted in a simplified non-linear model.

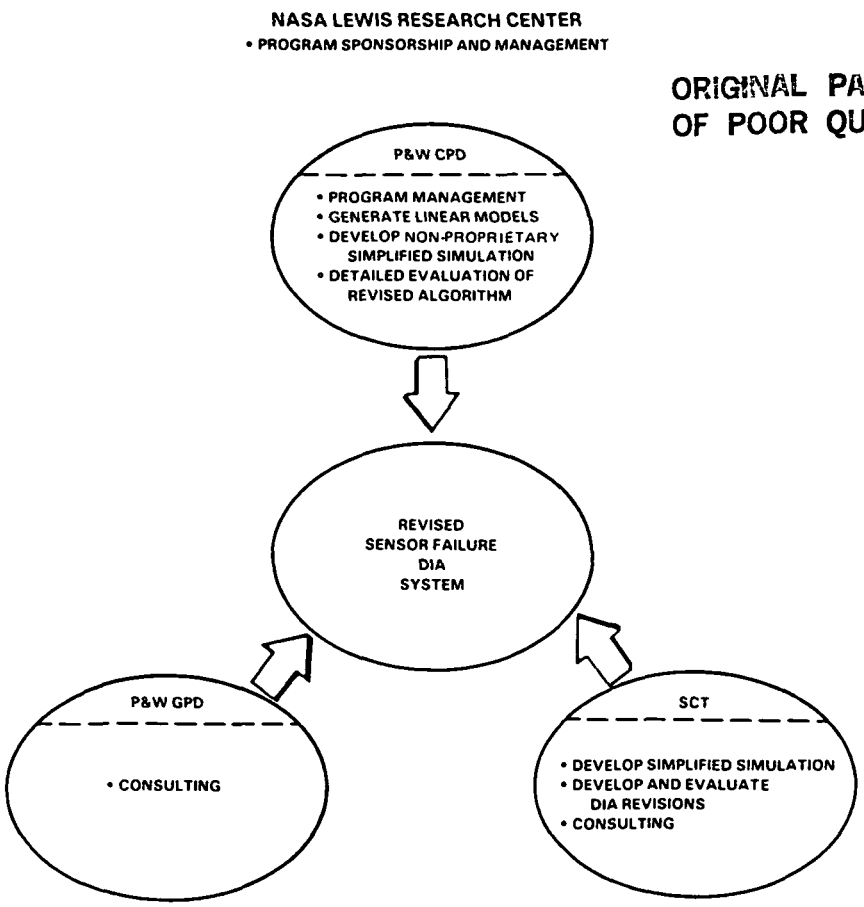

Figure 2-1 Team Members and Primary Responsibilities

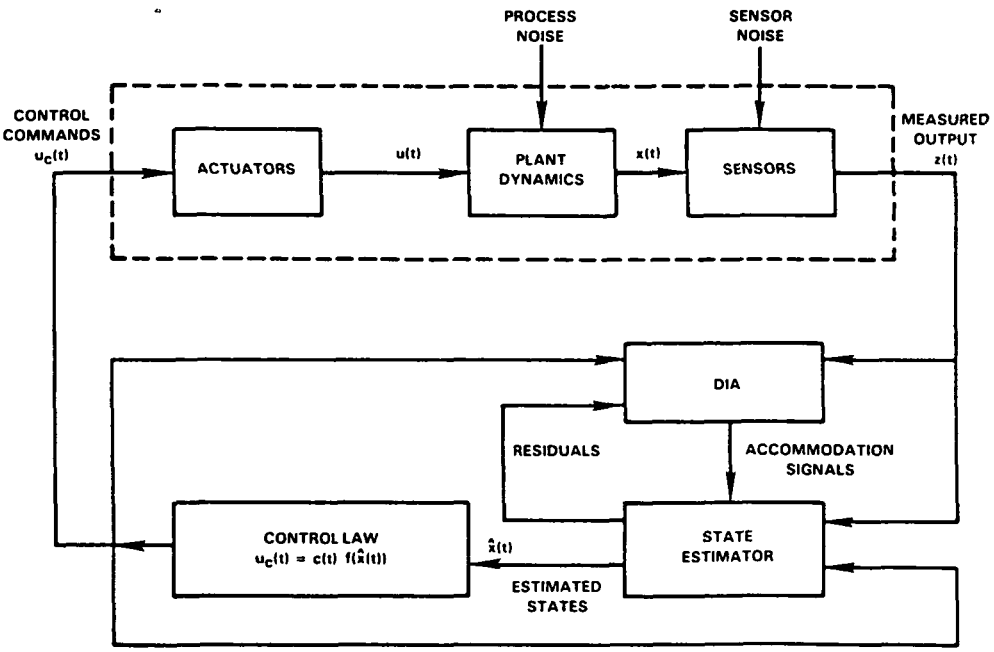

Figure 2-2 Generalized Block Diagram of Failure Detection, Isolation, and Accommodation Logic

TABLE 2-1

ADVANCED CONCEPT FOR DETECTING, ISOLATING, AND ACCOMMODATING SENSOR FAILURES

Detection	-	Innovations testing based on a Weighted Sum-Squared Residual (WSSR) technique for soft failures. Innovations testing against thresholds for hard failures.
Isolation	-	On-line isolation of hard failures using innovations testing; off-line isolation (Logic only activated after detection occurs) of soft failures using a Generalized Likelihood Ratio testing technique. A bank of Kalman filters is employed for off-line isolation.
Accommodation	-	Reconfiguration and reinitialization of normal mode filter.

The Final Report on NASA Contract NAS3-22481 [1] describes the results of the detailed evaluation of the detection, isolation and accommodation concept. While the performance of the advanced concept was generally good and its feasibility demonstrated, several problem areas were identified. These problems included steady state and dynamic mismatch of the simplified non-linear model; steady state estimate errors with no failures induced; instabilities when accommodating failures; accommodation inaccuracies; and missed detections and false alarms. These problems were addressed in the follow-on program as noted below.

Linear models of the F100 engine were generated at 109 flight operating points. The specific flight operating points were selected to be sufficient to ensure that the linear models completely define engine operation throughout the flight envelope. Functional relationships between the linear model coefficients were developed to create a simplified non-linear simulation of the F100 engine. This simplified simulation was validated by comparing its operation to that of the non-linear F100 simulation. The simplified non-linear simulation was delivered to NASA-LeRC. A detailed discussion of the simplified simulation development is included in Section 3.

Potential revisions to the DIA algorithm were developed to correct the algorithm deficiencies identified in the referenced contract. Three potential algorithm revisions were evaluated to arrive at a modified design which eliminates the steady state estimation errors with no failures induced (Section 5.1). The three revisions are summarized below:

Revision 1 The sensor values are fed back to the control algorithm in the case of no failures. When a failure occurs, the appropriate estimator output will be substituted.

Revision 2 The estimator outputs are fed back all the time to the linear regulator portion of the control mode. In the case of no failure, the sensor outputs are fed to the integral control, but in case of a failure the appropriate estimator output is fed back in place of the failed sensor.

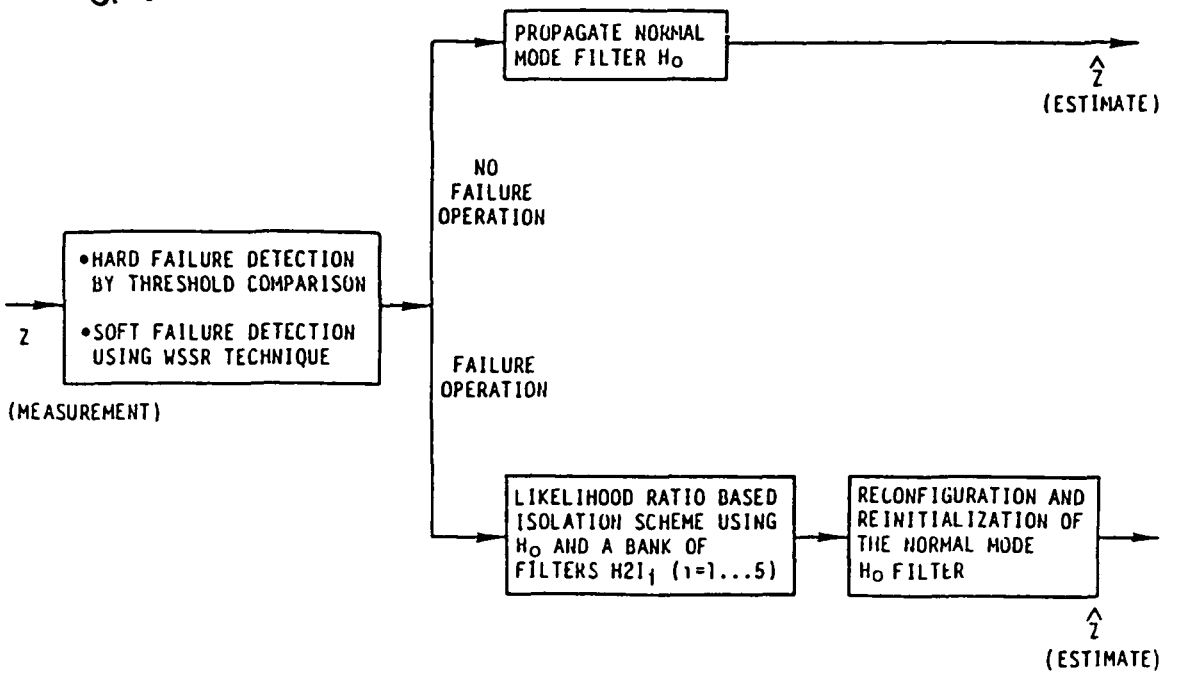

Figure 2-3 Detection, Isolation, and Accommodation Concept

Revision 3 The estimator outputs are fed back all of the time to both the proportional (LQR) and integral portions of the control. A supplementary trim logic (integrator) is implemented in the DIA algorithm to eliminate bias errors in estimator outputs.

Revisions 1 and 2 were judged to be equal in complexity, whereas Revision 3 was considered to be of much greater complexity because of the additional integrators and associated integral trim logic. All three DIA revisions were judged to be equal in their ability to eliminate the steady state hang-off errors for the no-failure case. The three DIA revisions also exhibited comparable detection, isolation and accommodation performance. However, Revision 2 generally exhibited less transient upset after a failure was induced, particularly for slow drifts. It was, therefore, decided to incorporate Revision 2 in the DIA algorithm for non-linear simulation evaluation during Task III. The results of this evaluation are presented in Section 5.3.

The DIA algorithm, modified with Revision 2, was further modified to incorporate the new simplified non-linear simulation to improve the algorithm's dynamic accuracy. This revised algorithm was then evaluated at 15 flight operating points using the non-linear F100 simulation. Comparisons to the baseline DIA algorithm (developed under Contract NAS3-22481) and parameter synthesis technique were made where data from similar flight and failure conditions existed from the previous contract. The revised algorithm was shown to eliminate the steady state hang off errors for the no-failure case and provide equal or better DIA capability to the algorithm developed in the referenced contract. The results of this comparison are presented in Section 6.

SECTION 3

3.0 DEVELOPMENT OF IMPROVED SIMPLIFIED NON-LINEAR SIMULATION

The filters employed in the detection, isolation,and accommodation (DIA) concept require the implementation of a dynamic model of the engine. The simplified model of the engine used for the DIA algorithm is shown in a block diagram on Figure 3-1 and is described by the following equations;

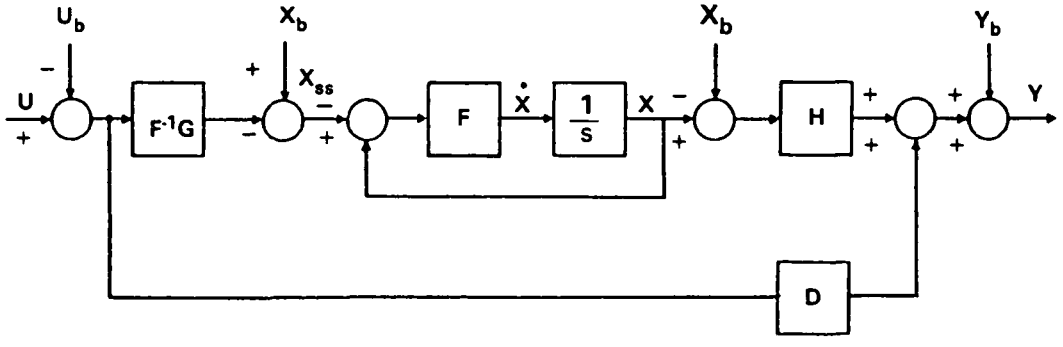

Figure 3-1 Simplified Nonlinear Model Implementation

$$\dot{X} = F(X - X_{ss}) \tag{1}$$

$$Y = Y_b + H(X - X_b) + D(U - U_b) \tag{2}$$

where

$$X_{ss} = X_b - F^{-1}G(U - U_b) \tag{3}$$

In these equations, the state derivative, $\dot{X}$, is being driven by the "distance" the state, X, is from its steady state value, X_{ss}. The subscript, b, denotes a base point obtained from the original steady state operating line data.

This model looks much like a linear model. Note, however, that the model matrices (F, $F^{-1}G$, H and D) are functions of the operating condition as are the base points (X_b, U_b, and Y_b). For full flight envelope operation, the matrices used are formed by scheduling linear model matrices throughout the flight envelope.

In the previous program, simplified fourth order linear models were developed using a limited number of sixteenth order linear models which were available from the F100 Multivariable Control System program (Air Force Contract F33615-75-C-2053). A set of Kalman filter gain matrices were designed based upon these fourth order linear models. Curve fits of the coefficients of the models and filters were then calculated to provide continuous operation of the models and filters throughout the flight envelope. The curve-fit set of linear models resulted in a simplified non-linear model.

While performance of the combined filter/model algorithm was quite good at the lower altitude and Mach number flight conditions, some problems of steady state and transient mismatch were encountered at higher altitudes and Mach numbers. The transient mismatch was found to result from not having a sufficient number of the original linear models available to constrain the curve fitting procedure for the matrix elements at these flight conditions to obtain a good accuracy of fit. The steady state mismatch resulted primarily from inaccuracies in the model base point schedules. Even though the Kalman filters worked well in minimizing these mismatches, the effectiveness of the detection, isolation, and accommodation algorithm was reduced at these flight conditions. Additional work was required to improve the transient accuracy of the model. This was the goal of Task I of this program.

The Task I effort involved generation of a set of linear engine models for the F100 engine, and development of a simplified non-linear simulation by developing functional relationships for model coefficients that span a typical flight envelope. The systematic procedure used to achieve this is outlined in Figure 3-2. This procedure will be discussed in the following paragraphs.

3.1 Selection of Flight Operating Points

The first task in developing the simplified non-linear simulation was to define a set of flight operating points at which to generate linear models of the F100 engine using the non-linear deck. The ground rule used to select the flight operating points was to determine which points are required to adequately span a typical flight envelope such that any functional relationships for simulation parameters are accurate for operation throughout the flight envelope.

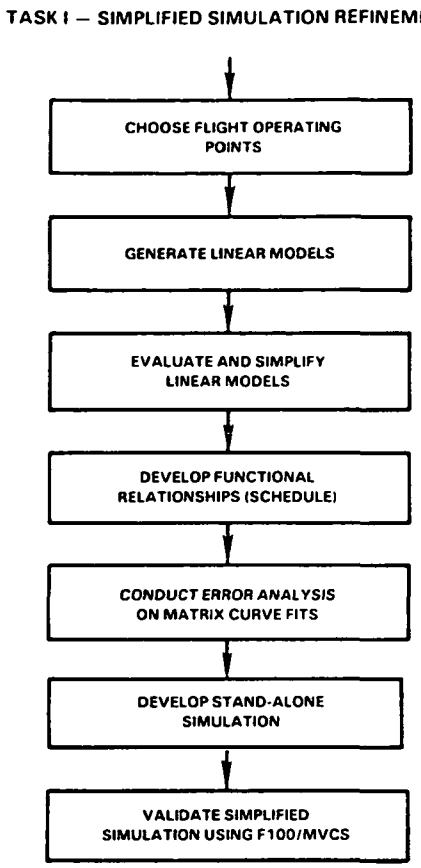

Figure 3-2 Simplified Simulation Refinement Procedure

In the previous program (NASA-22481) the flight point data was obtained from the Air Force document AFAPL-TR-76-74, "F100 Multivariable Control System - Engine Models/Design Criteria," dated November 1976 [4]. Sixteenth order linear models at these points were available from the F100/MVCS program. These were reduced to fourth order models and used in the simplified F100 simulation. The flight operating points are plotted on Altitude/Mach number and PT2/TT2 (engine inlet pressure and temperature) diagrams shown in Figures 3-3 and 3-4. Figure 3-3 shows that the data points span the flight envelope adequately. However, when evaluating the data points relative to the PT2/TT2 relationship on Figure 3-4, a high concentration of points are evident at the lower PT2/TT2 conditions. The distribution over the remaining flight envelope is inadequate. The high concentration of models on the PT2/TT2 diagram coincide with the flight conditions where the performance of the original simplified non-linear model was acceptable.

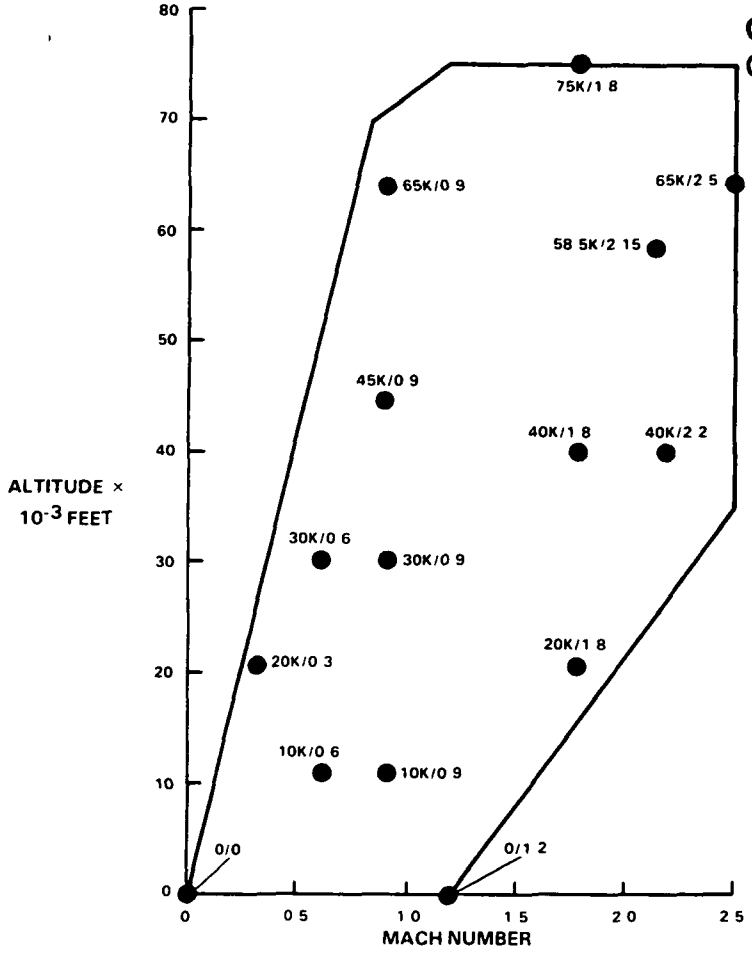

Figure 3-3 F100 Flight Envelope With Old Data Points

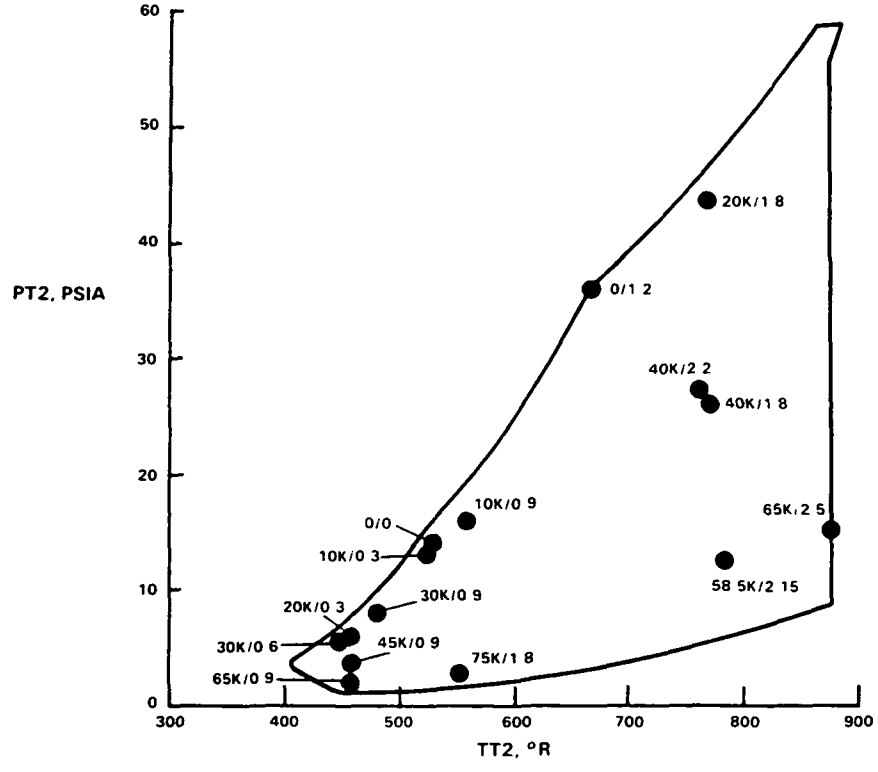

Figure 3-4 F100 Flight Envelope With Old Data Points

TABLE 3-1

SELECTED FLIGHT POINTS

Altitude (ft)	Mach No.	PLA (deg)
0.0	0.0	24., 36., 52., 67., 83.
0.0	1.2	60., 70., 83.
10000.0	0.3	20., 56., 83.
10000.0	0.75	20., 36., 52., 67., 83.
15000.0	1.25	60., 74., 83.
15000.0	1.6	74., 83.
20000.0	0.75	20., 36., 52., 67., 83.
20000.0	1.5	74., 83.
20000.0	1.9	74., 83.
25000.0	1.75	74., 83.
28000.0	1.25	60., 74., 83.
30000.0	0.6	24., 36., 67., 83.
30000.0	2.0	74., 83.
32000.0	2.2	74., 83.
35000.0	0.8	20., 36., 52., 67., 83.
35000.0	1.6	74., 83.
35000.0	2.2	74., 83.
35000.0	2.5	74., 83.
41000.0	2.20	74.0
41000.0	2.0	83.0
41000.0	2.3	74., 83.
42500.0	1.8	74., 83.
42500.0	2.2	74., 83.
45000.0	0.9	24., 40., 52., 67., 83.
45000.0	2.5	74., 83.
49000.0	2.3	74., 83.
50000.0	1.3	74., 83.
50000.0	1.8	74., 83.
50000.0	2.3	74., 83.
52500.0	0.65	20., 36., 52., 67., 83.
55000.0	2.1	74., 83.
56000.0	2.0	74., 83.
59000.0	2.0	74., 83.
65000.0	1.2	60., 74., 83.
65000.0	1.8	74., 83.
65000.0	2.5	74., 83.
70000.0	0.85	20., 36., 52., 67., 83.
70000.0	2.1	74., 83.
75000.0	1.2	60., 74., 83.
75000.0	2.3	74., 83.
75000.0	2.5	74., 83.

The relative location of the flight points on the PT2/TT2 envelope was felt to be a definite consideration in the selection process. Therefore flight operating points were selected which span both the altitude/Mach number and PT2/TT2 flight envelopes. A total of 109 points were selected as tabulated on Table 3-1 and illustrated on Figures 3-5 and 3-6 relative to the Altitude/Mach number and PT2/TT2 diagrams, respectively.

3.2 Generation of Linear Models

Fourth order linear models of the F100 engine were generated at the 109 selected flight operating points using the non-linear F100 simulation. The linear models generated are composed of a set of matrices (F, $F^{-1}G$, G, H and D) generated at each flight point and are defined in the following state space equations:

$$\delta \dot{X} = F \delta X + G \delta U \quad (4)$$

$$\delta Y = H \delta X + D \delta U \quad (5)$$

where X is a 4 x 1 state vector, U is a 5 x 1 input vector, and Y is a 7 x 1 output vector. These vectors are defined in Table 3-2.

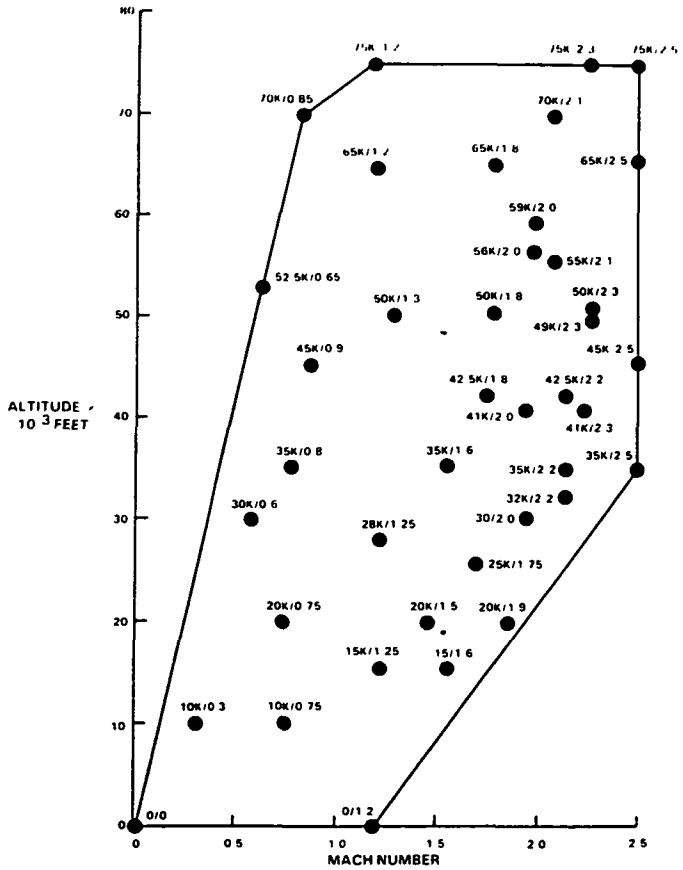

Figure 3-5 Selected Data Points on Alt/M Flight Envelope

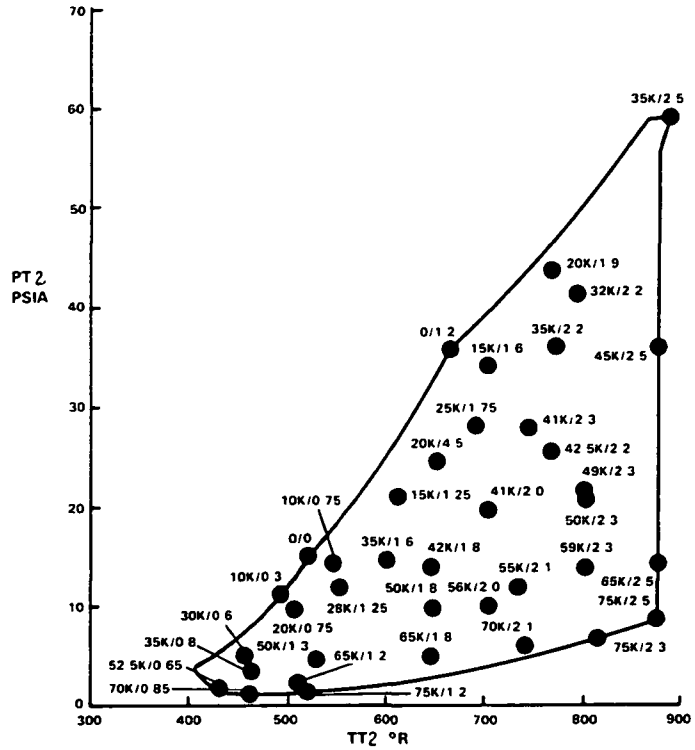

Figure 3-6 Selected Data Points on PT2/TT2 Flight Envelope

TABLE 3-2

ENGINE VARIABLES USED IN REDUCED ORDER MODELS

1. Engine State Variables

X_1 = Fan Speed, SNFAN (N_1) - rpm

X_2 = Compressor Speed, SNCOM (N_2) - rpm

X_3 = Burner Exit Slow Response Temperature, T_{t4lo} - °R

X_4 = Fan Turbine Inlet Slow Response Temperature, $T_{t4.5lo}$ - °R

2. Engine Inputs

U_1 = Main Burner Fuel Flow, WFMB - lb/hr

U_2 = Nozzle Jet Area, Aj - ft^2

U_3 = Compressor Inlet Variable Vane, CIVV-deg

U_4 = Rear Compressor Variable Vane, RCVV-deg

U_5 = Compressor Bleed Flow, BLC - %

3. Engine Outputs

Y_1 = Fan Speed, SNFAN (N_1) - rpm
Y_2 = Compressor Speed, SNCOM (N_2) - rpm
Y_3 = Burner Pressure, PT4 - psia
Y_4 = Augmentor Pressure, PT6 - psia
Y_5 = Fan Turbine Inlet Temperature, FTIT - °R
Y_6 = Engine Thrust, FNMX - lb
Y_7 = Compressor Surge Margin, SMHC %

The model matrices were generated by two different methods at the selected flight operating points. These two methods calculate the matrices as follows.

(i) Method 1: In this method, matrices F and H are generated using an "offset derivative technique" wherein biases are introduced to each element of the state vector (x) at a steady state point. The resulting steady state changes in the output (y) and state derivative ($\dot{x}$) are observed and are used to determine F and H directly, as shown below, without exercising the simulation transiently. Figure 3-7 shows a block diagram of this technique.

$$F_{ij} = \frac{\delta \dot{x}_i}{bx_j} \tag{6}$$

$$H_{ij} = \frac{\delta y_i}{bx_j} \tag{7}$$

where bx_j is the perturbation in the jth element of the x vector.

The $F^{-1}G$ matrix is generated by introducing biases in the control vector and converging the simulation to steady state; i.e., $\dot{x}$ equal to 0.0. For this situation equation (5) can be written as

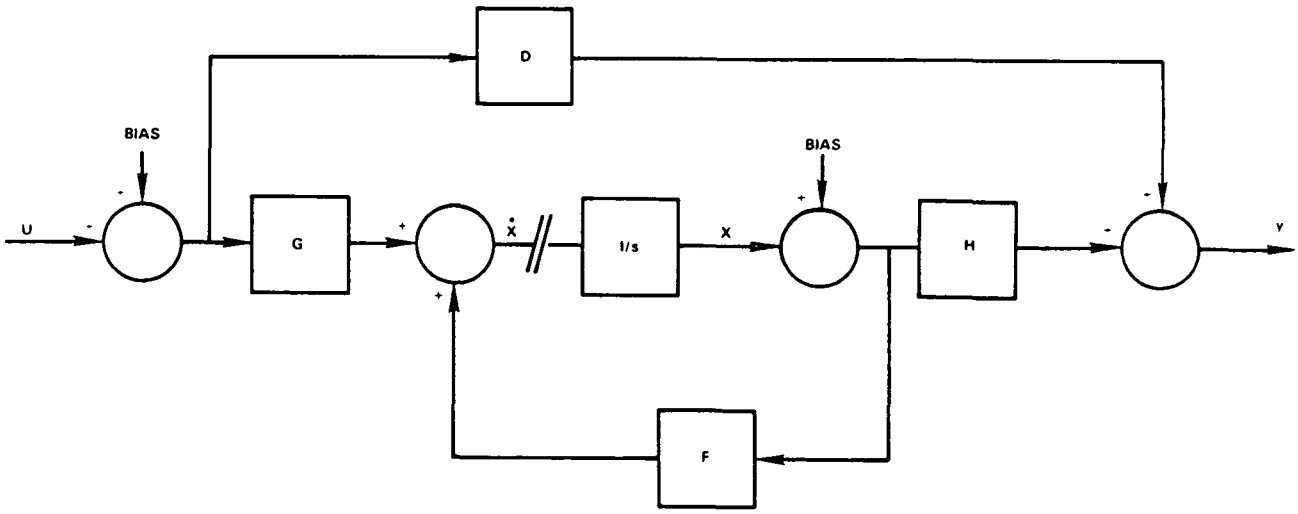

Figure 3-7 Linear Model Generation by the Offset Derivative Technique

$$\dot{\delta X} = o = F\delta x + Gb_u$$

$$(-F^{-1}G)_{ij} = \frac{1}{b_{u_j}} \delta x_i \qquad (8)$$

where bu_j is the perturbation in the jth element of the u vector.

Similarly $\delta Y = H\delta X + Db_u$

$$= H(-F^{-1}G)b_u + Db_u$$

$$= (D - HF^{-1}G)\, b_u$$

$$(D - HF^{-1}G)_{ij} = \frac{1}{b_{u_j}} \delta y_i \qquad (9)$$

Using the F, H and $F^{-1}G$ matrices, the G and D matrices can be computed as follows:

$$G = -(F)\ (-F^{-1}G) \qquad (10)$$

$$D = (D - H\,F^{-1}G) - (H)\ (-F^{-1}G) \qquad (11)$$

(ii) Method 2: In this method the G and D matrices are also generated directly using the "offset derivative technique" with biases introduced to each element of the control vector (u) at a steady state point. The $F^{-1}G$ matrix is computed from F and G. In addition to equations (6) and (7), the following equations apply for this method.

$$G_{ij} = \frac{\delta \dot{x}_i}{bu_j} \qquad (12)$$

$$D_{ij} = \frac{\delta y_i}{bu_j} \qquad (13)$$

After evaluating the two methods, it was decided to use the matrices generated directly; i.e., F, G, H, and D from method 2 and $F^{-1}G$ from method 1.

3.3 Transient Performance of the Linear Models

The transient performance of several linear models was compared for a step input in PLA against the detailed nonlinear F100 simulation. Figures 3-8 to 3-10 show the transient responses of fan speed (N1), compressor speed (N2), burner pressure (PT4) and augmentor pressure (PT6) at the following flight points.

(i) alt = 0 ft., Mach No = 0.0, PLA = 52.0 degrees to 52.5 degrees (step)
(ii) alt = 0 ft., Mach No = 0.0, PLA = 52.0 to 57.0 degrees (step)
(iii) alt = 30000,ft, Mach No. = 0.6, PLA = 24.0 degrees to 24.5 degrees (step)

The linear models were perturbed with the control variable transients generated by the nonlinear simulation of the F100 engine and multivariable control system. Small perturbation transient characteristics of the linear models are in good agreement with the nonlinear simulation. Differences in the steady state base points result from differences in steady state reference schedules between the Multivariable Control System simulation and the F100 simulation used to generate the linear models.

3.4 Simplification of Linear Model Matrices

In order to implement a simplified nonlinear model based upon the individual linear models, polynomial curve fits of each model matrix element were developed. Prior to developing these curve fits, the matrix data was analyzed to determine what simplifications could be implemented which would result in the simplest polynomial curve fits. This simplification was accomplished in two ways. First matrix data was analyzed to determine which elements were insignificant and could either be zeroed or set to a constant value. Second, correction factors such as θ [(inlet total temperature)/(standard day temperature)], and δ [(inlet total pressure)/(14.7)] were applied to matrix elements and potential bias variables to reduce data scatter.

In order to determine which matrix elements were insignificant; i.e., their contribution to system static and dynamic performance is negligible, the matrices were first nondimensionalized. This was accomplished by dividing each incremental quantity by its corresponding base point value. For example, the H_{23} element of the H matrix was nondimensionalized as follows.

$$H_{23\ \text{nondimensional}} = H_{23} * X_{b3}/Y_{b2} \qquad (14)$$

The nondimensionalized set of matrices represent sensitivities in percent and are independent of the magnitude and range of values over which states x, inputs u and outputs y vary. By applying a simple threshold check on respective elements of all matrices, relatively small magnitude elements were identified. For example the F24 and F34 elements of the F matrix were found to be on the order of 10^{-3} to 10^{-4} (except at very few flight points) whereas other elements were generally in the range of 10^{+1} to 10^{-1}. Therefore F24

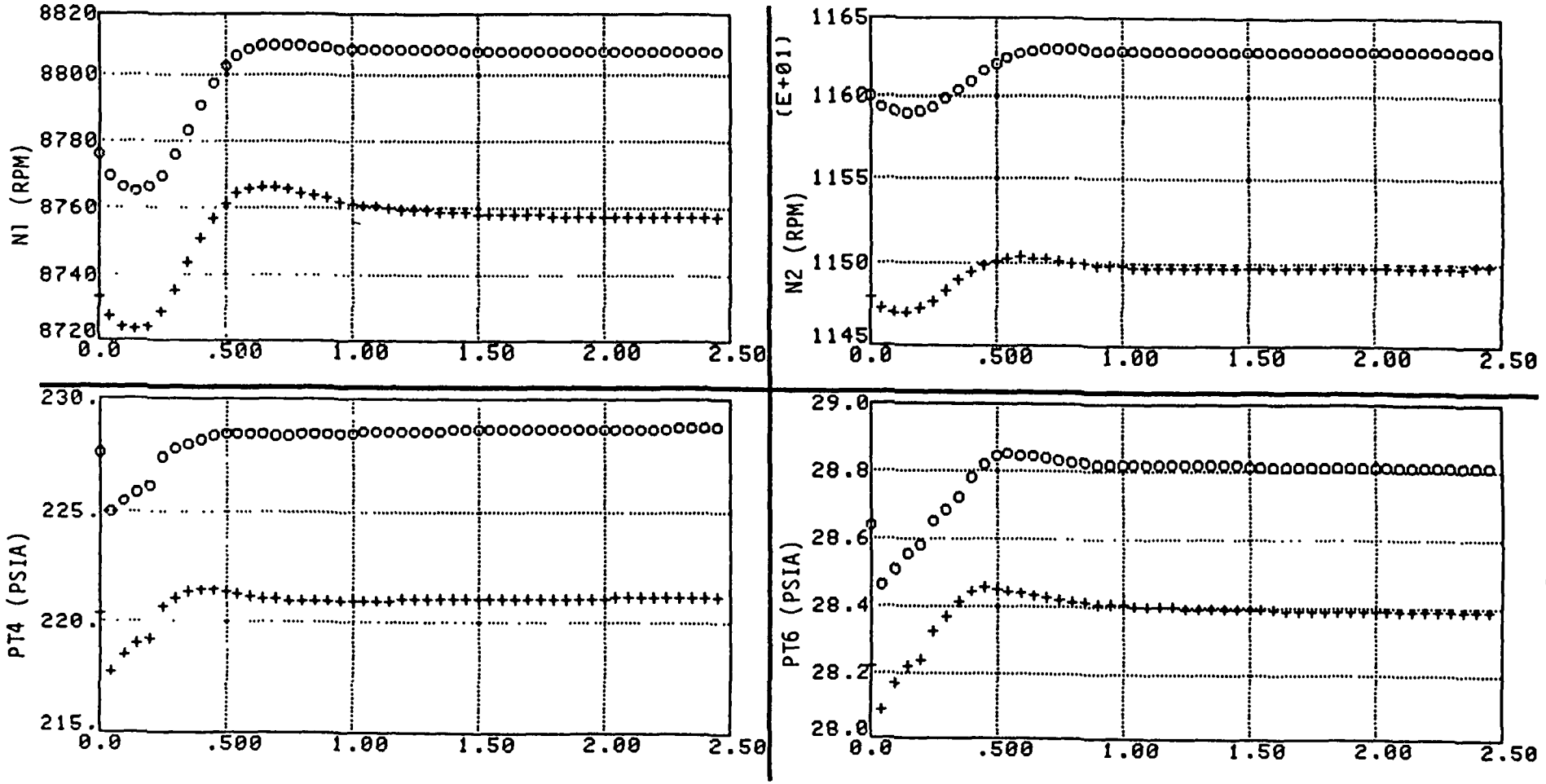

Figure 3-8 Small Perturbation Transient Response of the Linear Model at 0/0/52 (++++) Linear Model (oooo) Non-Linear Model (PLA size: 52.0 Degrees to 52.5 Degrees)

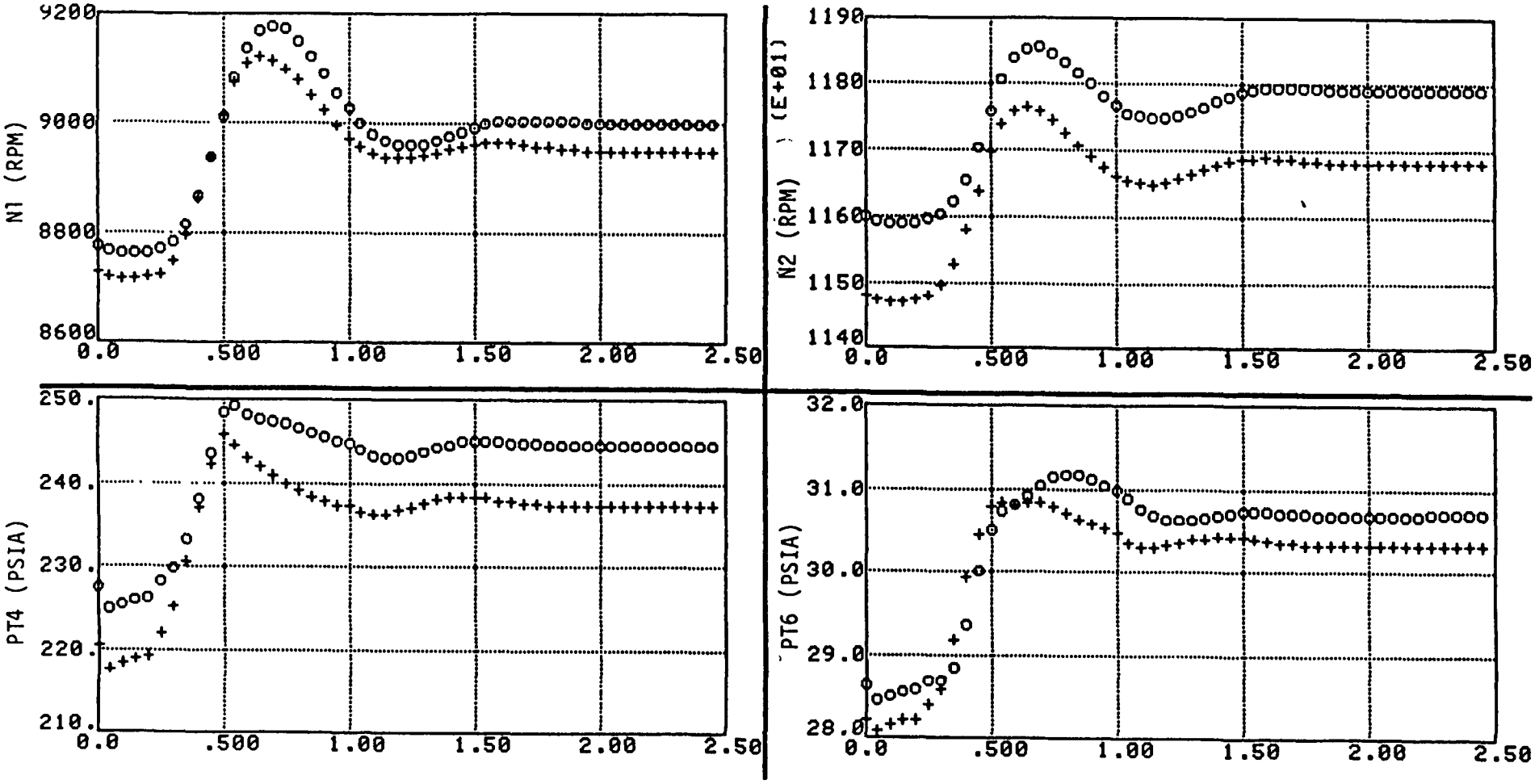

Figure 3-9 Small Perturbation Transient Response of the Linear Model at 0/0/52 (++++) Linear Model (oooo) Non-Linear Model (PLA size: 52.0 Degrees to 57.0 Degrees)

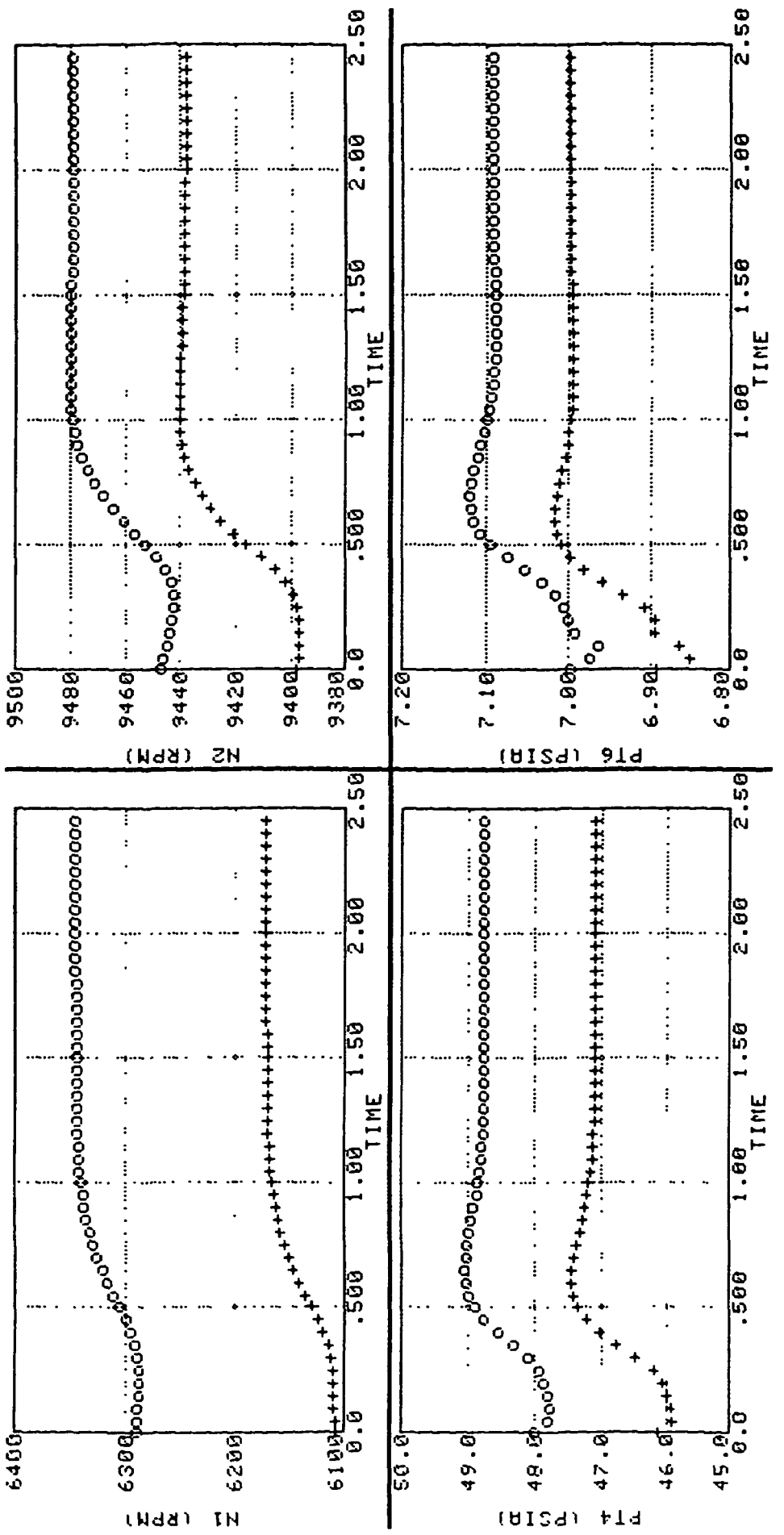

Figure 3-10 Small Perturbation Transient Response of the Linear Model at 30K/0.6/24 (++++) Linear Model (oooo) Non-Linear Model (PLA step: 24.0 Degrees to 24.5 Degrees)

and F34 were identified as small and could either be made zero or replaced by the mean of all 109 points. The matrix elements identified to be small are:

F24, F34,
H73, H54, H74
D44, D64

The above mentioned matrix elements were made constant in the development of the simplified engine model.

A sensitivity analysis of the eigensystem to the elements of the F matrix was also performed. The elements F13, F43, F24 and F34 had negligible effect on the eigensystem. Thus, implementation of these matrix elements as constants will have no adverse effect on the system transient behavior.

Application of temperature and pressure correction factors to matrix elements and potential bias parameters for curve fits was accomplished with a computer program which operated on the data and provided plots for visual inspection. It was observed from the point plots of the model data, that application of the correction factors tends to reduce the spread (scatter) of the matrix elements with changing flight condition. Figures 3-11 and 3-12 present examples of matrix element point plots with no correction factors and with the correction factors respectively. The "corrected" data gives improved functional relationships and was used in the development of the polynomial curve fits discussed in Section 3.5.

3.5 CURVE-FITTING OF MODEL MATRIX ELEMENTS

Polynomial schedules of the model matrices F, $F^{-1}G$, H and D were developed for use in the full envelope simplified nonlinear model of the F100 engine. The point plots of the linear model data, with correction factors applied, were studied for selection of the variables with which the matrix elements show a functional relationship. A polynomial function was generated for each matrix element of the F, F^{-1} G, H and D matrices using a leaps and bounds subset regression technique [5]. This regression analysis resulted in the polynomial curve fits for the matrix elements shown in Tables 3-3a through 3-3d.

3.6 ERROR ANALYSIS OF MODEL MATRIX CURVE FITS

The error analysis approach taken was to plot the matrix elements computed from the full envelope model against the actual value of the corresponding matrix element. Data with correction factors applied (both real data and matrix data) was used for this error analysis. For a perfect regression model the model points would lie on a line of 45° slope ($y = \hat{y}$). If the regression model is not perfect these model points will be distributed around the 45° slope line. A measure of the goodness of the fit can be obtained using the sample correlation coefficient R, and standard deviation of the model errors. Figures 3-13a through 3-13f present plots of F11, F21, F12, F22, F33, and F44 matrix elements with a 45° slope line and 1σ and 2σ bands around it. It is clear from Figures 3-13a through 3-13f that most model points lie within a 1σ band of the regression model and most certainly within 2σ.

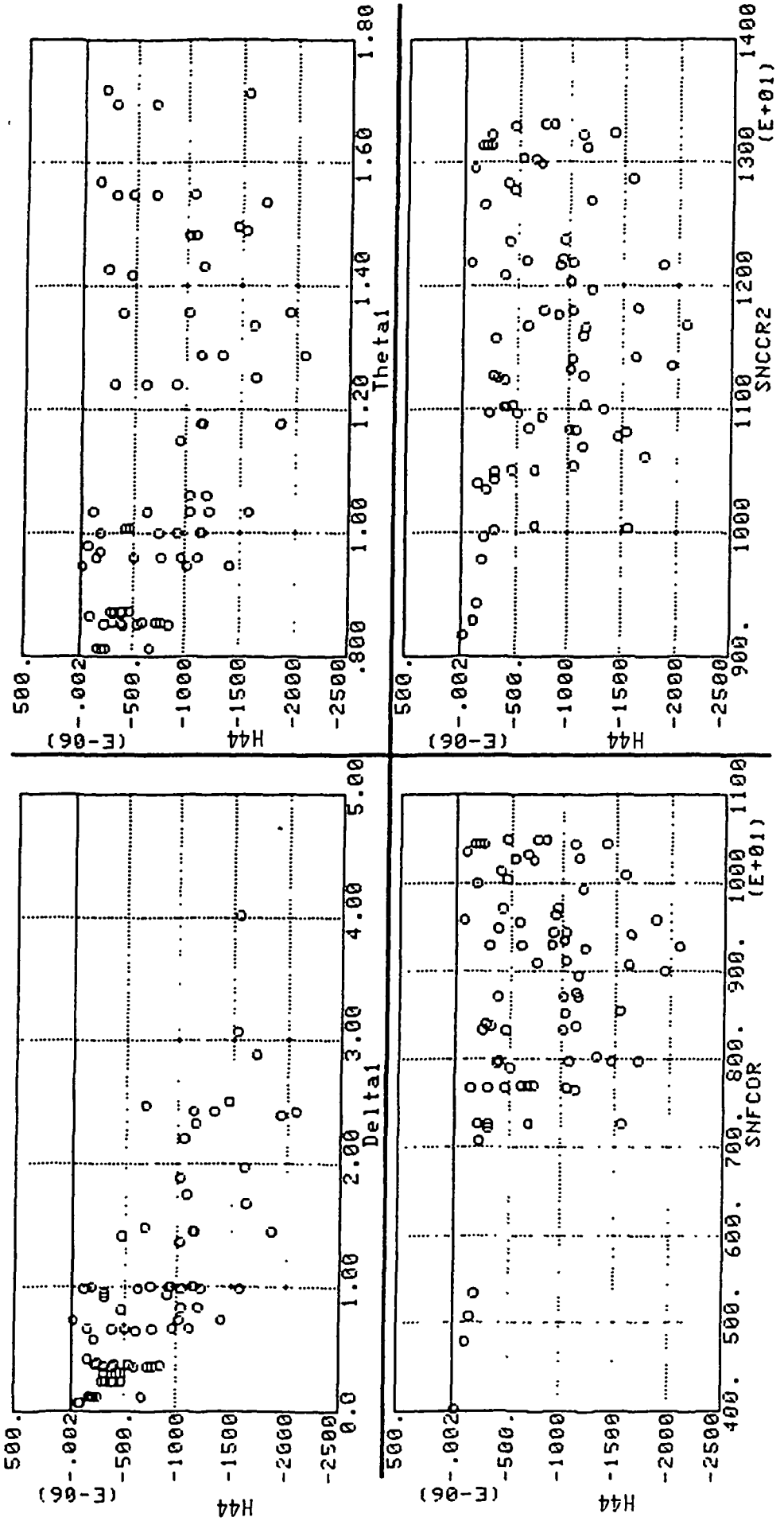

Figure 3-11 Point Plot of H_{44} Element With No Correction Factor

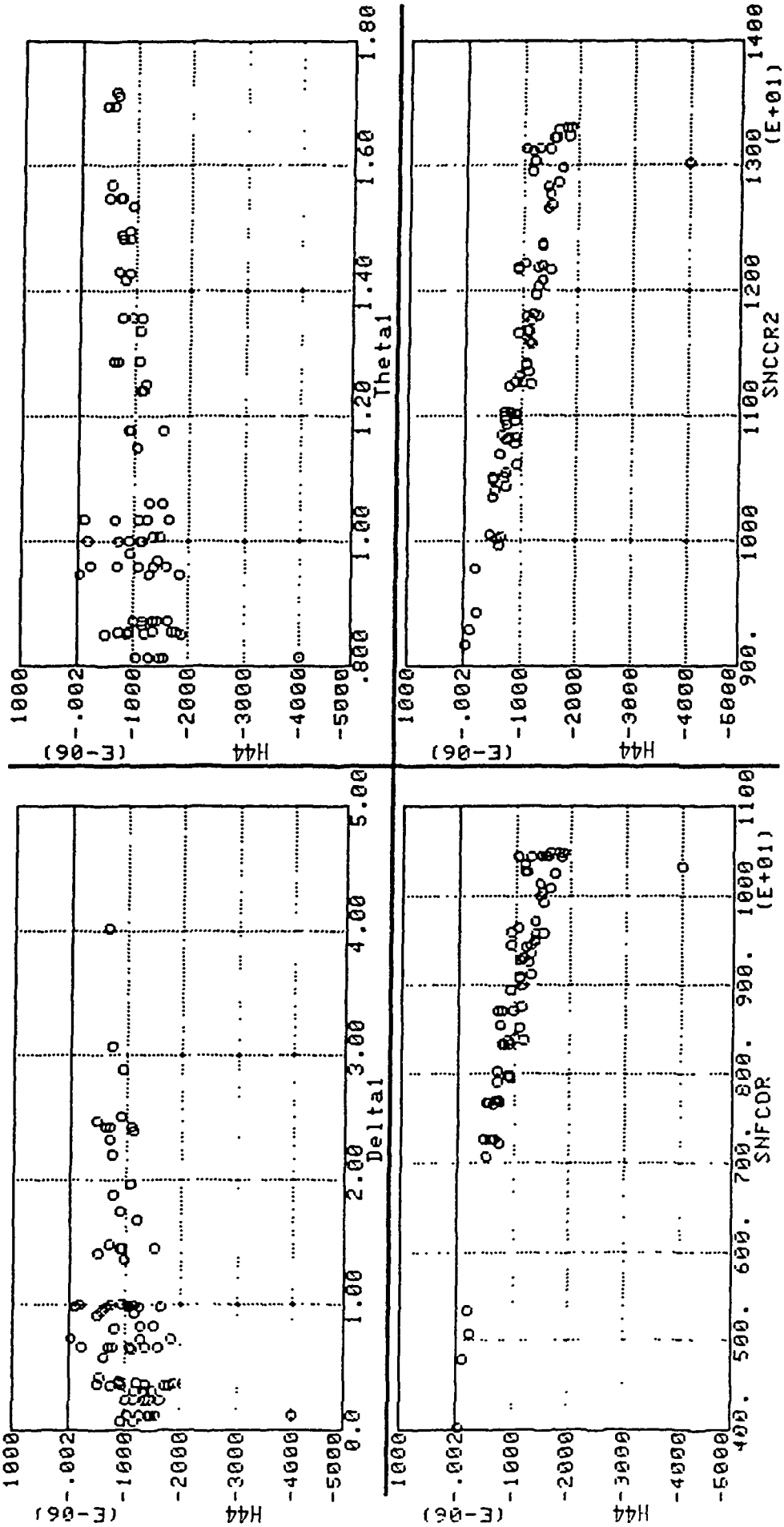

Figure 3-12 Point Plot of H44 Element Corrected with Theta (TT2/518.6°R) divided by Delta (PT2/14.7) Correction Factor

TABLE 3-3a
FULL ENVELOPE MODEL OF F MATRIX

```
F(1,1) = -0 9683E-1/DL1-0 1886E-2*XPT6**2-2 463
F(2,1) = -0 1820E-3*XN1+0 2768E-9*XPT6*XN1**2+0 7721
F(3,1) = -0 2201E-2*XPT6+0 8295E-4*XTT45-0 8207E-1
F(4,1) =  0 6353E-2/DL1+0. 1038E-8*XPT4**3-0 2724E-1
F(1,2) = -0. 2596E+1*TH1+0. 8159E-1/DL1+5 78
F(2,2) = -0 2381E+1/TH1-0 2348E-7*XN1**2+1 549
F(3,2) = -0 4095E-2*DL1-0 8174E-2/DL1+0 1212E-1
F(4,2) = -0 1010E-1*DL1-0 2312E-1/DL1+0 2996E-1
F(1,3) = -1 597
F(2,3) = -0. 1569/DL1+0 2382E-1*XPT4+4 2890
F(3,3) = -0 6377/DL1+0 5218/TH1-0 5229
F(4,3) = -0 1156
F(1,4) = -0 1143/DL1+0 8349E-7*XN1**2+1 074
F(2,4) =  0 6013E-1
F(3,4) =  0. 2632E-2
F(4,4) = -0 1914E+1/DL1+0 1564E+1/TH1-1 568
```

TABLE 3-3b
FULL ENVELOPE MODEL OF $F^{-1}G$ MATRIX

```
FIG(1,1) =  0. 9327E-3*XN1-0. 3145E-11*XN1**3-6 56
FIG(2,1) = -0 3616*TH1-0. 3850E+8/XN1**2+0 4541
FIG(3,1) =  0. 1183E-3*XPT4-0 363E-9*XPT4**3-0 372E-1
FIG(4,1) =  0. 9333E-3*XPT6-0 9744E-9*XN1*XPT6**2-0 306E-1
FIG(1,2) = -0. 2971E+2*XPT6+0 2182E+2/(TH1*DL1)-260 4
FIG(2,2) =  0 1121*XN1-0 1545E-2*XPT4*XPT6**2-721 8
FIG(3,2) =  0 5845E-1*XPT4-0 7198E-4*XPT4*XPT6**2-1 568
FIG(4,2) =  0 3761*XPT6-0 5675E-4*XPT4*XPT6**2-1 418
FIG(1,3) =  0 1627*XPT4-0 4133E-4*XPT4*XPT6**2-2 104
FIG(2,3) = 0 275*XPT6-6. 304
FIG(3,3) =  0 1306E-1*XPT6-0 2379
FIG(4,3) =  0 1068E-1*XPT6-0 1881
FIG(1,4) =  0 8670E+1/TH1+0 5090E-1*XPT4-26 19
FIG(2,4) =  0 1168E+3*TH1+0 1092E+3/TH1-220 7
FIG(3,4) =  0 2010*TH1-0. 1262E-2*XPT4+0 2459
FIG(4,4) =  0 9386E-1*TH1-0 1157E-2*XPT4+0 2951
FIG(1,5) =  0 5357E+4/(DL1*RTH1)-75 87
FIG(2,5) =  0 3754E+4/(DL1*RTH1)+157 9
FIG(3,5) = -0 9392E+2*(RTH1/DL1)-0 7399E+1*(TH1/DL1**2)+8 53
FIG(4,5) = -0 8524E+2*(RTH1/DL1)-0 5902E+1*(TH1/DL1**2)+9 7
```

TABLE 3-3c
FULL ENVELOPE MODEL OF H MATRIX

```
H(1,1) =  1
H(2,1) =  0
H(3,1) = -0 2814E+1/XPT4-0 2378E-5*XPT4*XPT6+0 4341E-1
H(4,1) = -0 5318/XPT4-0 4950E-10*XN1**2+0 9656E-2
H(5,1) =  0 8714E-3*XPT4+0 1786E+2/XPT4-0 3067
H(6,1) =  0 9184/TH1-0 3491E+4/XPT4**2+0 1518
H(7,1) =  0 3119E-2/XPT6-0 2978E-1/XPT6**2-0 7266E-4
H(1,2) =  0
H(2,2) =  1
H(3,2) =  0 2915E-1/TH1+0 4644E-3*XPT6-0 1233E-1
H(4,2) = -0 9080E-7*XN1-0 6664E-1/XPT4+0. 1152E-2
H(5,2) = -0. 1327E-3*XTT45-0 1907E+4/XN1+0 4014
H(6,2) =  0 3287E-1
H(7,2) =  0 2899E-3/DL1+0 6102/XPT4**2+0 5523E-4
H(1,3) =  0
H(2,3) =  0
H(3,3) = -0 7570E-7*XPT6**3-0 4867E-3
H(4,3) = -0. 3204E-6*XN2+0 2399E-2
H(5,3) =  0 3111E-1*TH1+0 5486E-4*XTT45-0. 3612
H(6,3) =  0. 1445E-1/DL1-0 1271E-3*XN1+0 3156
H(7,3) = -0 1322E-5
H(1,4) =  0
H(2,4) =  0
H(3,4) = -0 1980E-3*XPT6+0 3175E-2
H(4,4) = -0 4300E-5*XPT4-0 5102E-4
H(5,4) =  0 8486E-2
H(6,4) =  0 1140E-1/DL1-0 1300E-3*XN1+0. 5192
H(7,4) = -0 1324E-5
```

TABLE 3-3d
FULL ENVELOPE MODEL OF D MATRIX

```
D(1,1) = 0
D(2,1) = 0
D(3,1) = -0 4135E-14*XN1**3+0 1983E-5*XPT6**2+0 9972E-2
D(4,1) = -0 9442E-7*XN1-0 2207E+5/XN1**2+0 2096E-2
D(5,1) = -0 3541E-1*TH1+0 3135E+2/XPT4+0 4914E-1
D(6,1) = -0 6850E+4/XN1+0 1326E+9/XN2**2+0 3505
D(7,1) = -0 8329E-2/XPT4+0. 1035E-4
D(1,2) = 0
D(2,2) = 0
D(3,2) = -0. 7192E-3*XPT6**3+1. 255
D(4,2) = -0 4047*XPT6+2. 908
D(5,2) =  0 2658E-2*XPT6**3-7 119
D(6,2) = -0 2704E+4/TH1+0 8536E+7/XN1+131 6
D(7,2) = -0 3962E-6*XPT6**3+0 2829E-3
D(1,3) = 0
D(2,3) = 0
D(3,3) =  0 5358E-2*XPT4-0 1670E-5*XPT4*XPT6**2-0 4101
D(4,3) =  0 8815E-3*XPT4-0 2836E-8*XPT4**3-0 6458E-1
D(5,3) =  0. 1110E-6*XPT4**3-0. 1789E-5*XN1*XPT4+0 5499
D(6,3) =  0 1347E+1*XPT6-12 67
D(7,3) =  0 2049E-3
D(1,4) = 0.
D(2,4) = 0
D(3,4) =  0 7838*TH1-0 4666
D(4,4) = -0 3630E-2
D(5,4) = -0 2147E+1*TH1+0 2716E-7*XN1**2-1 36
D(6,4) = 1 073
D(7,4) =  0 5327E-2*TH1-0 8454E-2
D(1,5) = 0
D(2,5) = 0.
D(3,5) = -0. 3165E+3/DL1-0. 1685E+1*XPT4+425. 9
D(4,5) = -0 1446E+2*(RTH1/DL1)-0 9368E-1*XPT4+24 09
D(5,5) =  0 1183E+4/DL1-631 2
D(6,5) = -0 7482E+4/DL1+1454 0
D(7,5) =  0 9856/DL1+0. 3580E-1
```

The 1σ and 2σ bands were computed as follows. Let σ_y, and $\sigma_{y/x}$ be the standard deviations of the data and the regression errors (regression of y on x) respectively. These are defined as:

$$\sigma_y^2 = \frac{\Sigma_i (y_i - \bar{y})^2}{n-1} \tag{15}$$

$$\sigma_{y/x}^2 = \frac{\Sigma_i (y_i - \hat{y}_i)^2}{n-2} \tag{16}$$

where y_i is the data being fitted, $\bar{y}$ is the mean of all the data records and $\hat{y}_i$ is the data obtained from the regression model.

The sample correlation coefficient R is a measure of the goodness of the fit and is defined as

$$R^2 = 1 - \frac{\Sigma_i (y_i - \hat{y})^2}{\Sigma_i (y_i - \bar{y})^2}; \quad 0 \leq R \leq 1 \tag{17}$$

For a perfect model, R = 1. Conversely, $R^2 = 0$ represents a poor fit.

The three quantities, R, σ_y, and $\sigma_{y/x}$, are related by the equation

$$\sigma_{y/x}^2 = \frac{n-1}{n-2} \sigma_y^2 (1 - R^2) \tag{18}$$

For the linear engine model case n = 109, and σ_y and R are obtained from the regression program used to generate regression models. The above equation can then be written as

$$\sigma_{y/x} = 1.0094\sqrt{(1-R^2)}\,\sigma_y \tag{19}$$

The 1σ and 2σ bands on Figures 3-13a through 3-13f were computed using the above equations.

Tables 3-4a through 3-4d tabulate the quantities R^2, R, σ_y and $\sigma_{y/x}$ as part of the error analysis.

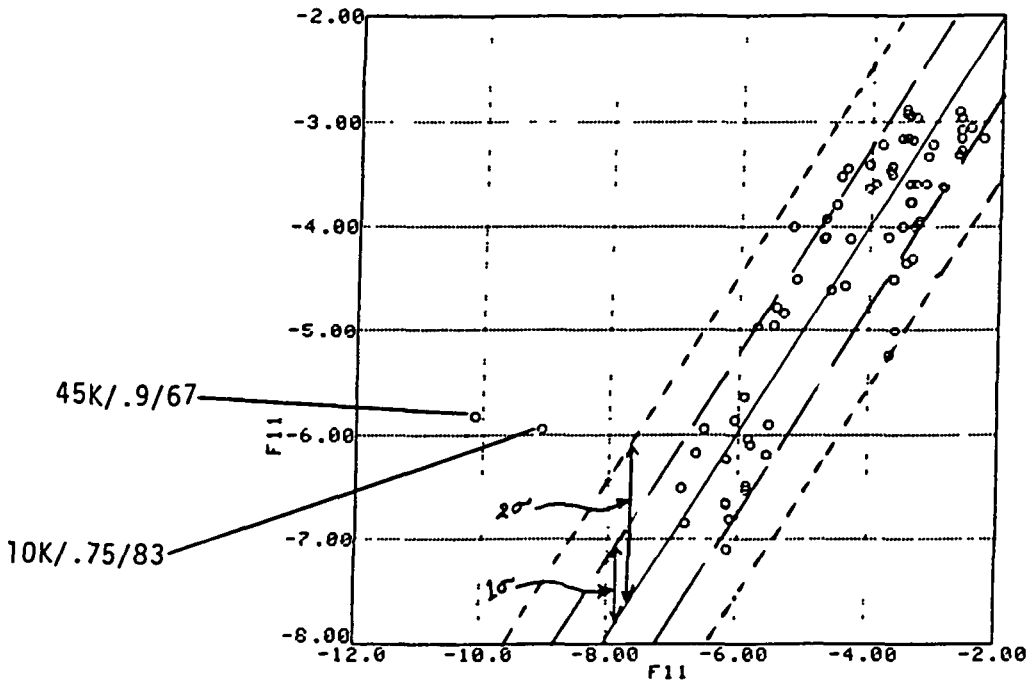

Figure 3-13a Error Analysis Plots of F_{11} Element

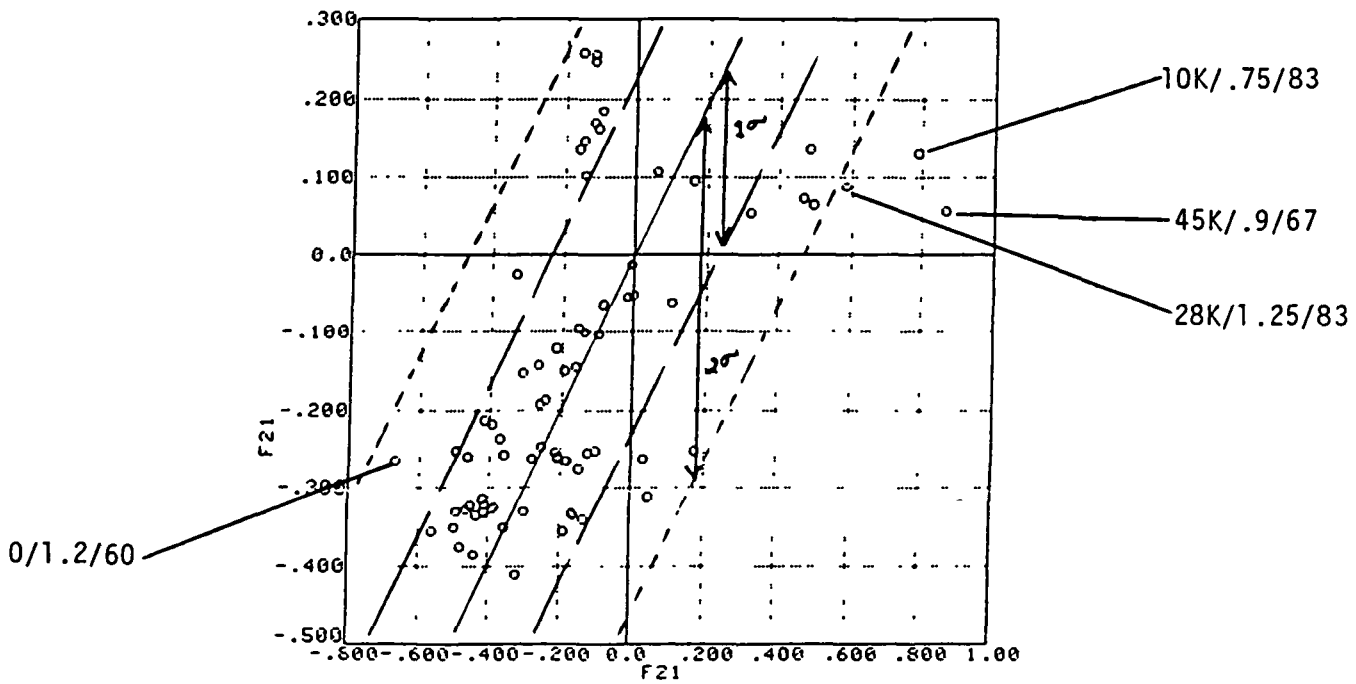

Figure 3-13b Error Analysis Plot of F_{21} Elements

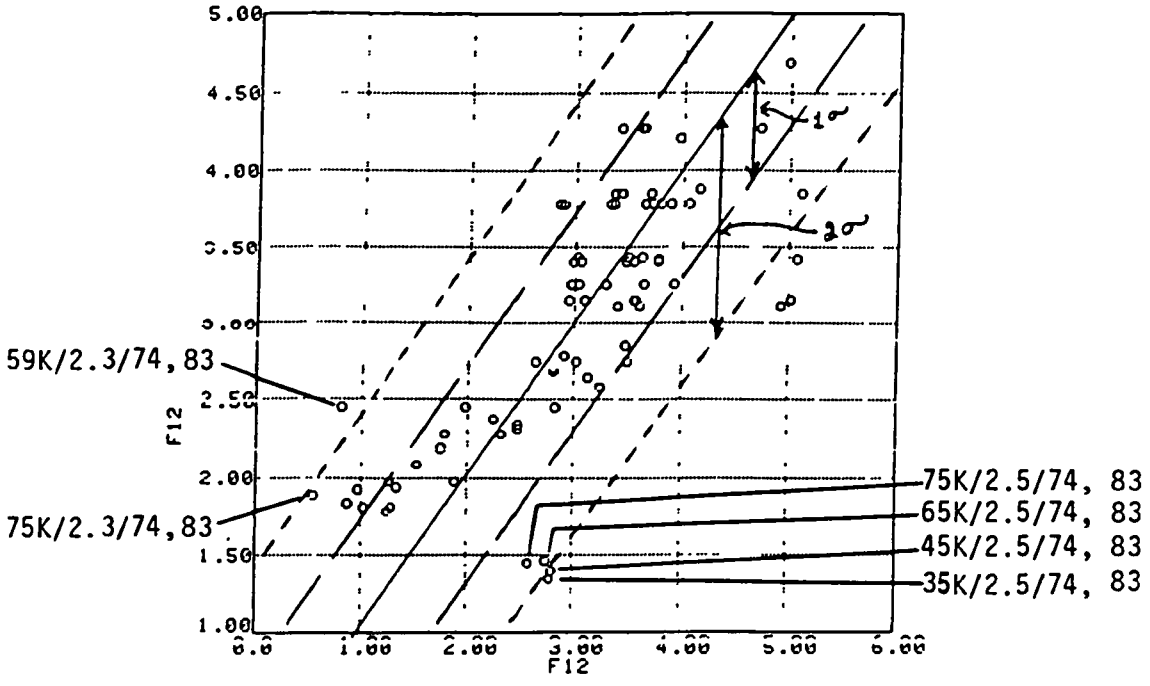

Figure 3-13c Error Analysis Plot of F_{12} Element

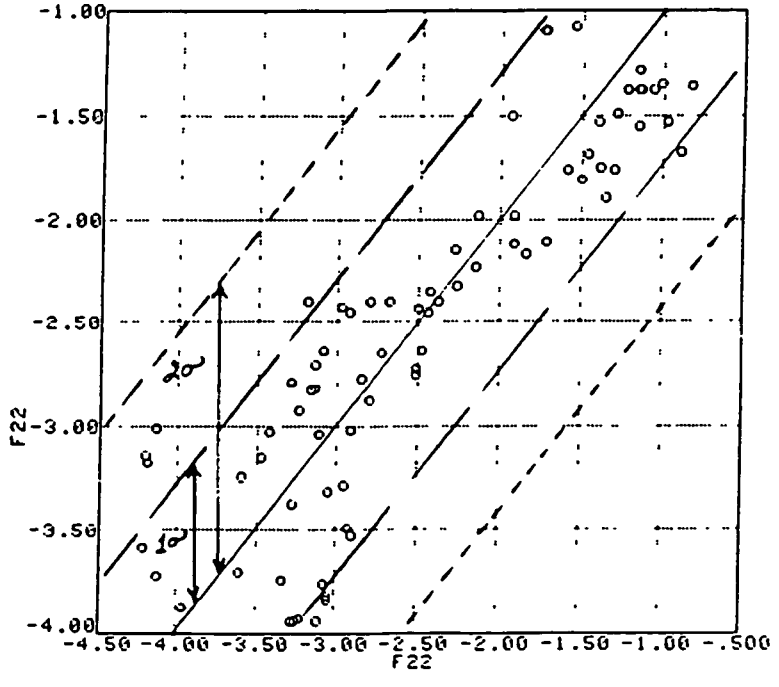

Figure 3-13d Error Analysis Plot of F_{22} Element

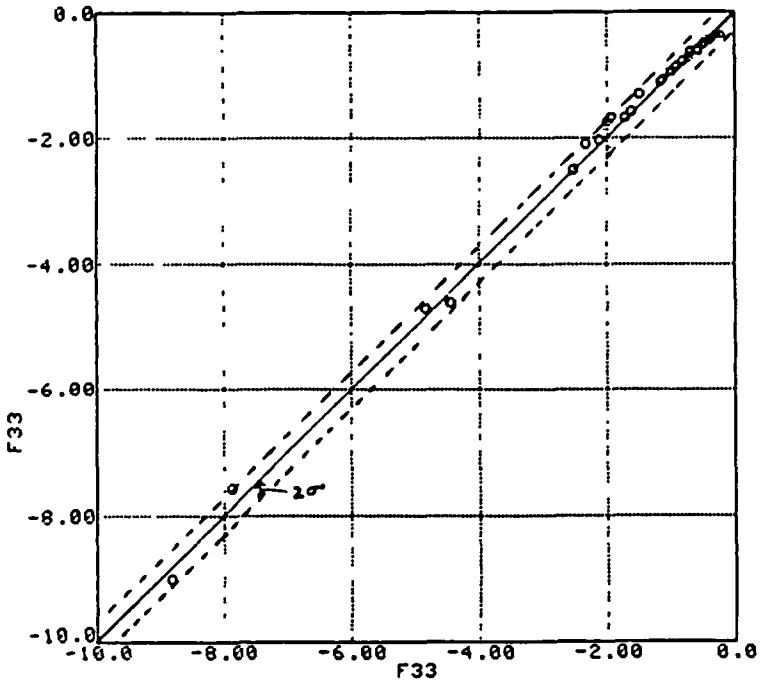

Figure 3-13e Error Analysis Plot of F_{33} Element

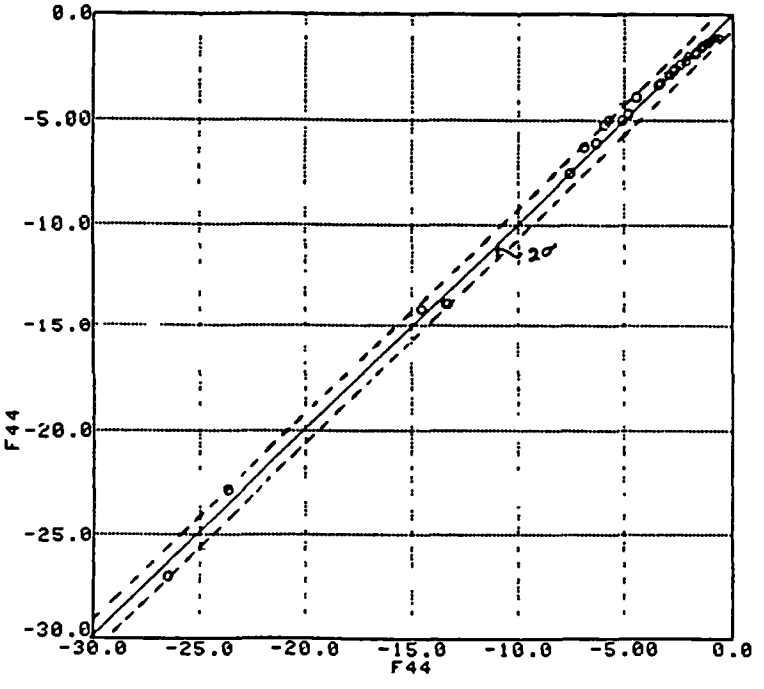

Figure 3-13f Error Analysis Plot of F_{44} Element

TABLE 3-4a

ERROR ANALYSIS OF F MATRIX ELEMENTS

Matrix Element	R^2	R	Mean	σ_y	$\sigma_{y/x}$	$\frac{\sigma y/x}{\sigma y}$
F11	0.745	0.863	-0.350	1.515	0.769	0.507
F21	0.402	0.634	-0.1681	0.3022	0.235	0.777
F31	0.440	0.663	0.1749E-2	0.1878E-1	0.1412E-1	0.752
F41	0.491	0.701	0.7128E-2	0.4945E-1	0.3545E-1	0.717
F12	0.637	0.798	2.909	1.162	0.703	0.605
F22	0.788	0.888	-0.2408	0.9844	0.455	0.463
F32	0.961	0.9803	-0.144E-1	0.2751E-1	0.006	0.198
F42	0.966	0.983	-0.4348E-1	0.7828E-1	0.015	0.185
F13	0.000	0.000	-1.597	0.4334	0.4375	1.000
F23	0.952	0.976	9.220	1.861	0.410	0.220
F33	0.997	0.9985	-1.788	2.203	0.121	0.055
F43	0.000	0.000	-0.1156	0.1339	0.1352	1.000
F14	0.948	0.974	7.309	1.660	0.380	0.229
F24	0.000	0.000	0.6013E-1	0.9085E-1	0.9127E-1	1.000
F34	0.000	0.000	0.2632E-2	0.5578E-2	0.5604E-1	1.000
F44	0.997	0.9985	-5.366	6.611	0.364	0.055

TABLE 3-4b

ERROR ANALYSIS OF $F^{-1}G$ MATRIX ELEMENTS

Matrix Element	R^2	R	Mean	σ_y	$\sigma_{y/x}$	$\frac{\sigma_{y/x}}{\sigma_y}$
$F^{-1}G11$	0.824	0.908	-0.6348	0.4701	0.198	0.422
$F^{-1}G21$	0.838	0.915	-0.5248	0.3345	0.135	0.404
$F^{-1}G31$	0.8404	0.917	-0.1661E-1	0.5268E-2	0.2114E-2	0.401
$F^{-1}G41$	0.596	0.772	-0.1272E-1	0.4172E-2	0.2664E-2	0.639
$F^{-1}G12$	0.741	0.861	-1022.0	284.4	145.4	0.511
$F^{-1}G22$	0.923	0.961	-113.6	262.1	73.07	0.279
$F^{-1}G32$	0.967	0.983	-5.828	12.06	2.201	0.183
$F^{-1}G42$	0.967	0.983	-4.708	9.788	1.786	0.183
$F^{-1}G13$	0.675	0.822	24.49	6.801	3.895	0.573
$F^{-1}G23$	0.438	0.662	1.321	4.008	3.019	0.753
$F^{-1}G33$	0.634	0.796	0.1243	0.1583	0.096	0.608
$F^{-1}G43$	0.649	0.806	0.1081	0.1280	0.076	0.595
$F^{-1}G14$	0.824	0.908	-7.034	6.369	2.685	0.422
$F^{-1}G24$	0.470	0.686	15.50	17.33	12.68	0.731
$F^{-1}G34$	0.748	0.865	0.2018	0.1788	0.090	0.504
$F^{-1}G44$	0.794	0.891	0.1468	0.1347	0.061	0.456
$F^{-1}G15$	0.971	0.985	0.1472E+5	0.2068E-5	0.3538E+4	0.171
$F^{-1}G25$	0.956	0.978	0.105E+5	0.1460E+5	0.3076E+4	0.211
$F^{-1}G35$	0.992	0.996	-378.3	624.2	56.09	0.0898
$F^{-1}G45$	0.992	0.996	-326.6	531.9	47.79	0.0898

TABLE 3-4c

ERROR ANALYSIS OF H MATRIX ELEMENTS

Matrix Element	R^2	R	Mean	σ_y	$\sigma_{y/x}$	$\frac{\sigma_{y/x}}{\sigma_y}$
H11	1.	1.	1.	0.	0.	--
H21	1.	1.	0.	0.	0.	--
H31	0.742	0.861	0.1184E-1	0.8429E-2	0.4302E-2	0.510
H41	0.393	0.627	0.279E-2	0.6902E-3	0.5403E-3	0.783
H51	0.833	0.913	-0.1687E-1	0.4572E-1	0.1877E-1	0.410
H61	0.537	0.733	0.8526	0.3497	0.2391	0.684
H71	0.406	0.637	-0.1132E-5	0.1468E-4	0.	0.774
H12	1.	1.	0.	0.	0.	--
H22	1.	1.	1.	0.	0.	--
H32	0.788	0.888	0.2647E-1	0.1112E-1	0.5144E-2	0.463
H42	0.434	0.659	-0.5460E-1	0.3873E-1	0.1906E-1	0.492
H62	0.	0.	0.3287E-1	0.5839E-1	0.5866E-1	1.005
H72	0.394	0.628	0.8334E-4	0.3207E-4	0.2508E-4	0.782
H13	1.	1.	0.	0.	0.	--
H23	1.	1.	0.	0.	0.	--
H33	0.671	0.819	-0.2707E-2	0.2531E-2	0.1459E-2	0.576
H43	0.790	0.889	-0.1297E-2	0.3850E-3	0.1773E-3	0.460
H53	0.721	0.849	-0.2283	0.1876E-1	0.9956E-2	0.531
H63	0.906	0.952	-0.7582	0.1551	0.4778E-1	0.308
H73	0.	0.	-0.1322E-5	0.2469E-5	0.2481E-5	1.005
H14	1.	1.	0.	0.	0.	--
H24	1.	1.	0.	0.	0.	--
H34	0.527	0.726	-02315E-2	0.2632E-2	0.1819E-2	0.691
H44	0.616	0.785	-0.1018E-2	0.4717E-3	0.2937E-3	0.623
H54	0.	0.	0.8486E-2	0.1296E-1	0.1303E-1	1.005
H64	0.928	0.963	-0.5890	0.1595	0.4300	0.269
H74	0.	0.	-0.1324E-5	0.2900E-5	0.2914E-5	1.005

TABLE 3-4d

ERROR ANALYSIS OF D MATRIX ELEMENTS

Matrix Element	R^2	R	Mean	σ_y	$\sigma_{y/x}$	$\frac{\sigma y/x}{\sigma_y}$
D11	1.	1.	0.	0.	0.	--
D21	1.	1.	0.	0.	0.	--
D31	0.515	0.718	0.8729E-2	0.6035E-3	0.422E-3	0.699
D41	0.635	0.797	0.9528E-3	0.9359E-4	0.5681E-4	0.607
D51	0.993	0.997	0.1718	0.6941E-1	0.5834E-2	0.084
D61	0.822	0.907	0.5703	0.9800E-1	0.4154E-1	0.424
D71	0.992	0.996	-0.3345E-4	0.1978E-4	0.1777E-5	0.089
D12	1.	1.	0.	0.	0.	--
D22	1.	1.	0.	0.	0.	--
D32	0.960	0.980	-19.84	20.11	4.041	0.201
D42	0.966	0.983	-8.314	3.973	0.736	0.185
D52	0.9696	0.985	70.84	73.95	12.95	0.175
D62	0.762	0.873	-1270	740.6	362.99	0.49
D72	0.835	0.914	-0.1134E-1	0.1188E-1	0.4848E-2	0.408
D13	1.	1.	0.	0.	0.	--
D23	1.	1.	0.	0.	0.	--
D33	0.785	0.886	0.3909	0.1623	0.7561E-1	0.466
D43	0.907	0.952	0.8678E-1	0.3607E-1	0.1105E-1	0.306
D53	0.751	0.867	-1.327	0.5617	0.2816	0.501
D63	0.747	0.864	24.69	15.04	7.601	0.505
D73	0.	0.	0.2049E-3	0.1285E-3	0.1291E-3	1.005
D14	1.	1.	0.	0.	0.	--
D24	1.	1.	0.	0.	0.	--
D34	0.583	0.764	0.4670	0.2928	0.1899	0.649
D44	0.	0.	-0.3630E-2	0.4006E-2	0.4026E-2	1.005
D54	0.791	0.889	-1.788	1.183	0.5433	0.459
D64	0.	0.	1.073	21.74	21.85	1.005

TABLE 3-4d (Cont'd)

Matrix Element	R^2	R	Mean	σ_y	$\sigma_{y/x}$	$\frac{\sigma_{y/x}}{\sigma_y}$
D74	0.522	0.722	-0.2108E-2	0.2104E-2	0.1462E-2	0.695
D15	1.	1.	0.	0.	0.	-
D25	1.	1.	0.	0.	0.	-
D35	0.990	0.995	-811.1	1212.	121.16	0.099
D45	0.983	0.9915	-35.86	52.92	6.932	0.131
D55	0.985	0.9925	2577.	4226.	520.0	0.123
D65	0.982	0.9910	-0.1883E+5	0.2676E+5	0.3607E+4	0.135
D75	0.995	0.9975	2.708	3.503	0.2489	0.071

3.7 VALIDATION OF THE SIMPLIFIED NONLINEAR MODEL

The full envelope simplified nonlinear model was validated by comparing its open loop transient response with the detailed F100/MVCS (Multivariable Control System) simulation as shown in Figure 3-14. The simplified model was driven by the control variables from the detailed F100/MVCS simulation. Base point information needed in the simplified model was derived by using fan speed from the model itself. The fan speed is used to compute a virtual power code which in turn (along with TT2 and Mach No.) is used to look up reference points (base points), as shown in Figure 3-15.

Figures 3-16 through 3-20 present transient plots of low rotor speed (N1), high rotor speed (N2), burner pressure (PT4), augmentor pressure (PT6), and Fan turbine inlet temperature (FTIT or TT45) at the flight points indicated on the figures. In general, the transient response of the simplified nonlinear model matched the detailed nonlinear F100/MVCS simulation quite well. The oscillations in Figures 3-18 and 3-19 originate within the detailed F100/MVC simulation. At some flight conditions, the steady state match was in error due to inaccuracies in the base point schedules which were taken directly from the MVCS logic.

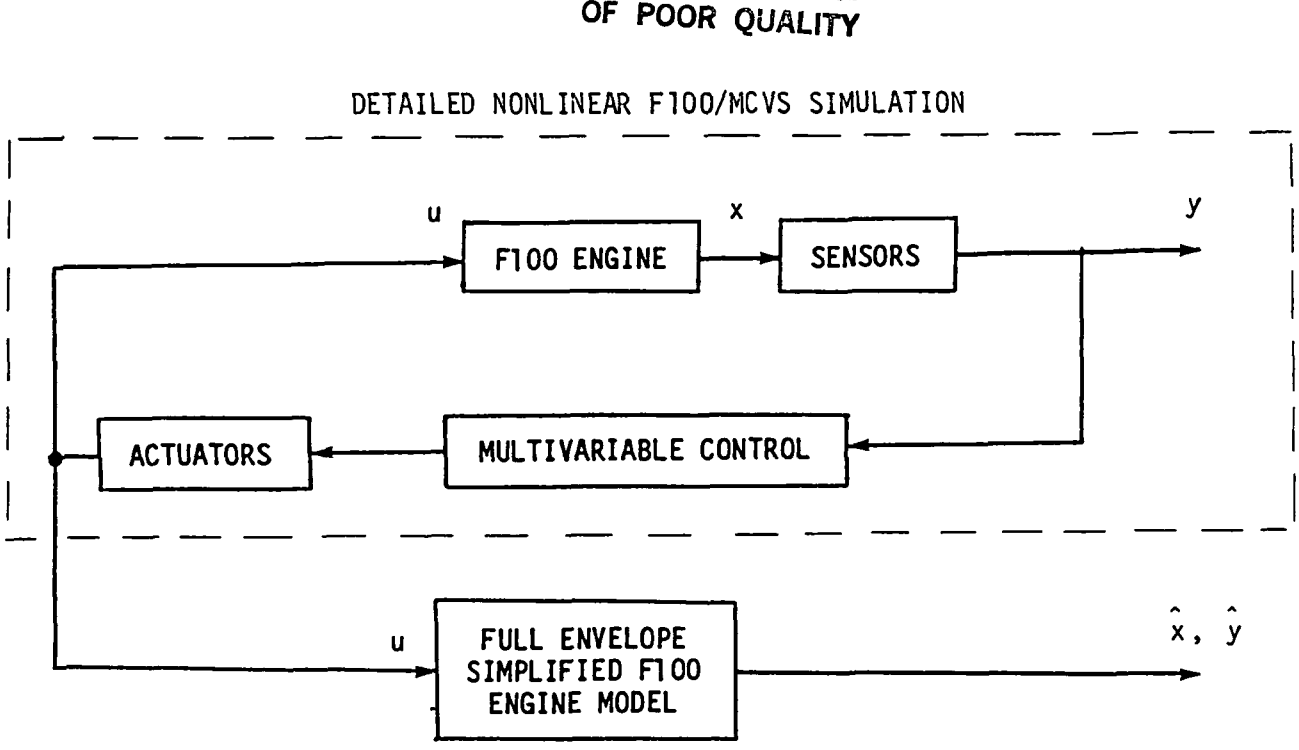

Figure 3-14 Comparison of Simplified Full Envelope Model with Detailed F100/MCVS Simulation

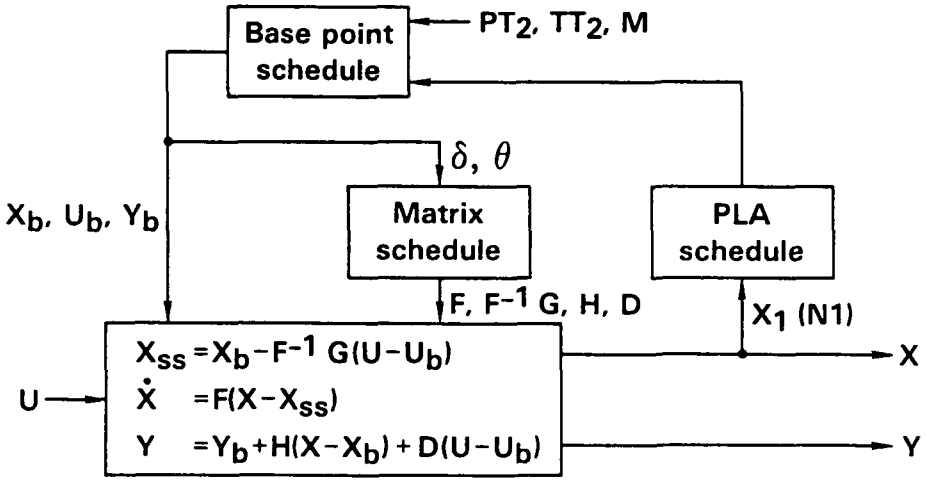

States: $X=[N1, N2, TT4LO, TT45LO]^T$

Inputs: $U=[WF, AJ, CIVV, RCVV, BLC]^T$

Outputs: $Y=[N1, N2, PT4, PT6, FTIT, FNMX, SMHC]^T$

Figure 3-15 Stand Alone Simplified Simulation

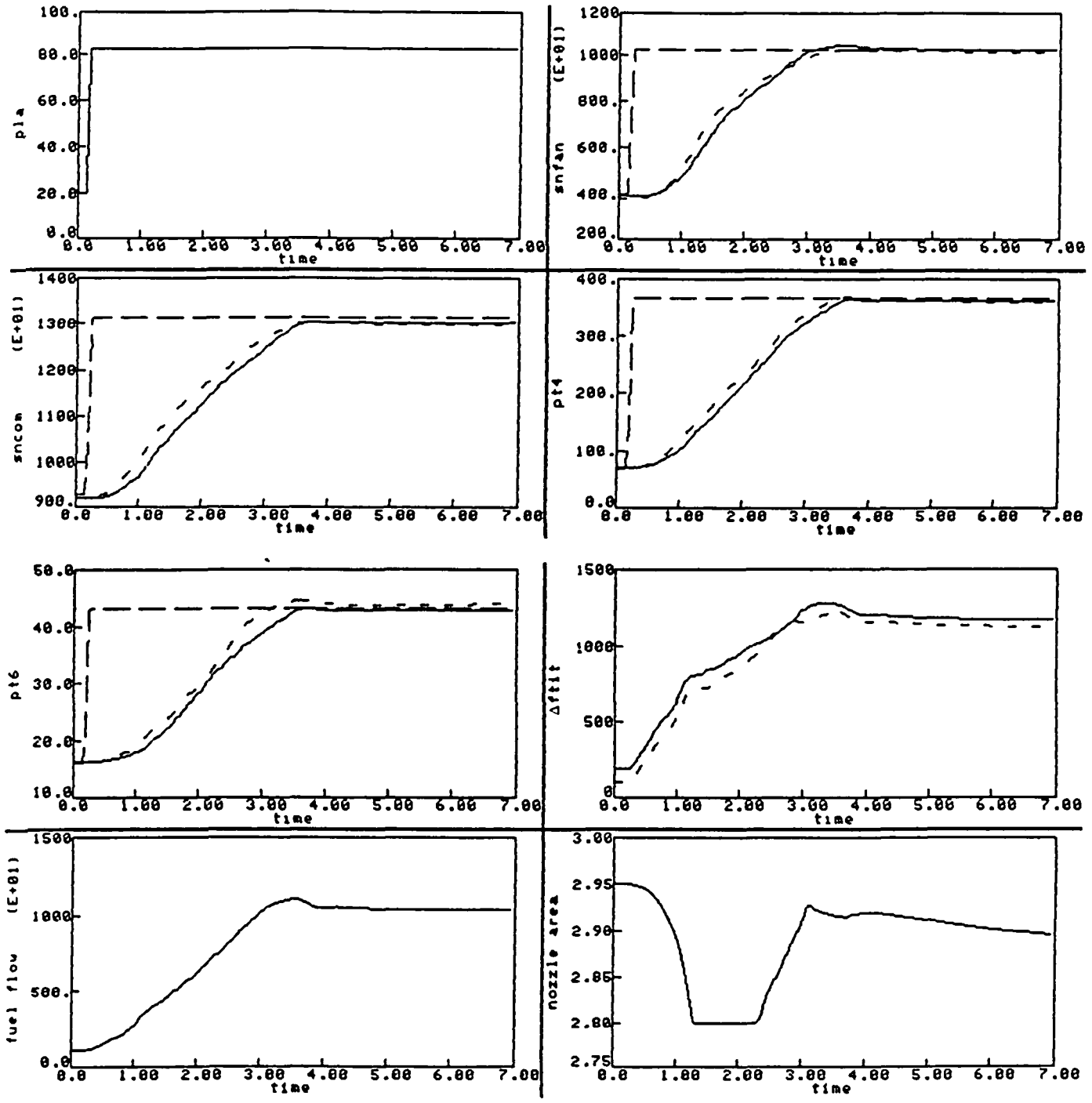

Figure 3-16 Comparison of the Transient Performance of the Nonlinear Engine (———) and the Simplified Model (-----) at Altitude = 0 feet, Mach No. = 0 and PLA Step From 20 Degrees to 83 Degrees

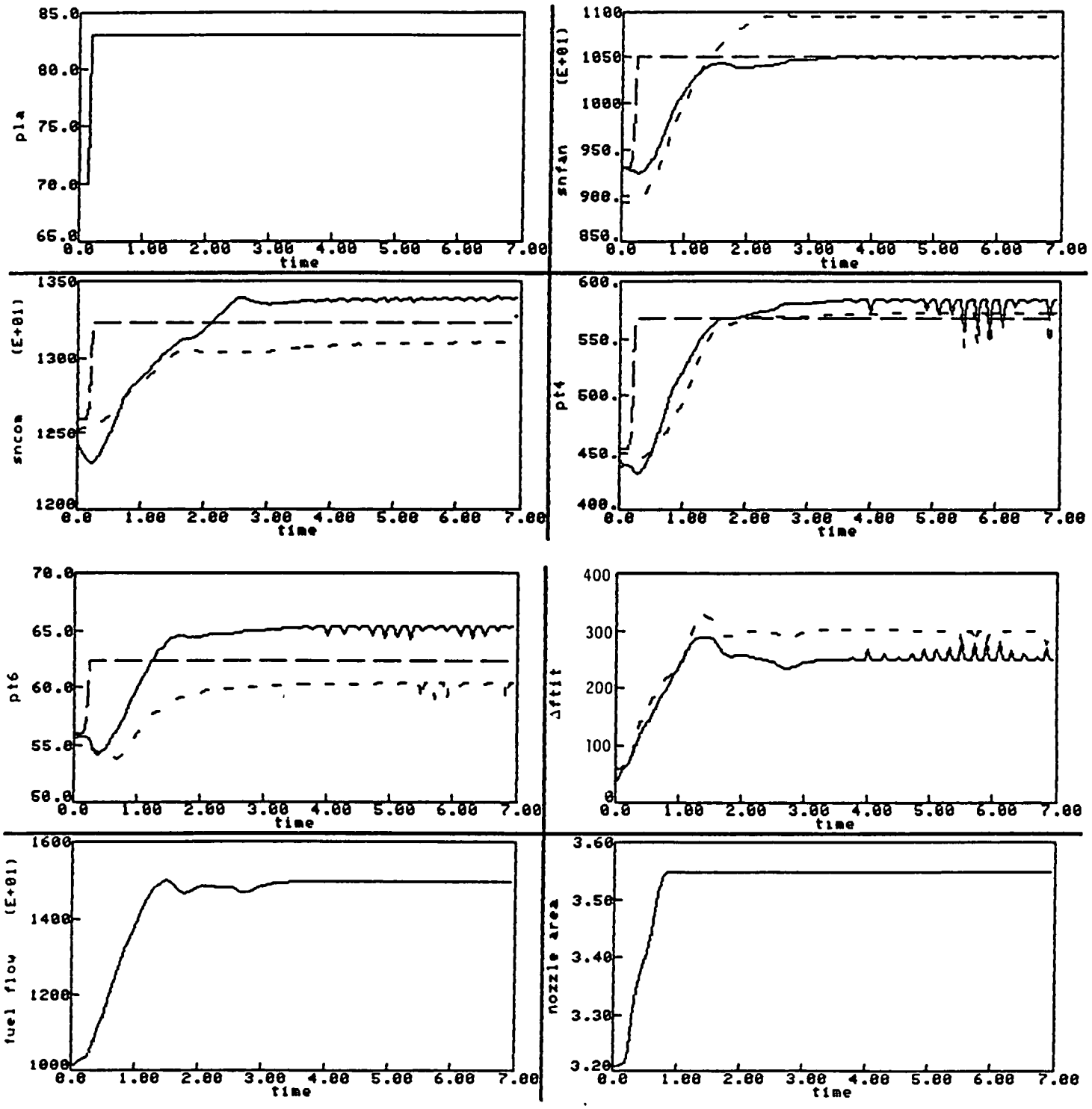

Figure 3-17 Comparison of the Transient Performance of the Nonlinear Engine (———) and the Simplified Model (-----) at Altitude = 0 feet, Mach No. = 1.2 and PLA Step From 70 Degrees to 83 Degrees

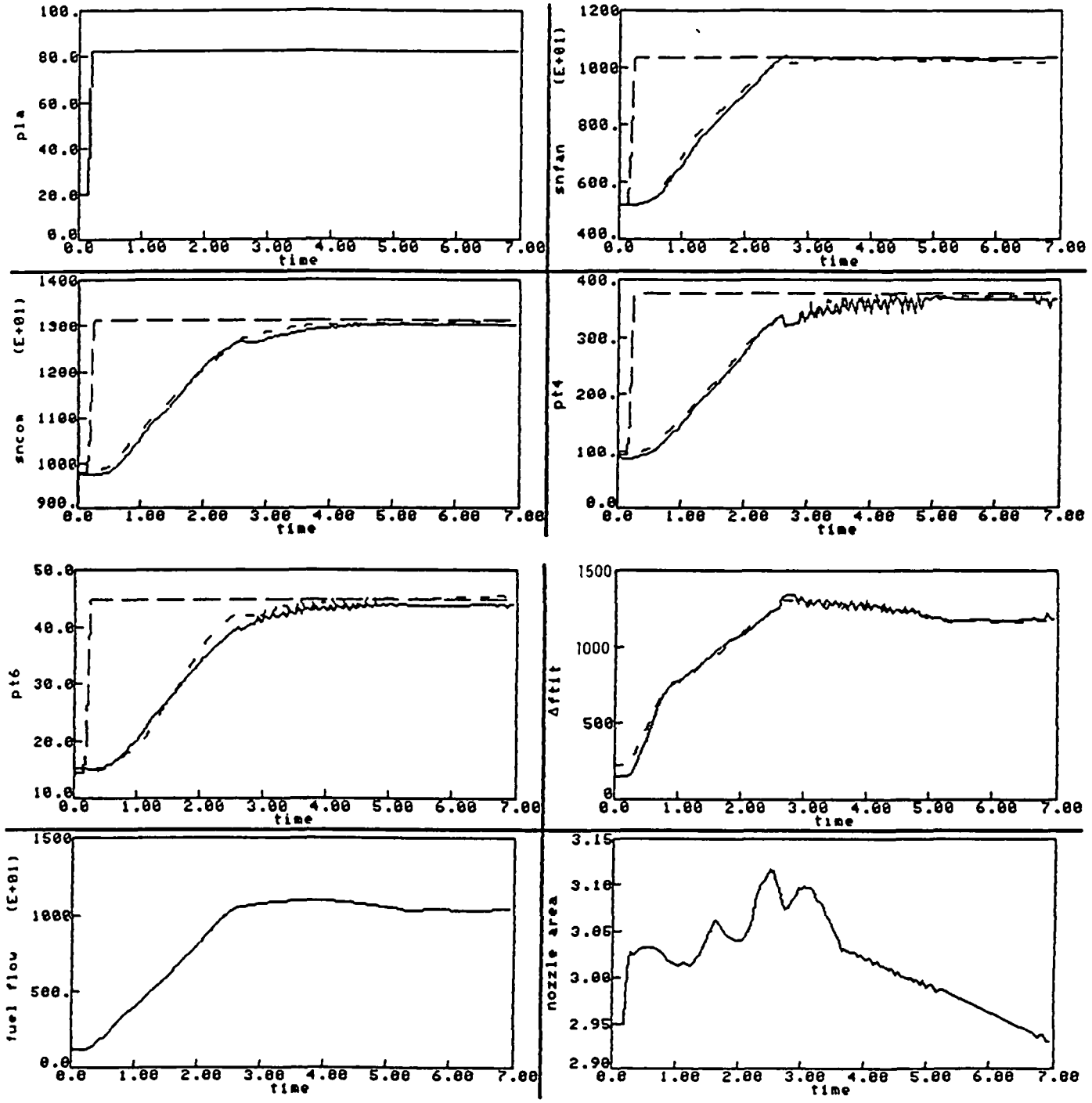

Figure 3-18 Comparison of the Transient Performance of the Nonlinear Engine (———) and the Simplified Model (-----) at Altitude = 10,000 feet, Mach No. = 0.9 and PLA Step From 70 Degrees to 83 Degrees

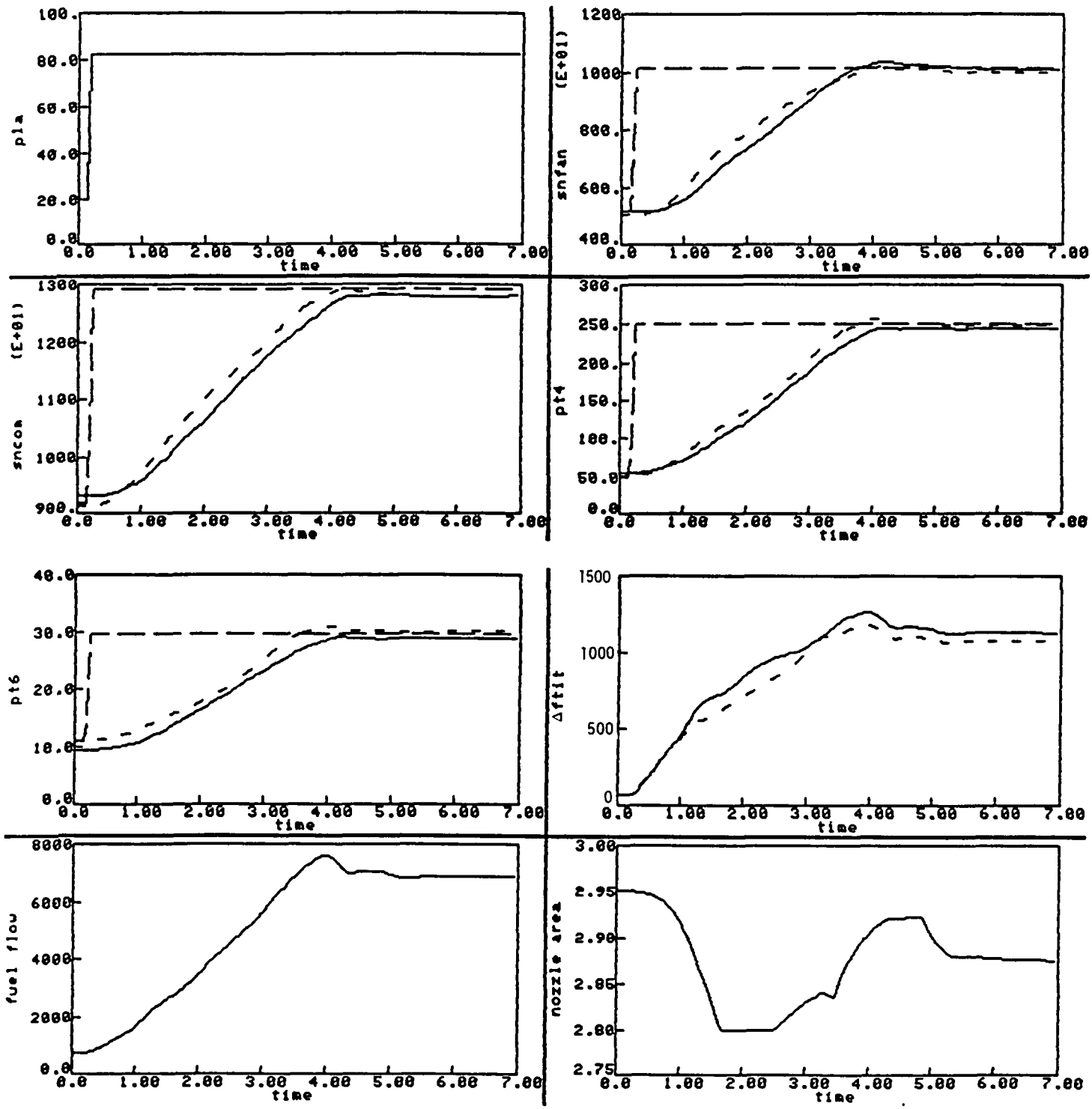

Figure 3-19 Comparison of the Transient Performance of the Nonlinear Engine (———) and the Simplified Model (-----) at Altitude = 20,000 feet, Mach No. = 0.75 and PLA Step From 20 Degrees to 83 Degrees

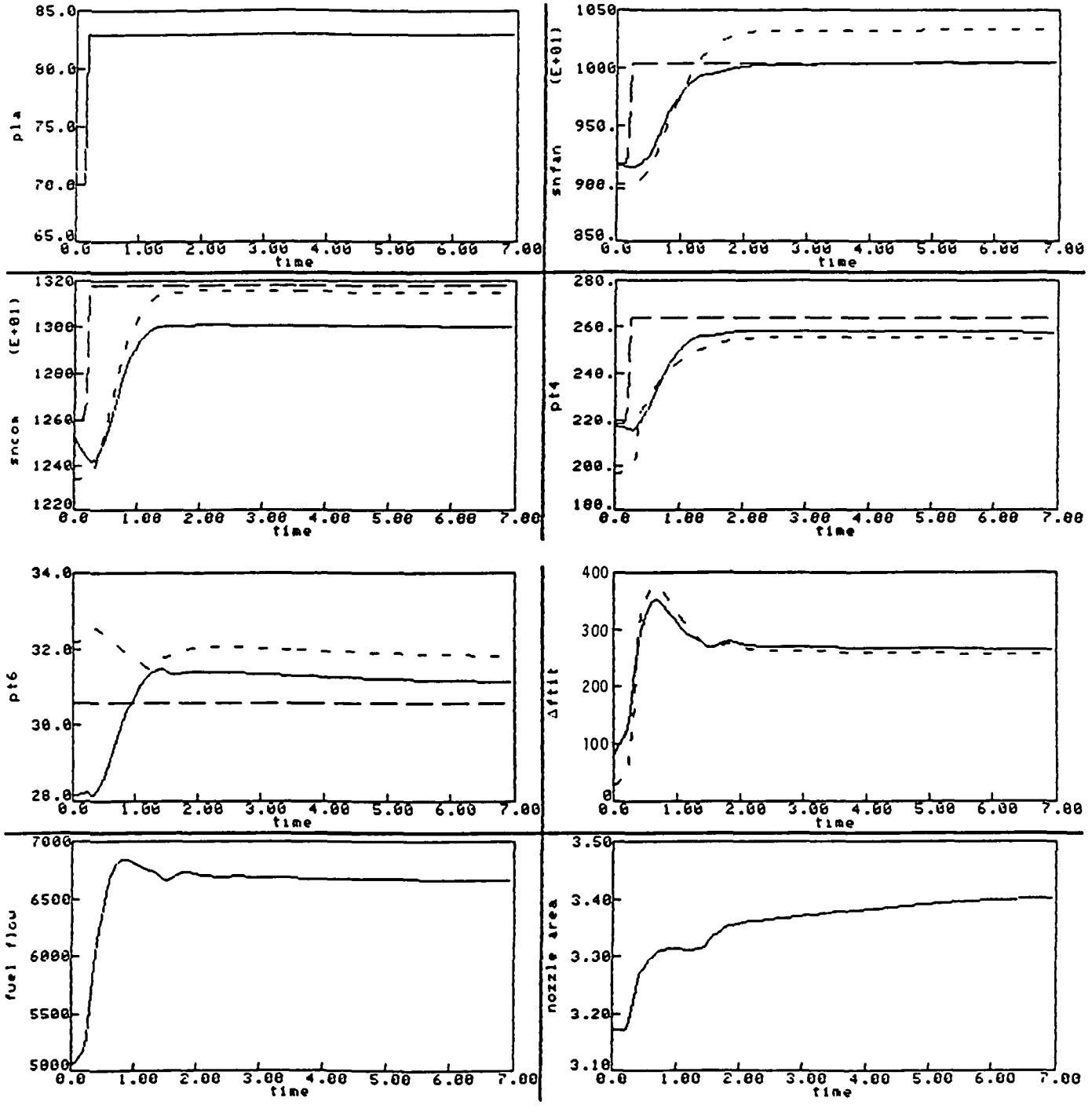

Figure 3-20 Comparison of the Transient Performance of the Nonlinear Engine (———) and the Simplified Model (-----) at Altitude = 40,000 feet, Mach No. = 2.0 and PLA Step From 70 Degrees to 83 Degrees

SECTION 4

BASELINE DIA ALGORITHM

An advanced concept for the Detection, Isolation and Accommodation (DIA) of sensor failures in gas turbine engine control systems, was developed under NASA contract NAS3-22481. This concept was selected based upon the results of a screening process of five candidate concepts for their DIA performance in a turbine engine control system. The selected concept was then evaluated in comparison to a parameter synthesis concept for DIA performance.

The five concepts were formulated based upon techniques from estimation and filtering theories and statistics. They were evaluated by application in an F100 engine and Multivariable Control System (F100/MVCS) simulation. The F100 Multivariable Control System was developed under Air Force Contract F33615-75-C-2053. In the screening process a simplified version of the simulation of the F100 engine and multivariable control system was used. This simplified simulation was also used as the model for the filters in the various advanced detection, isolation and accommodation concepts.

The advanced concept from NASA contract NAS3-22481 served as the baseline DIA algorithm in this program. The following sections describe this concept and discuss the problem areas identified in the above referenced contract.

4.1 ALGORITHM DESCRIPTION

The selected advanced DIA concept utilizes a Weighted Sum-Squared Residual technique to detect soft failures. A normal mode Kalman filter; i.e., a filter designed to use all sensor inputs with no failure assumed on those inputs, is used to generate the residuals and the estimated measurements. Detection and isolation of hard-over failures is also accomplished with the normal mode filter by testing for large values of the individual residuals. Isolation of soft failures is accomplished by likelihood ratio based testing of innovations from a bank of Kalman filters, each designed with the assumption of one failed input. Accommodation is accomplished by reconfiguring the normal mode Kalman filter to eliminate the failed sensor from the input. The baseline DIA concept is shown in Figure 4-1 and is described in detail in Appendix A.

The configuration of the multivariable control and fault detection logic used in conjunction with the F100 engine simulation is shown in Figure 4-2. The form of the control law is given by

$$U = U_b + C_p(\hat{Z}_p - Z_{pb}) + \int C_i(\hat{Z}_i - Z_{ib})\, dt \qquad (1)$$

where U is the input vector $[WF\ AH\ CIVV\_RCVV\ BL\_C]^T$, $\hat{Z}p$ is the estimate of the output vector, $[N1\ N2\ PT4\_PT6\ FTIT]^T$, and $\hat{Z}_i$ is the estimate of the vector $[N1\ PT6]^T$. The vector $\hat{Z}i$ is a subset of the vector $\hat{Z}p$. The hat ($\wedge$) denotes the estimates. U_b, Z_{pb} and Z_{ib} are the base point vectors and

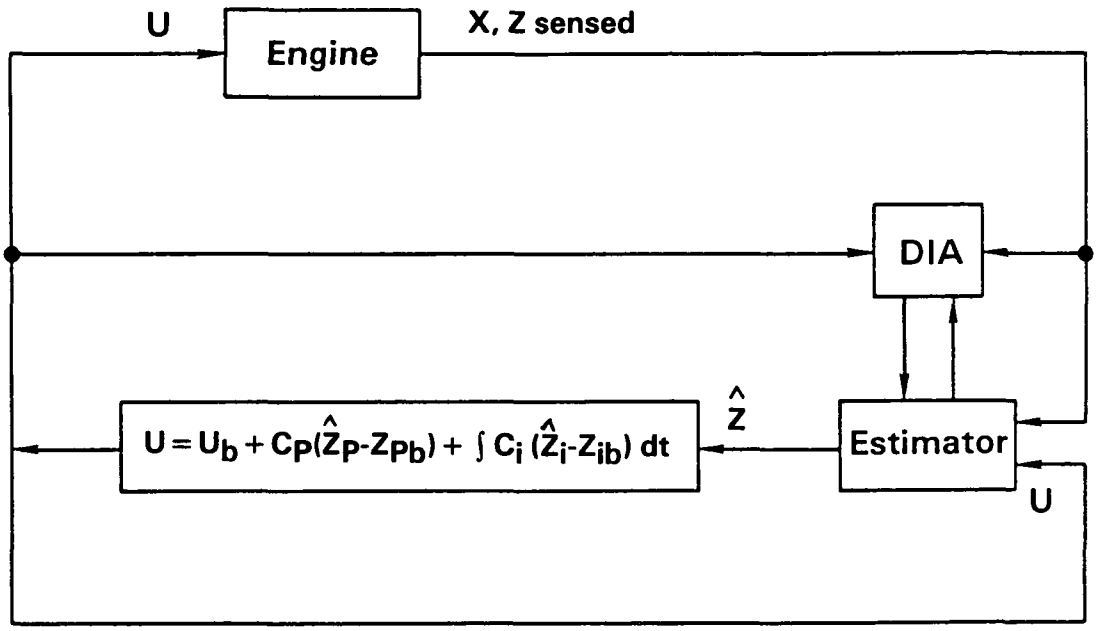

Figure 4-1 Baseline DIA Algorithm

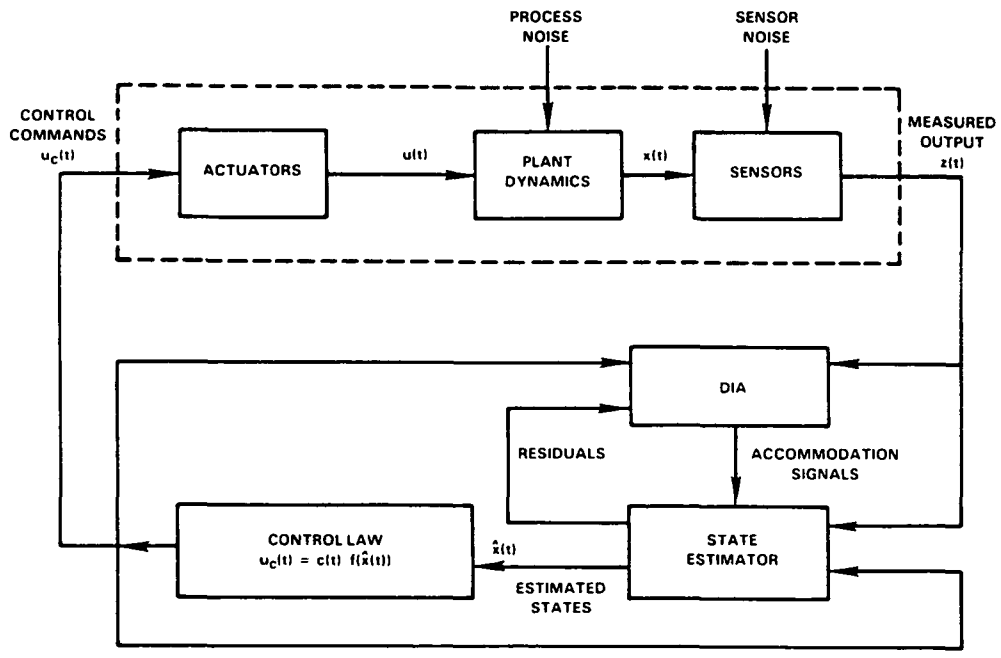

Figure 4-2 Generalized Block Diagram of Failure Detection, Isolation, and Accommodation Logic

C_p and C_i are proportional and integral control gain matrices. The proportional part of the control provides regulation and the integral part provides trim for the fan speed (N1) and augmentor pressure (PT6). Note that the control law uses the estimates for both the proportional and integral portions. The variables in the vectors above are defined as follows.

inputs (U):

WF	fuel flow (lbs/hr)
AJ	nozzle area (sq.ft.)
CIVV	compressor inlet guide vane (deg)
RCVV	rear compressor variable vane (deg)
BLC	bleed flow (%)

outputs (Z):

N1	fan speed (rpm)
N2	compressor speed (rpm)
PT4	burner pressure (psia)
PT6	augmentor pressure (psia)
FTIT	fan turbine inlet temperature (°R)

4.2 PROBLEM DEFINITION

The results of the detailed evaluation of the advanced DIA concept against the parameter systhesis concept are presented in the final report on NASA Contract NAS3-22461 [1]. The DIA performance of the advanced concept was generally good and it was demonstrated to be a viable concept for real-time applications. Several problem areas were identified in the referenced contract. These problems consisted primarily of inaccuracies in the simplified nonlinear engine model used in the estimation filters of the advanced concept, steady state biases on the outputs of the estimation filters, and steady state hangoff errors in the engine power setting parameters of fan speed (N1) and augmentor pressure (PT6).

In the following paragraphs, the problem areas identified are discussed.

4.2.1 DIA/Control Interaction

The F100/MVC control mode requires N1 and PT6 trimmed to their reference points. In the baseline DIA algorithm these outputs hang off from their reference points because the estimated values of these parameters are fed back to the control law (see Figure 4-1). DIA algorithm revision is required either to allow feedback of actual sensor values or to eliminate the bias errors from the estimates such that the estimator outputs equal sensor outputs when there is no failure. Three revisions were defined to accomplish this objective and are discussed in Section 5.1.

4.2.2 DIA Performance

The estimation errors in fan turbine inlet temperature (FTIT) were very large at many flight conditions (reference 1), causing false alarms. The filter gain on FTIT was also low and was not very effective in minimizing the residuals. An improved engine model and improved filter gain schedule were required to improve the estimate of FTIT and reduce the possibility of false alarms.

SECTION 5

DEVELOPMENT AND EVALUATION OF REVISIONS TO THE DIA ALGORITHM

The revisions to the DIA algorithms were developed to eliminate the steady state hangoff errors in the engine outputs. The DIA algorithm discussed in section 4 was used as the baseline algorithm. Three revisions were developed and were evaluated using the F100/MVCS/DIA simulation as the testbed. As a result, one revision was selected and expanded for full envelope operation. The resultant revision was implemented in the F100/MVCS/DIA simulation, for detailed evaluation.

This section presents a discussion of each of the three revisions, results of the evaluation, development of the filter gain matrix schedule and the microprocessor requirements for the revised DIA algorithm.

5.1 DESCRIPTION OF THE DIA ALGORITHM REVISIONS

The three logic revisions which were studied in this program, either reconfigure the control structure or supplement the estimator logic with integrators which drive the residual errors ($Z-\hat{Z}$) to zero. These revisions are described in the following sections.

5.1.1 DIA Algorithm Revision 1

In Revision 1, the sensor values are fed back to the control algorithm when there are no detected sensor failures. In this situation, any biases on the estimator outputs will not affect the accuracy of the closed loop control mode because the estimator is not in the control loop. When a sensor failure is detected, the appropriate estimator output will be substituted for the sensor value. Any bias on the estimator output will contribute to the degraded engine operation when running on estimated values. This logic revision is shown in Figure 5-1.

The form of the control law (equation 1 in Section 4) for this revision is as follows.

No failure:

$$U = U_b + C_p(Z_p - Z_{pb}) + \int C_i(Z_i - Z_{ib})\,dt \qquad (1)$$

Failure in Channel 1 (N1):

$$U = U_b + C_p \begin{bmatrix} \hat{N1}-N1b \\ N2-N2b \\ PT4-PT4b \\ PT6-PT6b \\ FTIT-FTITb \end{bmatrix} + C_i \int \begin{bmatrix} \hat{N1} - N1b \\ PT6 \quad PT6b \end{bmatrix} dt \qquad (2)$$

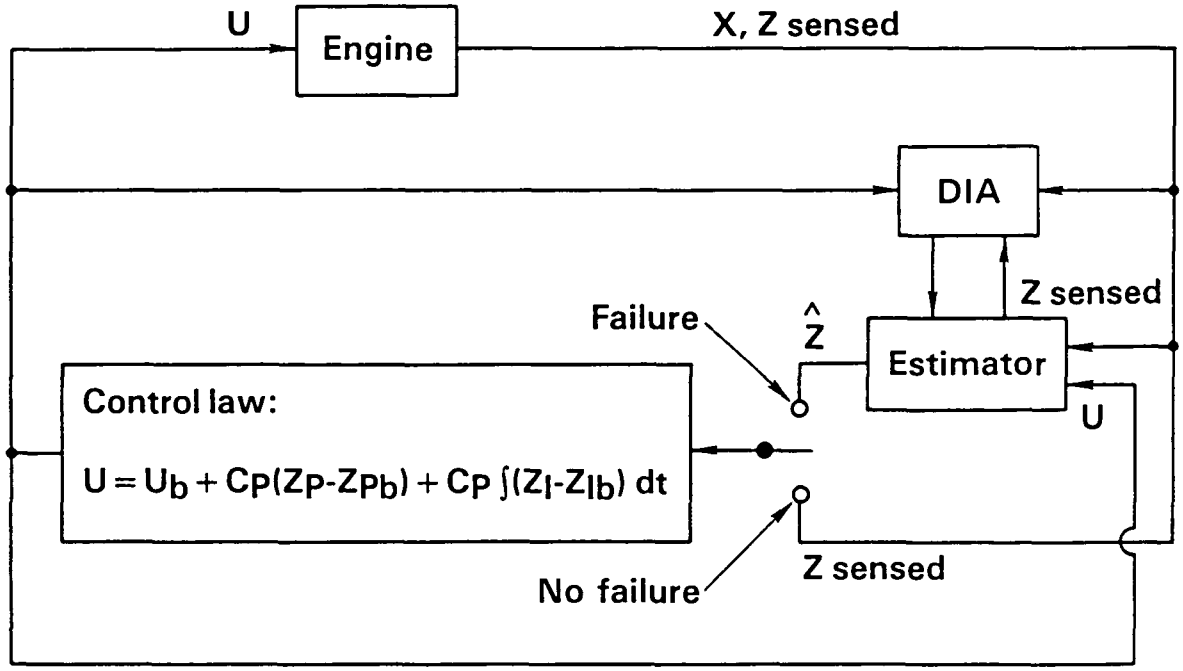

Figure 5-1 DIA Algorithm Revision 1

where Z_p is the output vector $[N1\ N2\ PT4\ PT6\ FTIT]^T$ and Z_i is the vector $[N1\ PT6]^T$. Note that in equation 2, the sensed value of N1 is replaced by its estimate ($\hat{N1}$) after failure isolation.

The responses of the engine and the estimator, with Revision 1 implemented in the F100/MVCS/DIA simulation, are shown in Figure 5-2 for a no failure case at the flight point of alt/M/PLA=0/0/36. This figure shows time histories of power lever angle (PLA), fan speed (N1 or SNFAN), compressor speed (N2 or SNCOM), burner pressure (PT4), augmentor pressure (PT6), fan turbine inlet temperature (FTIT), net thrust (FNMX) and compressor surge margin (SMHC). At time t = 0. seconds, N1 and PT6 are at their reference points. A small initialization transient is seen in all outputs. After the transient is over, N1 is trimmed to its reference point but PT6 has a small hangoff. This hangoff error goes to zero at a slow rate, due to a low value of the PT6 integrator gain in the Multivariable Control mode.

5.1.2 DIA Algorithm Revision 2

In Revision 2, the estimator outputs are fed back all of the time to the proportional or Linear Quadratic Regulator (LQR) portion of the control mode. When there are no detected sensor failures, the sensor outputs are fed back to the integral portion of the control mode. In this situation actual N1 and PT6 will be trimmed to their reference points and any biases on the estimator outputs will not affect the steady state control accuracy. Furthermore, rapid transient failures of sensors should have less impact on the system than with Revision 1 since the integrators will act as 'filters' on the actual sensor measurements. The estimator outputs, driving the proportional mode, will not respond rapidly to a failure. When a sensor failure is detected, the appropriate estimator output will be substituted for the actual sensor value in the integral control mode. This logic revision is shown in Figure 5-3.

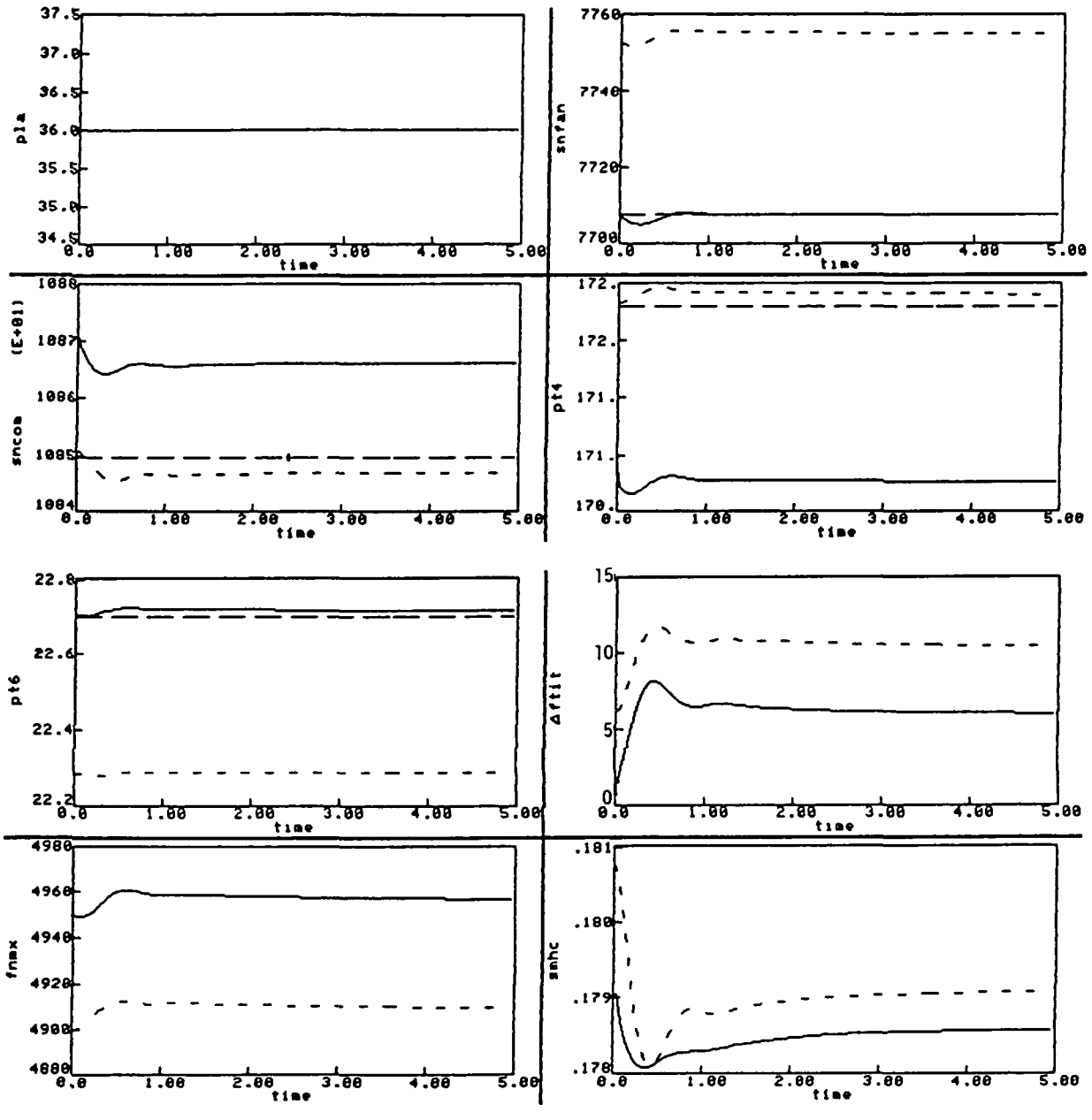

Figure 5-2 Steady State Results for Revision 1 with No Failure at the Flight Condition OK/OM, PLA=36.0 Degrees. Engine (————), Estimate (— — — —), Reference (———— ————)

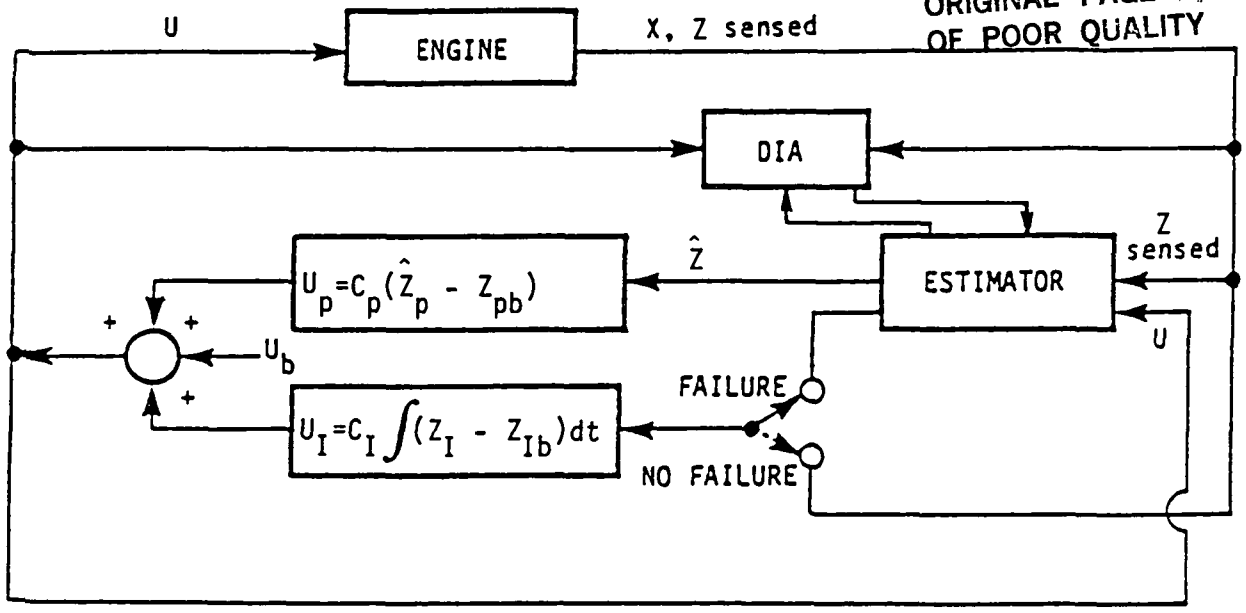

Figure 5-3 DIA Algorithm Revision 2

The control law (equation 1 in Section 4) for this revision can be written in the following form.

No Failure:

$$U = U_b + C_p(\hat{Z}_p - Z_{pb}) + \int C_i\,(Z_i - Z_{ib})\quad dt \tag{3}$$

Failure in Channel 1 (N1):

$$U = U_b + C_p(\hat{Z}_p - Z_{pb}) + C_i\int\begin{bmatrix}\hat{N1}-N1_b\\ PT6-PT6\end{bmatrix}\quad dt \tag{4}$$

Note that $\hat{N1}$ is being used in the integral portion after failure isolation.

Figure 5-4 shows the response of the engine and the estimator outputs for the no-failure case at the flight condition 0/0/36 with Revision 2 implemented in the simulation. The parameters plotted are the same as those shown in the plots for Revision 1. These plots also exhibit an initial minor transient due to simulation initialization. The small hangoff in PT6 is due to the reasons described in Section 5.1.1.

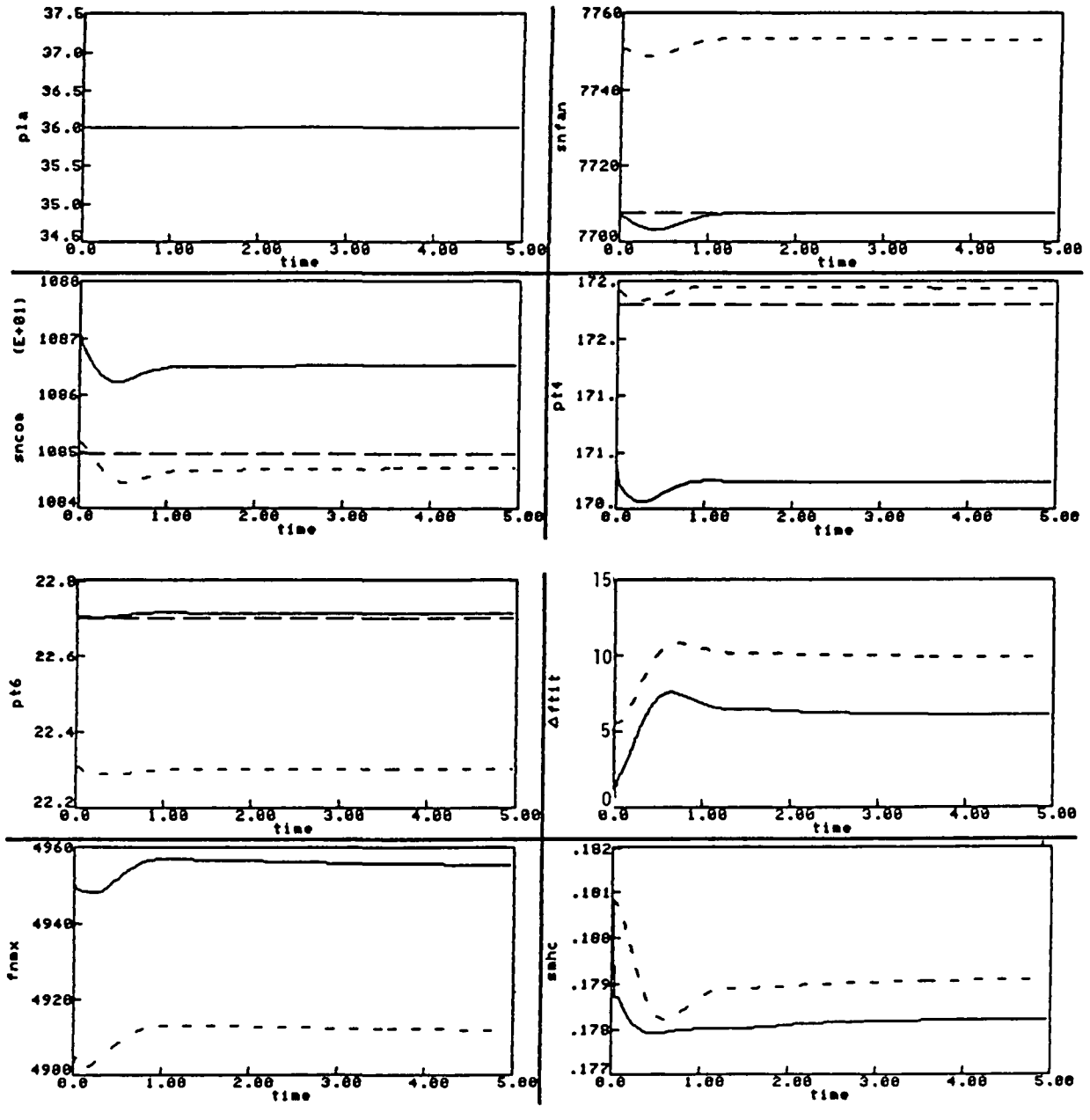

Figure 5-4 Steady State Results for Revision 2 with No Failure at the Flight Condition OK/OM, PLA = 36.0 Degrees. Engine (————), Estimate (— — — —), Reference (———— ————)

5.1.3 DIA Algorithm Revision 3

In this revision the estimator outputs are fed back all of the time to both the proportional (LQR) and integral portions of the control algorithm. Supplementary logic is implemented in the detection, isolation and accommodation algorithm to trim out the estimator output bias errors in steady state. As an example, this logic could take the form of low gain or "slow" trim integrators driven by errors between actual sensor outputs and estimator outputs. This logic revision is shown in Figure 5-5.

In this case the control law is written as

$$U = U_b + C_p\,(\hat{Z}_p - Z_{pb}) + C_i \int (\hat{Z}_i - Z_{ib})\quad dt \tag{5}$$

in both the failure and the no failure cases. Equation (5) is the same as equation (1) in Section 4.

To design the supplementary integral part for the estimator, the approach selected was to estimate the bias in the estimate and add it to the corresponding estimate. This is described by the following equations.

$$\delta\,\dot{\hat{X}} = F(\hat{X} - X_b) + G(U - U_b) + K_p(Z - \hat{Z}) \tag{6}$$

$$\delta\,\dot{\hat{b}} = K_i(Z - \hat{Z}) \tag{7}$$

$$\hat{Z} = Z_b + H(\hat{X} - X_b) + D(U - U_b) + \hat{b} \tag{8}$$

In matrix form, the above equations can be written as

$$\begin{bmatrix} \delta\dot{\hat{X}} \\ \delta\dot{\hat{b}} \end{bmatrix} = \begin{bmatrix} F & 0 \\ 0 & 0 \end{bmatrix} \begin{bmatrix} \delta\hat{X} \\ \delta\hat{b} \end{bmatrix} + \begin{bmatrix} G \\ 0 \end{bmatrix} \delta U + \begin{bmatrix} K_p \\ K_i \end{bmatrix} (Z - \hat{Z}) \tag{9}$$

$$\delta\,\hat{Z} = \begin{bmatrix} H & I \end{bmatrix} \begin{bmatrix} \delta\hat{X} \\ \delta\hat{b} \end{bmatrix} + D\,\delta U \tag{10}$$

The error equations can be written as follows.

$$\begin{bmatrix} \delta\dot{\tilde{X}} \\ \delta\dot{\tilde{b}} \end{bmatrix} = \begin{bmatrix} F & 0 \\ 0 & 0 \end{bmatrix} \begin{bmatrix} \delta\tilde{X} \\ \delta\tilde{b} \end{bmatrix} + \begin{bmatrix} K_p \\ K_i \end{bmatrix} (Z - \hat{Z}) \tag{11}$$

$$\delta\tilde{Z} = \begin{bmatrix} H & I \end{bmatrix} \begin{bmatrix} \delta\hat{X} \\ \delta\tilde{b} \end{bmatrix} \tag{12}$$

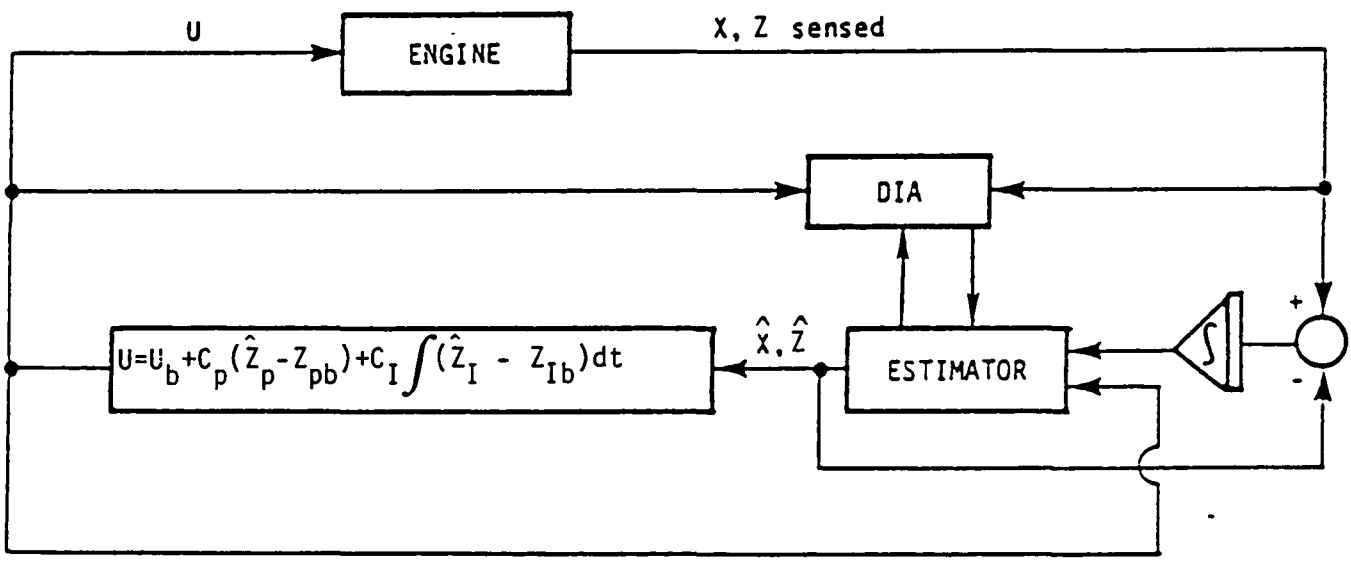

Figure 5-5 DIA Algorithm Revision 3

where $\tilde{X} = \hat{X} - X$ and $\tilde{b} = \hat{b} - b$. The filter gains were designed using the model from equation (5). The criteria followed in the integral gain design was to place integrator roots so that they are slower than the estimator roots with no integrators.

For the baseline DIA algorithm and for Revisions 1 and 2, the detection and isolation thresholds were chosen to be large to encompass modelling errors. Since the modelling errors are 'eliminated' in Revision 3, the detection threshold was made smaller. The isolation threshold was unchanged because integrators were not incorporated into the bank of isolation filters. As a result of the smaller residuals, the time to detect a failure in Revision 3 has improved as can be seen in Table 5-1.

TABLE 5-1

COMPARISON OF THE DETECTION AND ISOLATION TIMES
FOR THE THREE REVISIONS

(i) Flight Condition - 0/0/36
Failure Mode - PT4 soft failure 15 PSI/sec at 0.1 seconds

	Time to Detect	Time to Isolate
Revision 1	2.892	0.122
Revision 2	2.962	0.114
Revision 3	0.716	1.86

(ii) Flight Condition - 20K/.3/83
Failure Mode - PT6 drift of 2 PSI/second at 0.1 seconds

	Time to Detect	Time to Isolate
Revision 1	2.524	0.226
Revision 2	2.490	0.260
Revision 3	0.486	2.190

(iii) Flight Condition - 45K/.9/83
Failure Mode - PT4 drift of 20 PSI/second at 0.1 seconds

	Time to Detect	Time to Isolate
Revision 1	1.996	0.160
Revision 2	2.028	0.156
Revision 3	0.496	1.492

The reason for the higher isolation time for Revision 3 is as follows. In Revisions 1 and 2 the detection filter residuals are high. After detection of a soft failure, the isolation filters are initialized to the outputs of the detection filters so that isolation filter residuals are also high. From this

initial condition the residuals grow at each time step and finally cross the thresholds (failure isolation), as shown in Figure 5-6. In Revision 3 the isolation filter residuals are initially very small and therefore take a longer time, than the residuals of Revisions 1 and 2, to cross the isolation thresholds (Figure 5-7).

Once a sensor failure is detected, isolated and accommodated, the magnitude of the detection thresholds must be increased to accommodate the larger residuals which have built up. If this is not done, false alarms will result. The detection threshold is maintained at the larger value until the added integrator logic in the estimator decreases the residuals. Any faulty measurements are eliminated from the integral portion of the estimator logic.

The responses of the engine and the estimator with Revision 3, are shown in Figure 5-8 for the no-failure case at the flight condition 0/0/36. The parameters plotted are the same as those shown in the plots for Revisions 1 and 2. The small transient seen is caused by the initialization of the simulation. The residual errors between the engine outputs and the estimator outputs are zero.

5.2 COMPARISON OF DIA ALGORITHM REVISIONS

This section presents a qualitative and quantitative comparison of the features of the three DIA algorithm revisions. The qualitative comparison includes complexity, and transient response of the closed loop system to failures. The quantitative comparison includes tabulation of the errors from engine outputs to reference points, and errors from engine outputs to estimator outputs (residuals).

5.2.1 Complexity

Revision 1 is the least complex of the three revisions. It involves switching from sensed values to estimates in case of a failure whereas sensed values are used in the case of no failure. Revision 2 requires splitting the control law into two parts, proportional and integral, which work on estimates and sensors, respectively. The level of complexity is slightly higher than Revision 1. Revision 3 requires design of integral gains and a higher order model for the estimator. It is the most complex of all the three revisions.

5.2.2 Steady State Errors (No Failure)

Steady state errors were compared to evaluate the DIA/Control interactions in the absence of a failure.

The three revisions were compared by tabulating the following differences:

i) Difference between actual engine outputs and the reference point schedules. This provides a gross check on the operating point.

ii) Difference between actual engine outputs and the estimates (residuals). This indicates whether the revision has a positive or negative impact on the magnitude of inherent modelling errors.

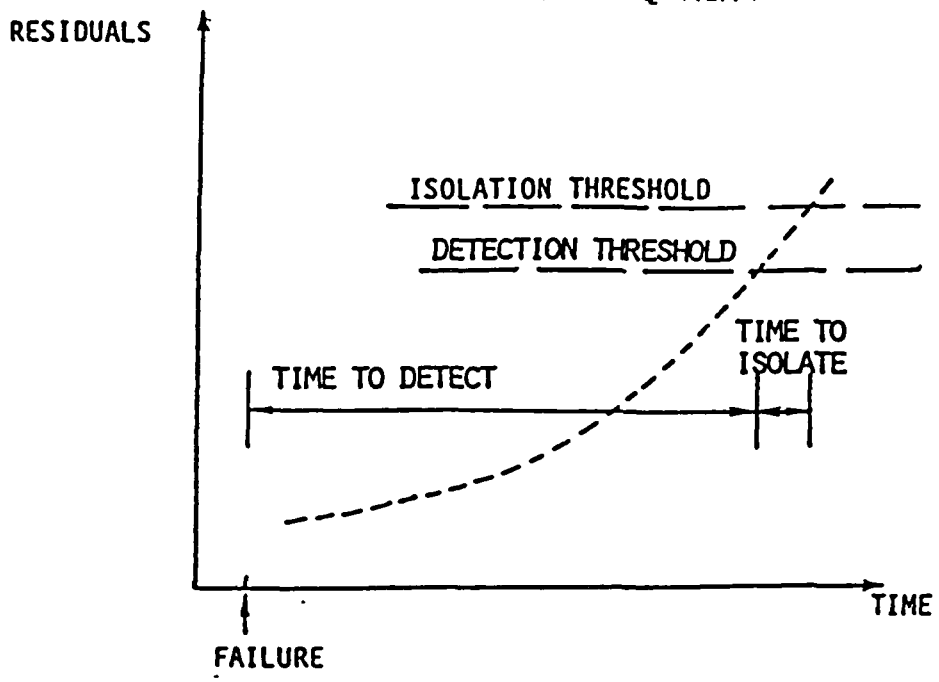

Figure 5-6 Time History of the Residuals in Revisions 1 and 2

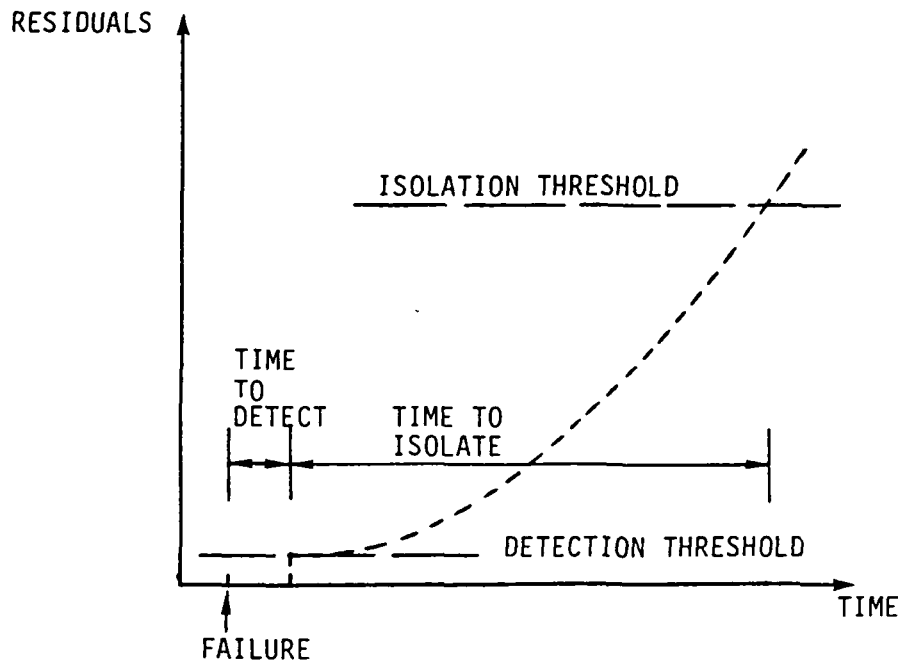

Figure 5-7 Time History of the Residuals in Revision 3

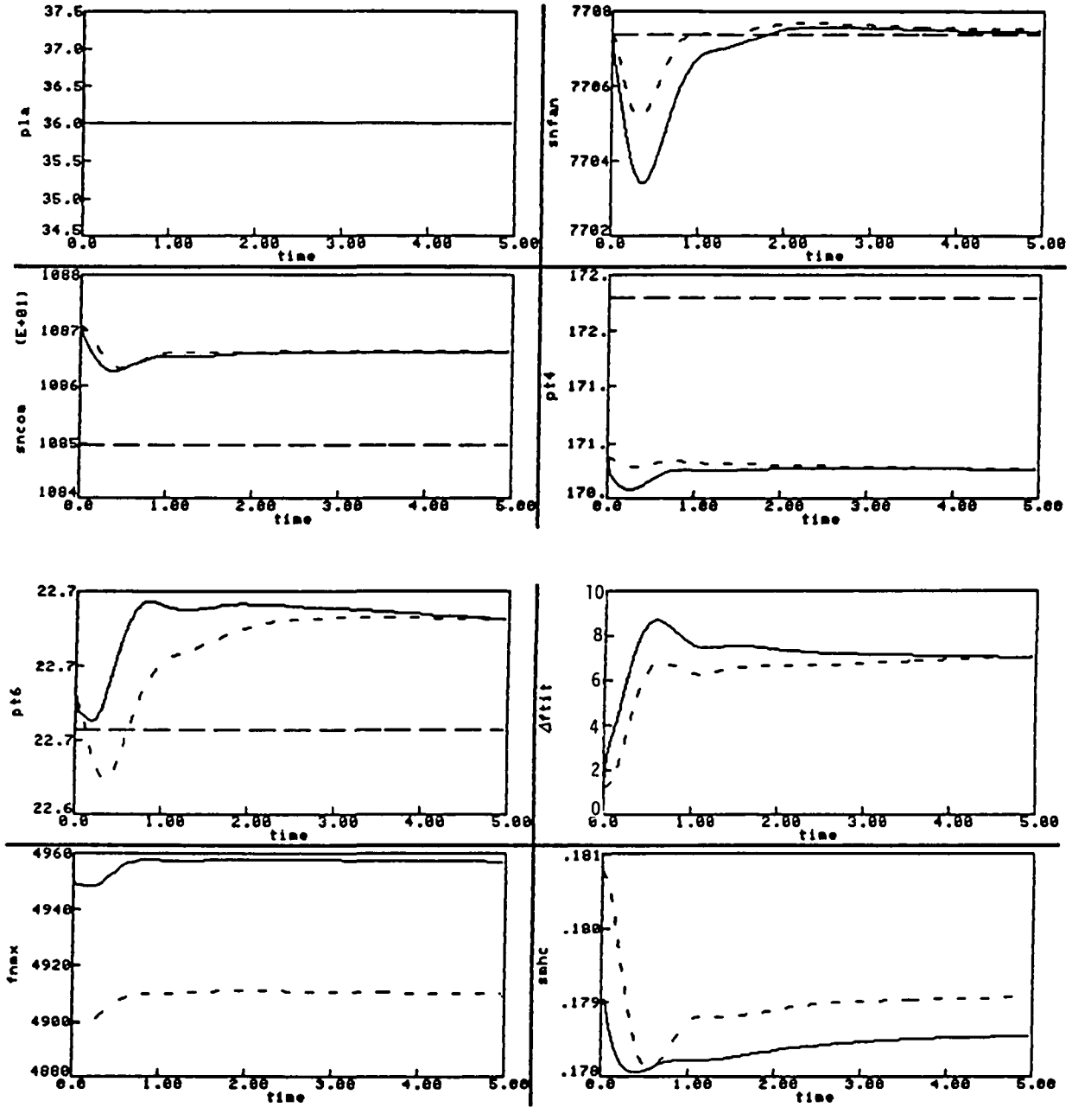

Figure 5-8 Steady State Results for Revision 3 with No Failure at the Flight Condition OK/OM, PLA = 36.0 Degrees. Engine (————), Estimate (— — — —), Reference (——— ———)

These differences were evaluated for a no-failure case at the flight point of altitude = 0 ft., Mach no. = 0, PLA = 36 degrees. The failure induced was a hard failure of +1000 RPM bias in the N1 sensor at 1.0 seconds (Figures 5-9b, c, and d respectively, for each revision). Results for the baseline DIA algorithm (without any revisions) are also included for comparison.

The Tables 5-2a and 5-2b contain the above mentioned differences for the no-failure case. It can be seen from Table 5-2a that in Revisions 1, 2 and 3, N1 and PT6 are very close to the reference point; i.e., the engine operating points are approximately the same for all three revisions. As expected the baseline DIA algorithm exhibits larger errors. Table 5-2b clearly demonstrates that with Revision 3 the residual errors are zero because of the trim integrators in the estimator. The estimation errors for Revisions 1 and 2 are comparable to the baseline DIA algorithm.

TABLE 5-2a

COMPARISON OF STEADY STATE ERRORS FOR THE THREE REVISIONS AND THE BASELINE DIA ALGORITHM

FLIGHT CONDITION: ALT = 0 FT, M = 0, PLA = 36
FAILURE MODE: NO FAILURE

	BASELINE DIA	REVISION 1	REVISION 2	REVISION 3
SNFAN-SNFSCH	-43.6 (.57)	0.1 (ϵ)	0.1 (ϵ)	0.1 (ϵ)
SNCOM-SNCSCH	35. (.32)	16. (0.15)	15. (0.14)	16. (0.15)
PT4-PT4SCH	-.37 (.22)	-1.53 (.89)	-1.56 (0.91)	-1.53 (0.89)
PT6-PT6SCH	0.433 (1.91)	0.015 (0.07)	0.01 (0.04)	0.015 (0.07)
FTIT-FTITSH	24.3 (1.64)	18.33 (1.24)	18.43 (1.24)	18.43 (1.24)
FNMX-$FNMX_{NOM}$	106. (2.14)	0. (0.)	-1.5 (0.03)	0.3 (ϵ)
SMHC-$SMHC_{NOM}$	0.0011 (0.59)	0. (0.)	-0.0004 (0.19)	-0.00002 (0.01)

(.) ARE PERCENTACES OF SCHEDULED VALUES
ϵ DENOTES A NUMBER APPROACHING ZERO

TABLE 5-2b

COMPARISON OF STEADY STATE ESTIMATION ERRORS FOR THE THREE REVISIONS AND THE BASELINE DIA ALGORITHM

FLIGHT CONDITION: ALT = 0 FT, M = 0, PLA = 36
FAILURE MODE: NO FAILURE

	BASELINE DIA	REVISION 1	REVISION 2	REVISION 3
SNFAN-SNFEST	-43.6 (.57)	-47.7 (0.62)	-45.8 (0.59)	$\epsilon(\epsilon)$
SNCOM-SNCEST	18. (0.17)	19. (0.18)	18. (0.17)	$\epsilon(\epsilon)$
PT4-PT4EST	-1.75 (1.02)	-1.64 (0.95)	-1.7 (0.99)	$\epsilon(\epsilon)$
PT6-PT6EST	0.431 (1.9)	0.43 (1.91)	0.409 (1.80)	$\epsilon(\epsilon)$
FTIT-FTIEST	-1. (0.07)	-4.4 (0.29)	-3.7 (0.25)	$\epsilon(\epsilon)$
FNMX-FNMXEST	60.2 (1.21)	47.5 (0.96)	43.7 (0.88)	47.6 (0.96)
SMHC-SMHCEST	-0.0013 (0.73)	-0.0005 (0.29)	-0.0009 (0.48)	-0.0005 (0.29)

(.) ARE PERCENTAGES OF SCHEDULED VALUES
ϵ DENOTES A NUMBER APPROACHING ZERO

Overall comparison of the revisions using Tables 5-2a and 5-2b does not show a clear winner. All three revisions accomplish the goal of eliminating the effect of estimator hangoff errors on the engine operating point. Other variations in the differences shown in the tables are not judged to be significant enough to select one revision over the other two.

5.2.3 Failure Transients

The flight conditions and the failure modes for which failure transients were evaluated for the three revisions were evaluated are listed in the following Table.

	Flight Condition	Failed Channel	Rate of Drift
(i)	0/0/36	N1	+1000 RPM (jump)
(ii)	0/0/36	N2	+1000 RPM (jump)
(iii)	0/0/36	N1	+5000 RPM/sec
(iv)	0/0/36	PT4	+15 PSI/sec
(v)	45K/.9/83	PT6	+2 PSI/sec
(vi)	45K/.9/83	PT4	+20 PSI/sec
(vii)	20K/.3/83	N2	+2000 RPM/sec

The results for each of the above failures modes for each revision are presented below.

5.2.3.1 N1 Hard Failure At The Flight Condition 0/0/36

A failure of +1000 RPM was induced in the N1 sensor at t=1.0 second for the flight condition 0/0/36. In the baseline DIA algorithm a hard failure is detected and isolated at the same time. All three revisions detected and isolated the failure as a hard failure and all took the same length of time to detect and isolate. No false alarms were detected. The time to detect was 0.002 seconds, which is the cycle time of the simulation. Figures 5-9a through 5-9d show the failure transients for the baseline DIA algorithm and for each revision. These figures consist of the time histories of PLA, fan speed (SNFAN or N1), compressor speed (SNCOM or N2), burner pressure (PT4), augmentor pressure (PT6), fan turbine inlet temperature (FTIT), net thrust (FNMX), compressor surge margin (SMHC), fuel flow (WF),and nozzle area (AJ).

In general, the transient results for the $\hat{N1}$ failure are comparable among the three revisions and the baseline DIA algorithm. In Revisions 1 and 2, the estimate of N1 ($\hat{N1}$) is higher than its reference point. When $\hat{N1}$ is substituted for N1, the control cuts down on fuel flow to bring $\hat{N1}$ to the reference point. This causes the engine to 'slow down' as can be seen in Figures 5-9b and 5-9c. In Revision 3, $\hat{N1}$ is equal to N1. When the failure is isolated the integrator which takes the residual ($\hat{N1}$-N1) to zero is turned off. The biased estimate of N1 causes the engine to 'slow down' as shown in Figure 5-9d.

The 'hump' in the estimator response is caused primarily by the zeroing of the first column of the filter gain matrix which is done to accommodate the N1 failure. Before the failure, the filter equation is written as follows.

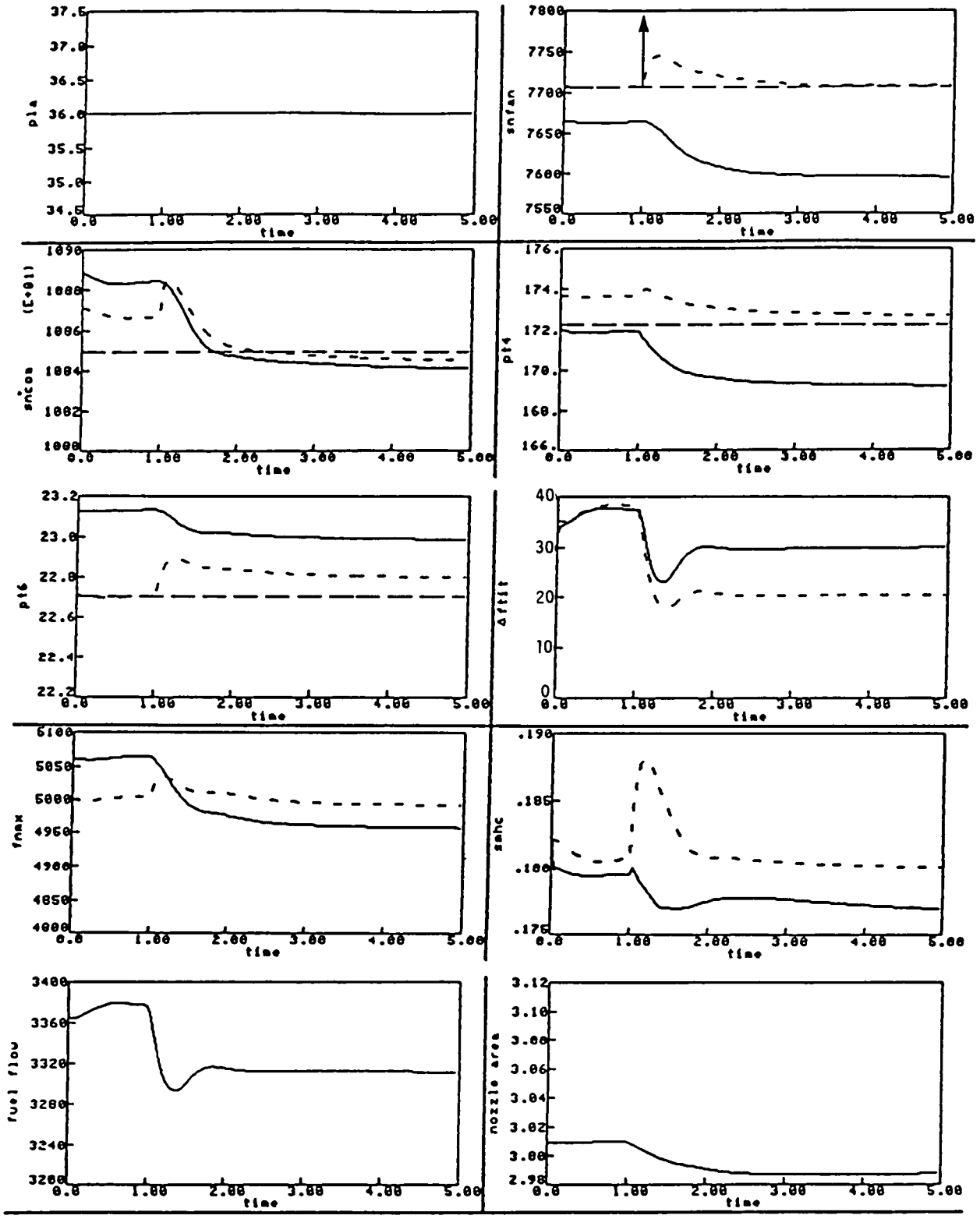

Figure 5-9a Transient Results for Baseline DIA with N1 Hard Failure (+1000 rpm Step) at the Flight Condition OK/OM, PLA = 36.0 degrees. Engine (————), Estimate (— — — —), Reference (——— ———)

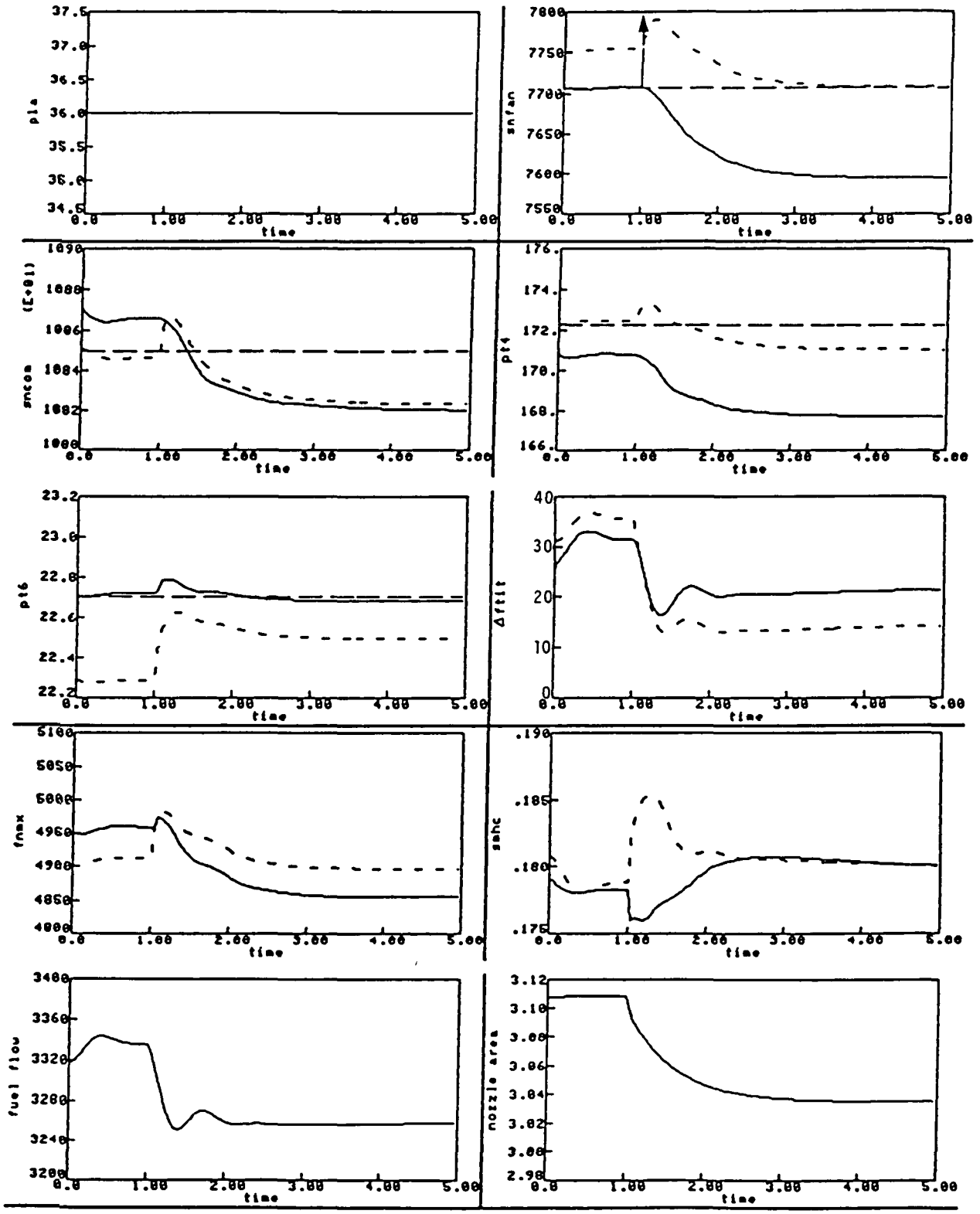

Figure 5-9b Transient Results for Revision 1 with N1 Hard Failure (+1000 rpm Step) at the Flight Condition OK/OM, PLA = 36.0 degrees. Engine (————), Estimate (— — — —), Reference (——— ———)

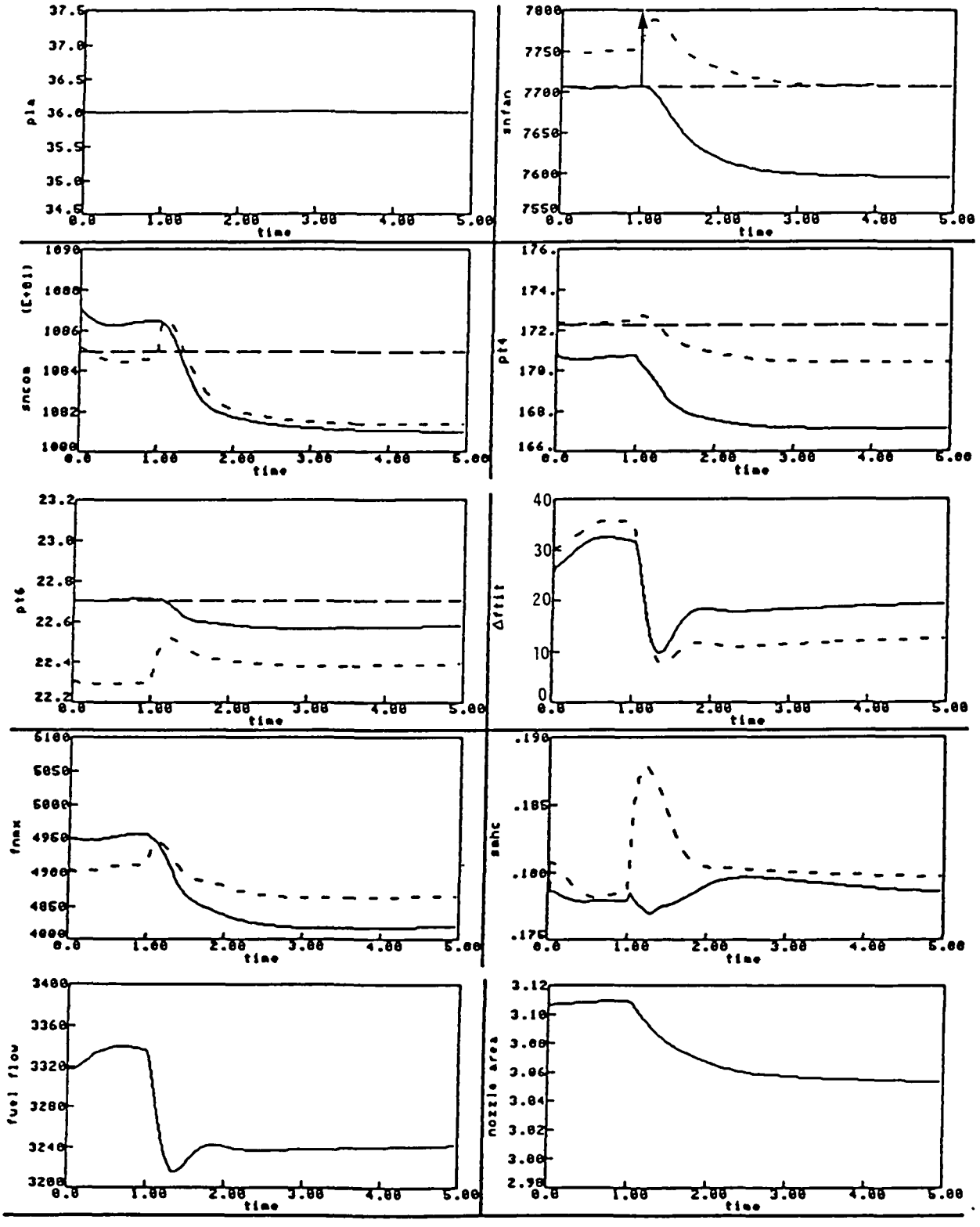

Figure 5-9c Transient Results for Revision 2 with N1 Hard Failure (+1000 rpm Step) at the Flight Condition OK/OM, PLA = 36.0 degrees. Engine (————), Estimate (— — — —), Reference (———— ————)

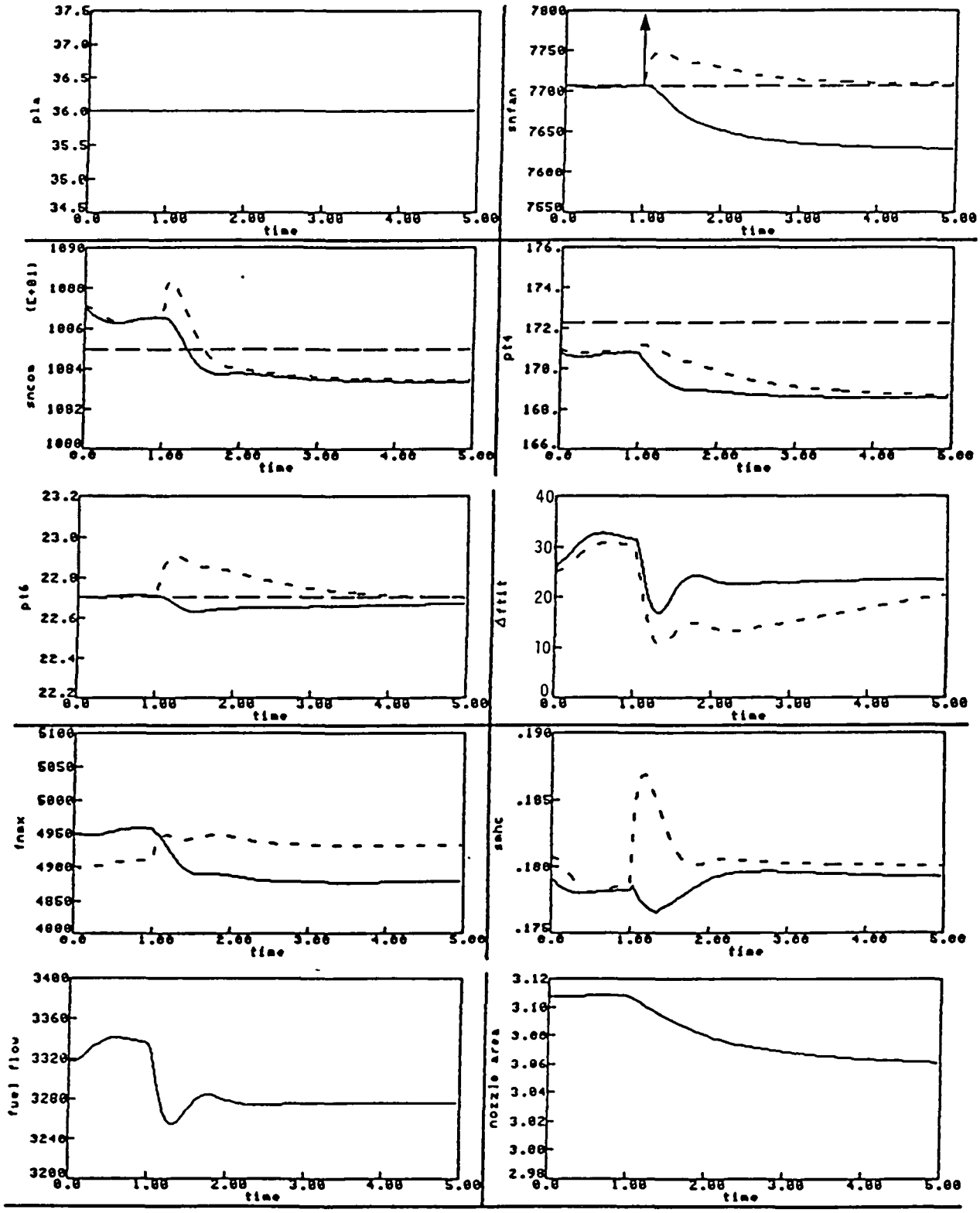

Figure 5-9d Transient Results for Revision 3 with N1 Hard Failure (+1000 rpm Step) at the Flight Condition OK/OM, PLA = 36.0 degrees. Engine (————), Estimate (— — — —), Reference (———— ————)

$$\delta \dot{\hat{X}} = F\delta\hat{X} + G\,\delta U + [K_1 \quad K_2 \quad K_3 \quad K_4 \quad K_5]\ (Z-Z)$$

where δ's are perturbations away from the nominal and

K_i are columns of the K matrix. After the N1 failure is isolated, the first column of the K matrix is made zero which results in a step input, as shown in the following equation.

$$\delta \dot{\hat{X}} = F\delta\hat{X} + G\,\delta U + [K_1 \quad K_2 \quad K_3 \quad K_4 \quad K_5]\ (Z-\hat{Z})$$

$$- [K_1 \quad 0 \quad 0 \quad 0 \quad 0]\ (Z-\hat{Z})\cdot 1(t-t_f)$$

where t_f is the time at which the step input is applied. This is demonstrated in Figure 5-10 for a case with no failure, where the first column of the K matrix was made zero at t=1.0 seconds. Thus, the upward excursion in the N1, N2, PT4, and PT6 outputs at t=1.0 seconds in Figure 5-9 is the effect of making the first column of the K matrix zero. The downward trend at the later time is the control system reaction trying to bring N1 to its reference point.

The control excursions for Revision 2 (Figure 5-9c) are larger than for Revision 1 (Figure 5-9b). In Revision 2 the change in control is caused by the change in all estimates, which feed back to the LQR portion of the control mode, caused by zeroing the first column of the K matrix. This causes a larger excursion than that for Revision 1 since in Revision 1 only the estimated N1 is substituted for actual N1 in the LQR portion of the control mode, as shown in the following.

$$\delta U_{f-} = [C_p] \begin{bmatrix} \delta N1 \\ \delta N2 \\ \delta PT4 \\ \delta PT6 \\ \delta FTIT \end{bmatrix}$$

After the failure, $\hat{N1}$ is substituted for N1, and the control is given by the following equation.

$$\delta U_{f+} = [C_p] \begin{bmatrix} \delta N1 \\ \delta N2 \\ \delta PT4 \\ \delta PT6 \\ \delta FTIT \end{bmatrix} + [C_p] \begin{bmatrix} (\delta\hat{N1}-\delta N1) \\ 0 \\ 0 \\ 0 \\ 0 \end{bmatrix} \cdot 1(t-t_f)$$

where δU_{f+} is the change in control after the failure is accommodated at time t^f and $1(t-t^f)$ is the step applied at the time the failure is accommodated.

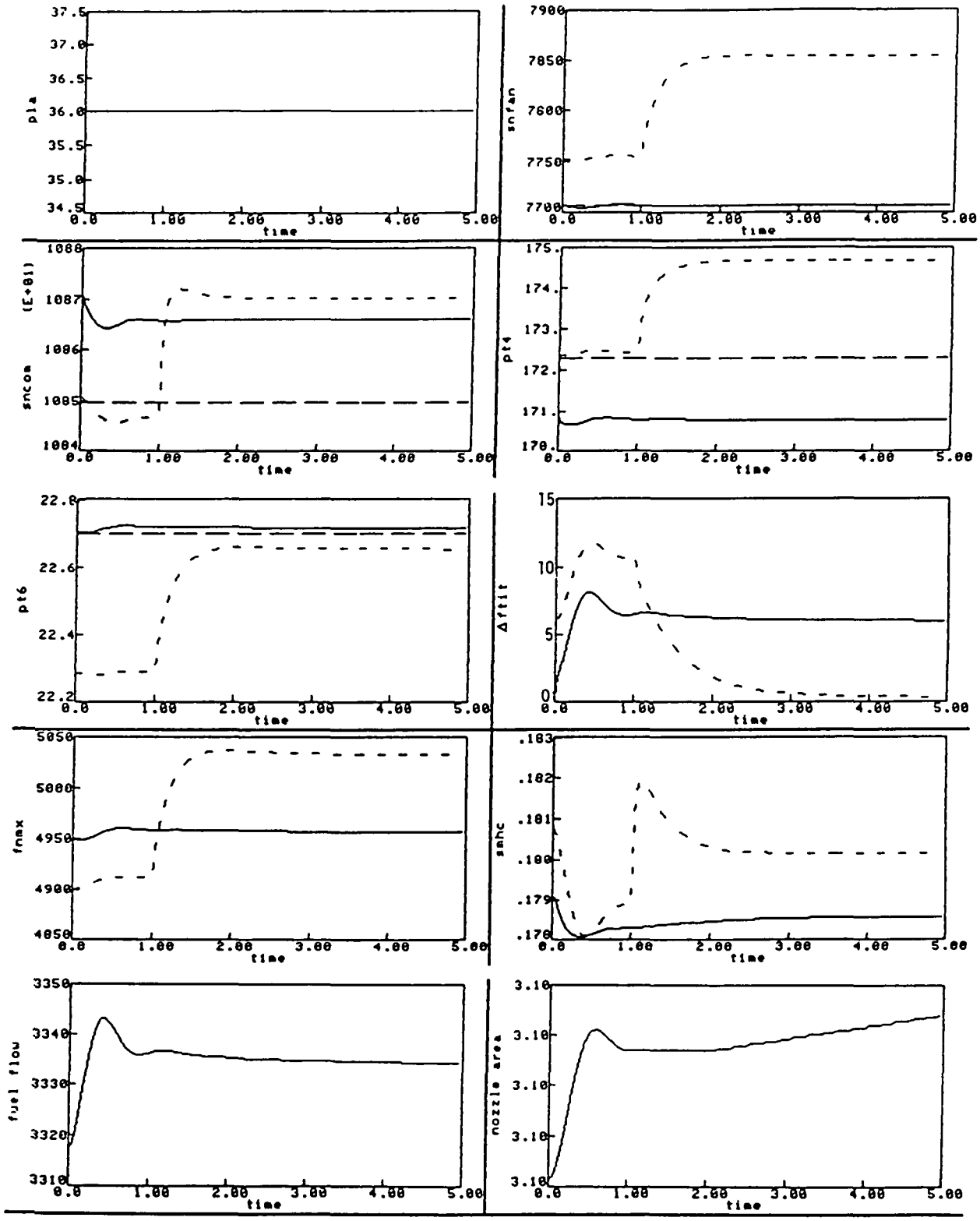

Figure 5-10 Transient Results for No Failure Case with First Column of Filter Gain Matrix Zeroed at t=1.second; at the Flight Condition OK/OM, PLA = 36.0 degrees. Engine (————), Estimate (— — — —), Reference (——— ———)

5.2.3.2 N2 Hard Failure At The Flight Condition 0/0/36

An N2 hard failure of +1000 RPM was induced at t=1.0 seconds at the flight condition 0/0/36. All the revisions detected and isolated the failure as an N2 hard failure at t=1.002 seconds (cycle time of the simulation). Figures 5-11a through 5-11c show the responses of engine and estimator outputs for each revision. The failure transients for Revisions 2 and 3 are comparable and are smoother compared to those for Revision 1.

5.2.3.3 N1 High Drift Rate Failure At The Flight Condition 0/0/36

An N1 failure of +5000 RPM/second (fast rate drift) was induced at t=0.1 seconds and each revision tested for its response. Figures 5-12a through 5-12c present the failure transients for each revision. It is observed that Revision 3 demonstrates slightly more degradation in the failed channel (N1) compared to Revisions 1 and 2. Other than this and the fact that the responses for Revision 1 are somewhat more oscillatory than those for Revisions 2 and 3, the performance of the three revisions are pretty much comparable.

5.2.3.4 PT4 Drift Failure At The Flight Condition 0/0/36

Another failure case of a slow drift rate was simulated. This failure has a drift rate of +15 PSI/second in the PT4 sensor induced at 0.1 seconds for flight condition 0/0/36. The failure transients of each revision are shown in Figures 5-13a through 5-13c. The failure detection and isolation properties of each revision are as follows.

	Time to Detect	Time to Isolate	False Alarm	Misses
Revision 1	2.892	0.122	none	none
Revision 2	2.962	0.114	none	none
Revision 3	0.716	1.86	none	none

Revision 3 takes a relatively short time to detect the failure since the detection threshold is small compared to Revisions 1 and 2. However it takes longer to isolate the failure after detection. Total time to detect and isolate the failure is slightly better for Revision 3 then for Revisions 1 and 2.

It is observed from Figures 5-13a through 5-13c that Revision 2 is least affected by the failure. Note that the three figures are plotted on the same scale. If the results for Revision 2 are plotted on an expanded scale (Figure 5-14), the accommodation transient can be seen. It is much smaller in magnitude compared to the accommodation transients of Revisions 1 and 3.

It is observed from Figure 5-13c that Revision 3 responses approach steady state conditions somewhat slower than Revisions 1 and 2, due to the additional trim integrators in the estimator. As noted earlier, the slow response of these various transients is attributed to the long time constant of the integral trim logic in the multivariable control. This was verified by

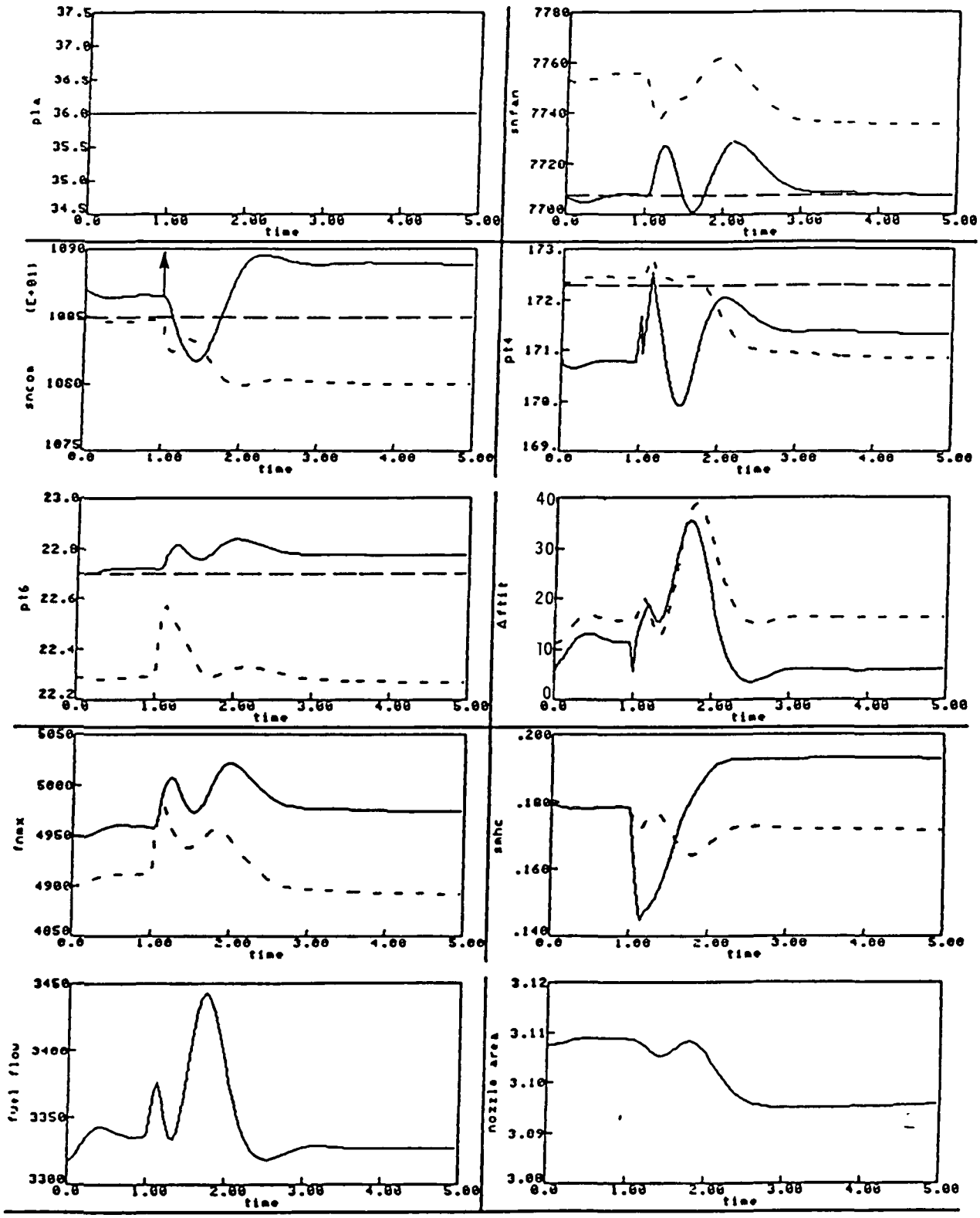

Figure 5-11a Transient Results for Revision 1 with N2 Hard Failure (+1000 rpm Step) at the Flight Condition OK/OM, PLA = 36.0 degrees. Engine (————), Estimate (— — — —), Reference (——— ———)

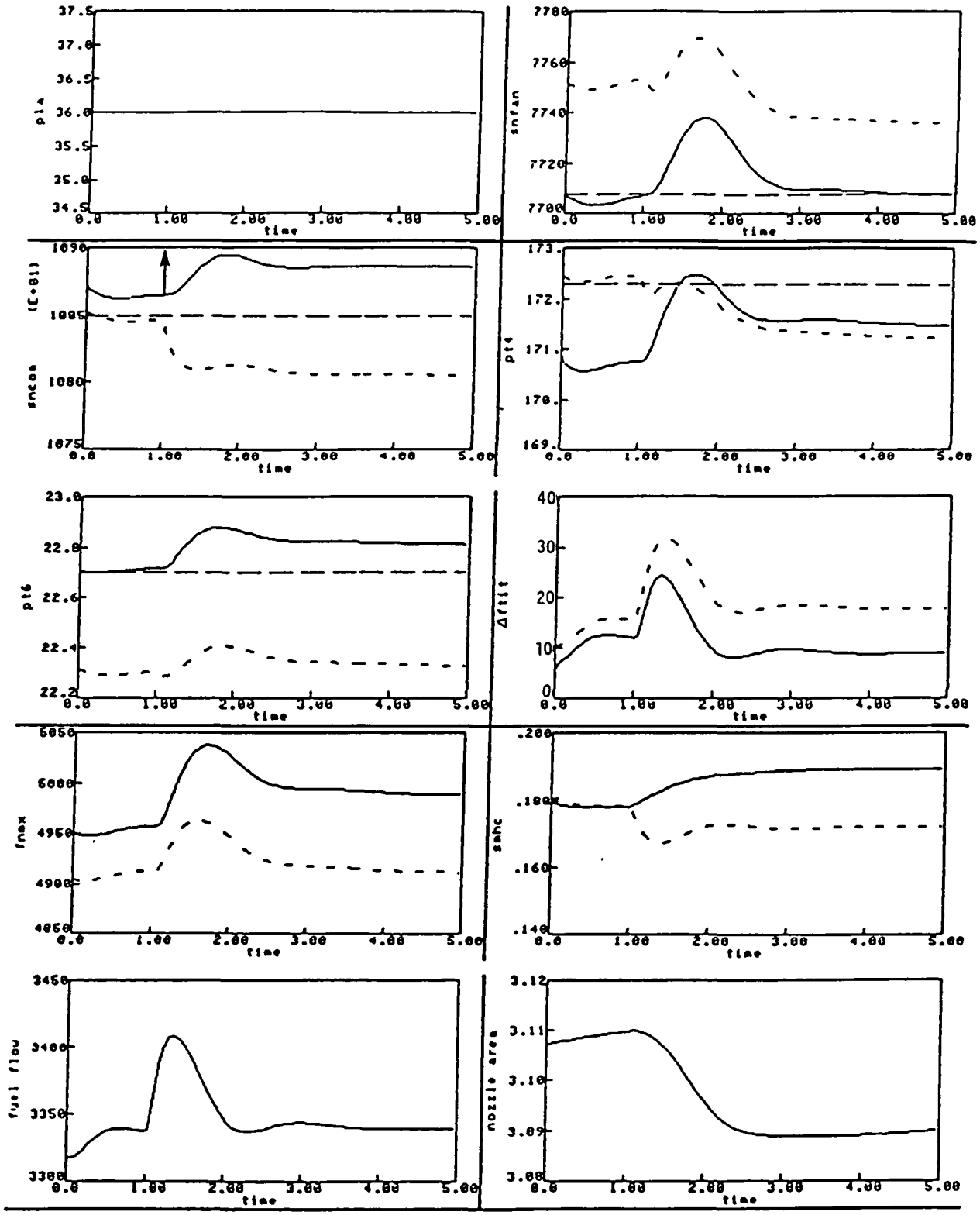

Figure 5-11b Transient Results for Revision 2 with N2 Hard Failure (+1000 rpm Step) at the Flight Condition 20K/0.3M, PLA = 83.0 degrees. Engine (————), Estimate (— — — —), Reference (——— ———)

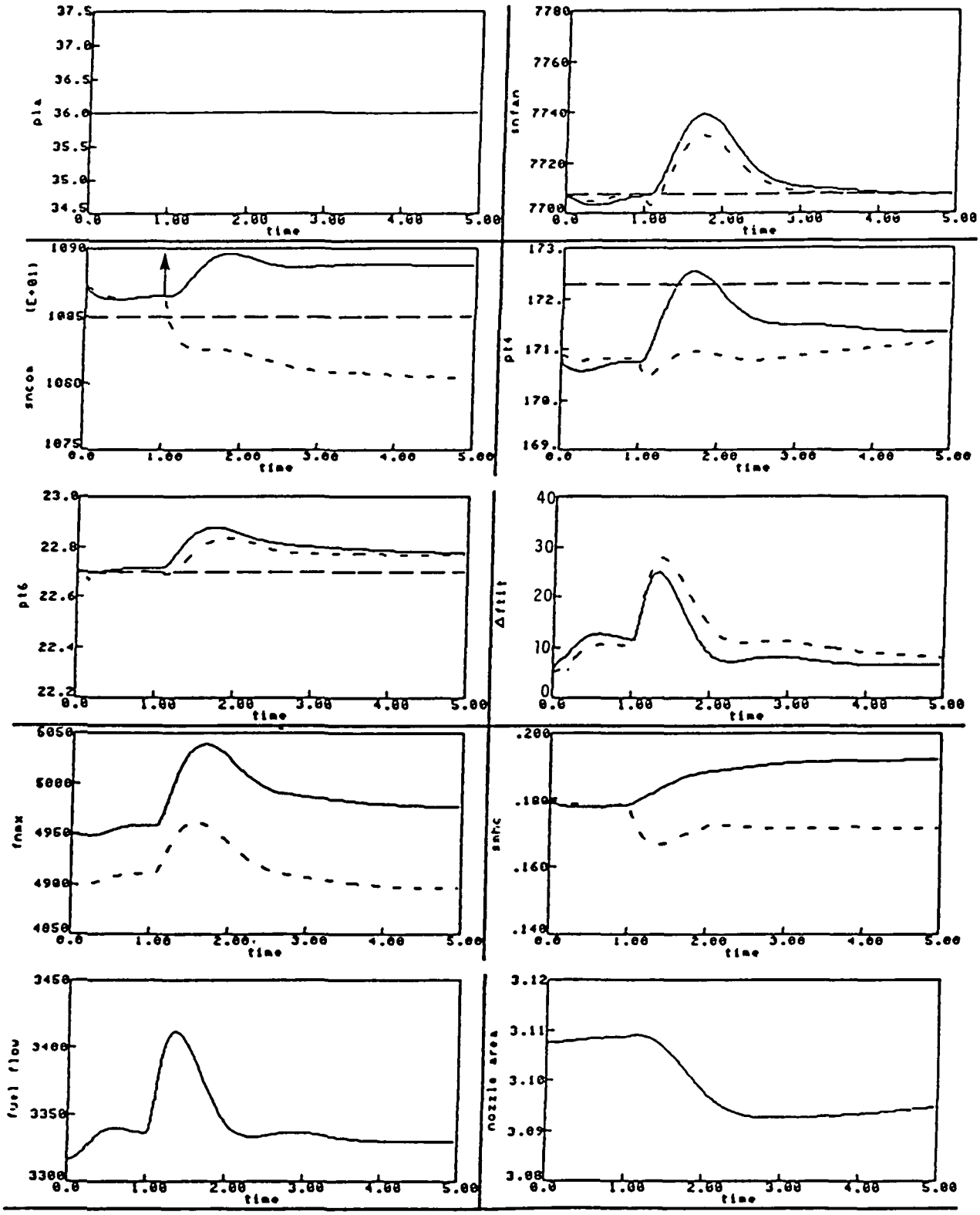

Figure 5-11c Transient Results for Revision 3 with N2 Hard Failure (+1000 rpm Step) at the Flight Condition OK/OM, PLA = 36.0 degrees. Engine (————), Estimate (— — — —), Reference (——— ———)

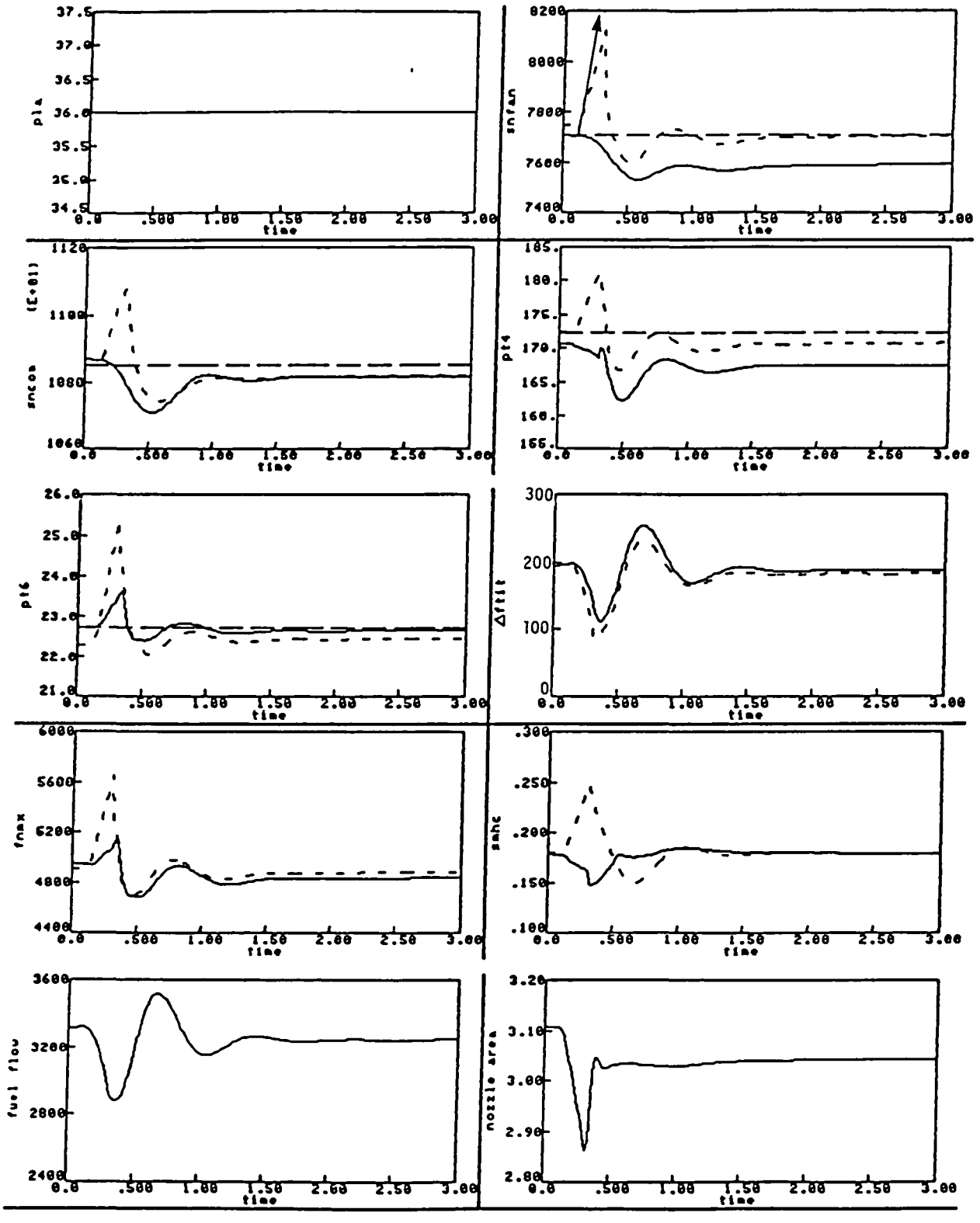

Figure 5-12a Transient Results for Revision 1 with N1 Hard Failure (+5000 rpm/Second) at the Flight Condition OK/OM, PLA = 36.0 degrees. Engine (————), Estimate (— — — —), Reference (——— ———)

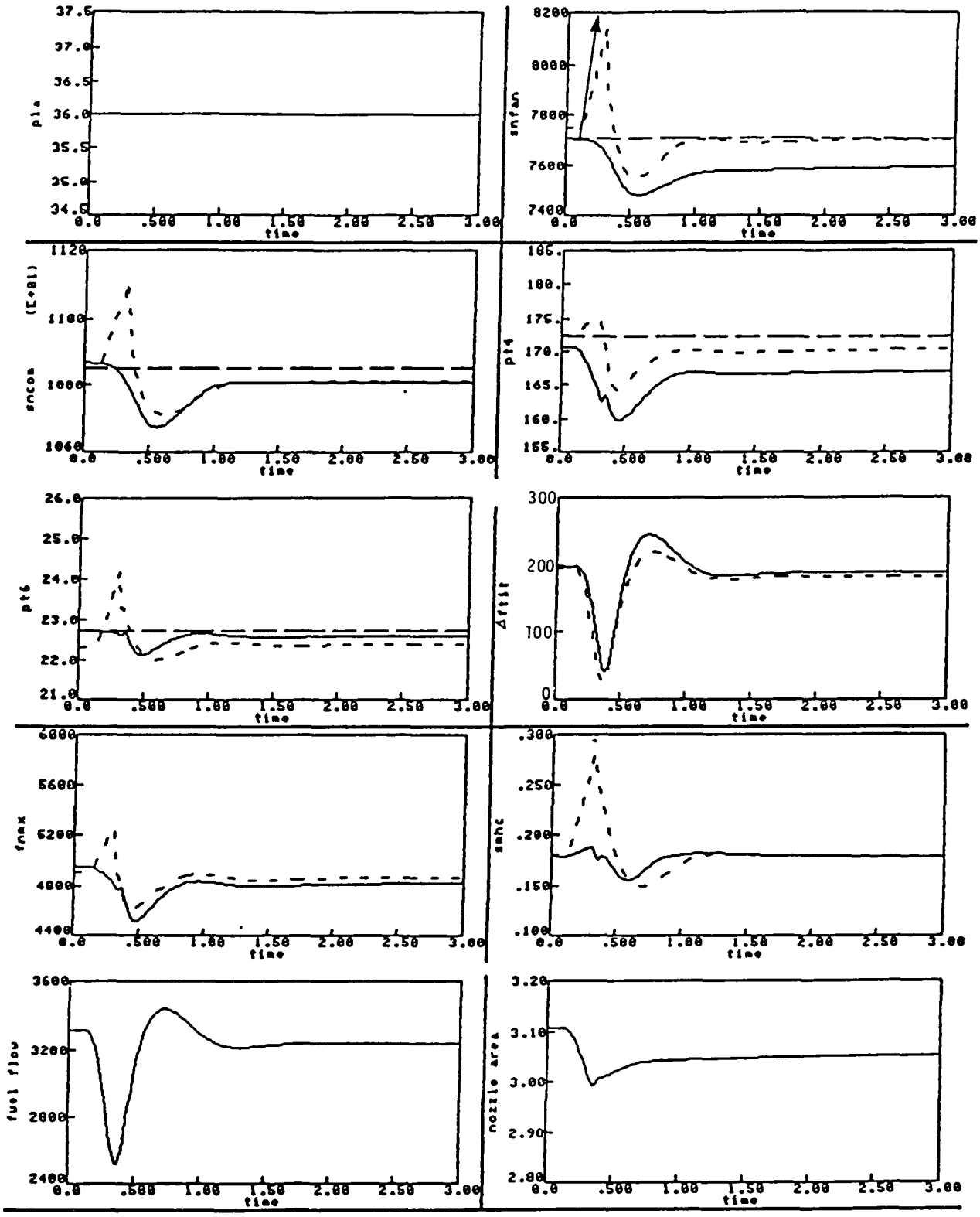

Figure 5-12b Transient Results for Revision 2 with N1 Hard Failure (+5000 rpm/ Second) at the Flight Condition OK/OM, PLA = 36.0 degrees. Engine (————), Estimate (— — — —), Reference (——— ———)

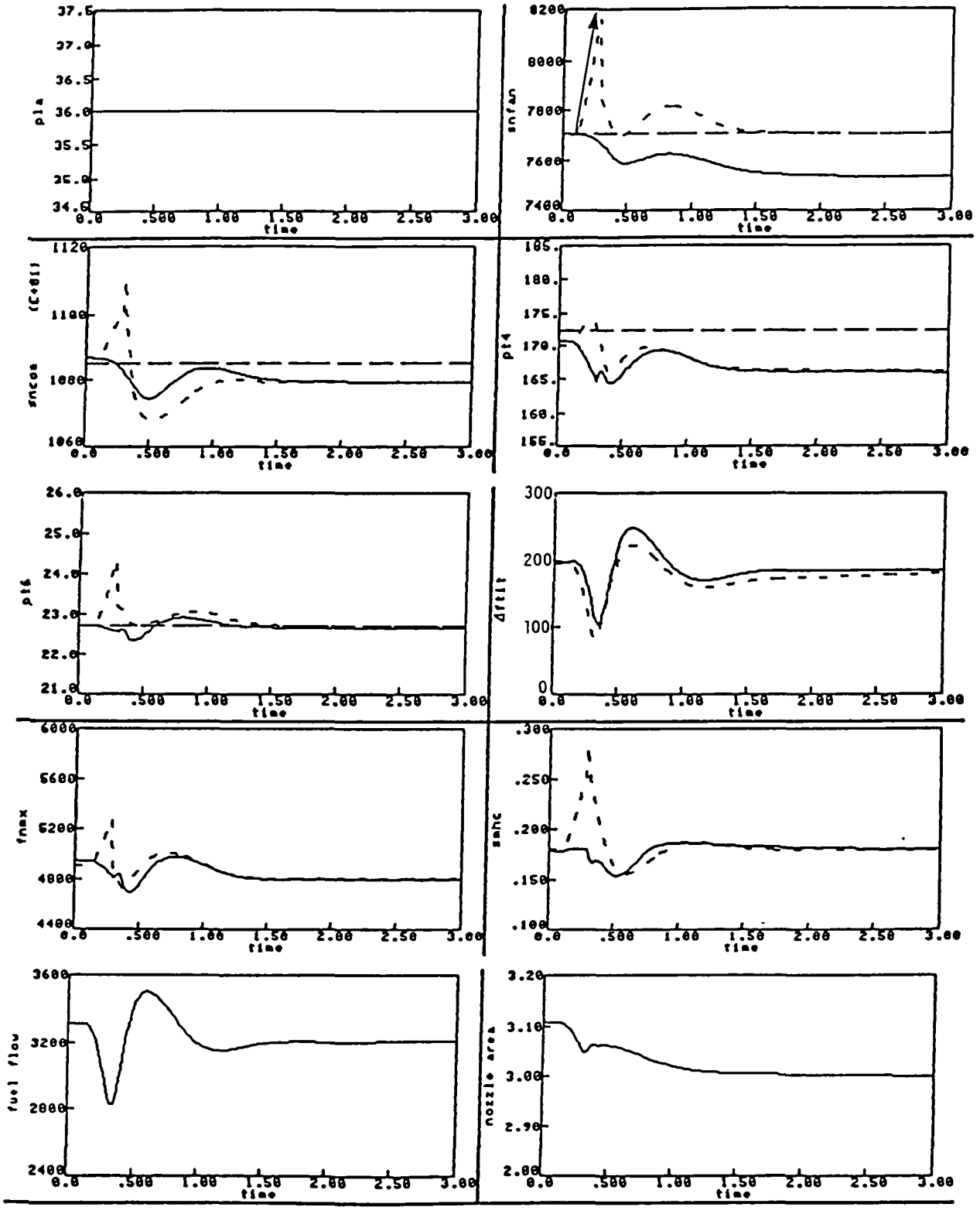

Figure 5-12c Transient Results for Revision 3 with N1 Hard Failure (+5000 rpm/Second) at the Flight Condition OK/OM, PLA = 36.0 degrees. Engine (————) Estimate (— — — —), Reference (———— ————)

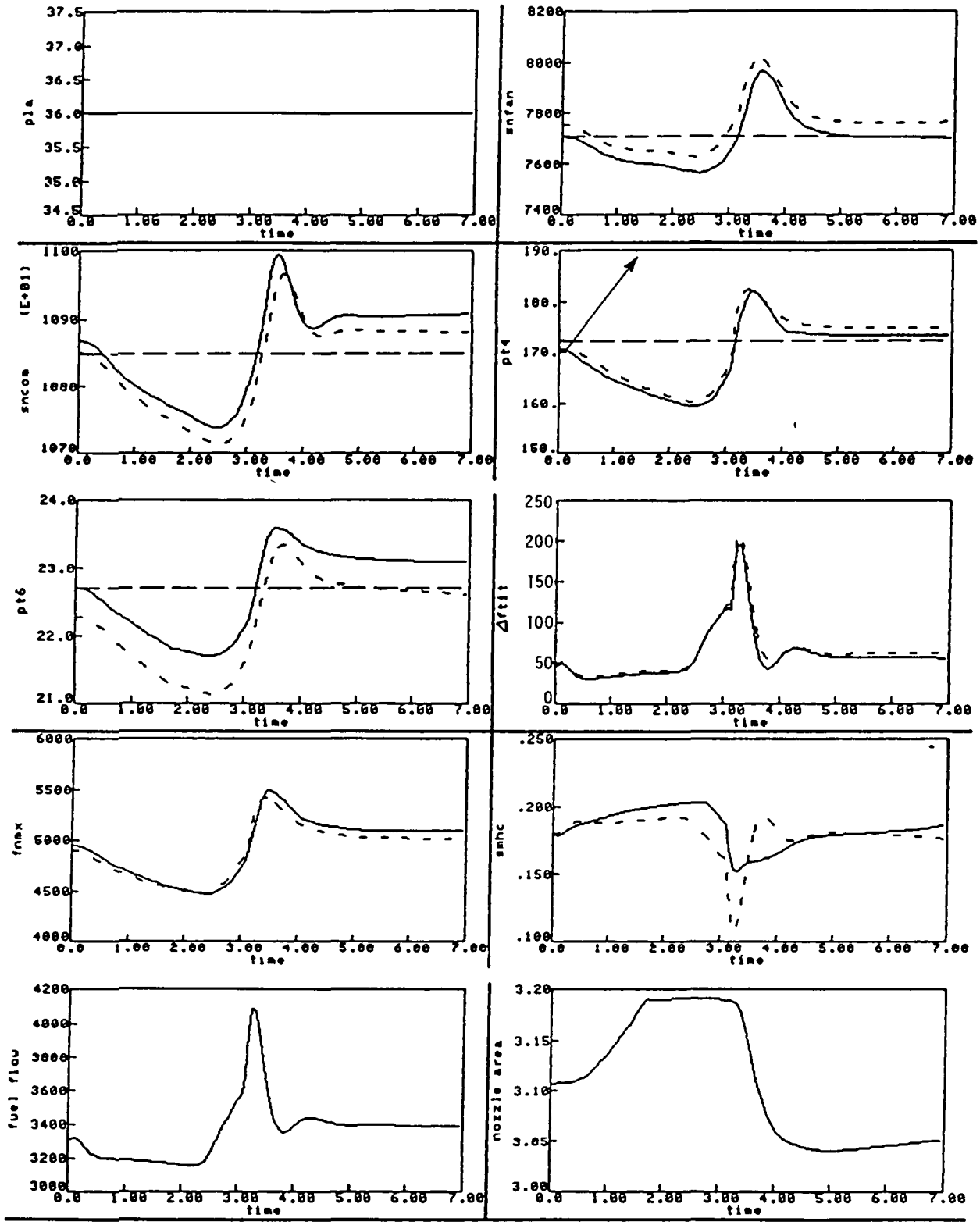

Figure 5-13a Transient Results for Revision 1 with PT4 Failure (+15 psia/second) at the Flight Condition OK/OM, PLA = 36.0 degrees Engine (————), Estimate (— — — —), Reference (—— ——)

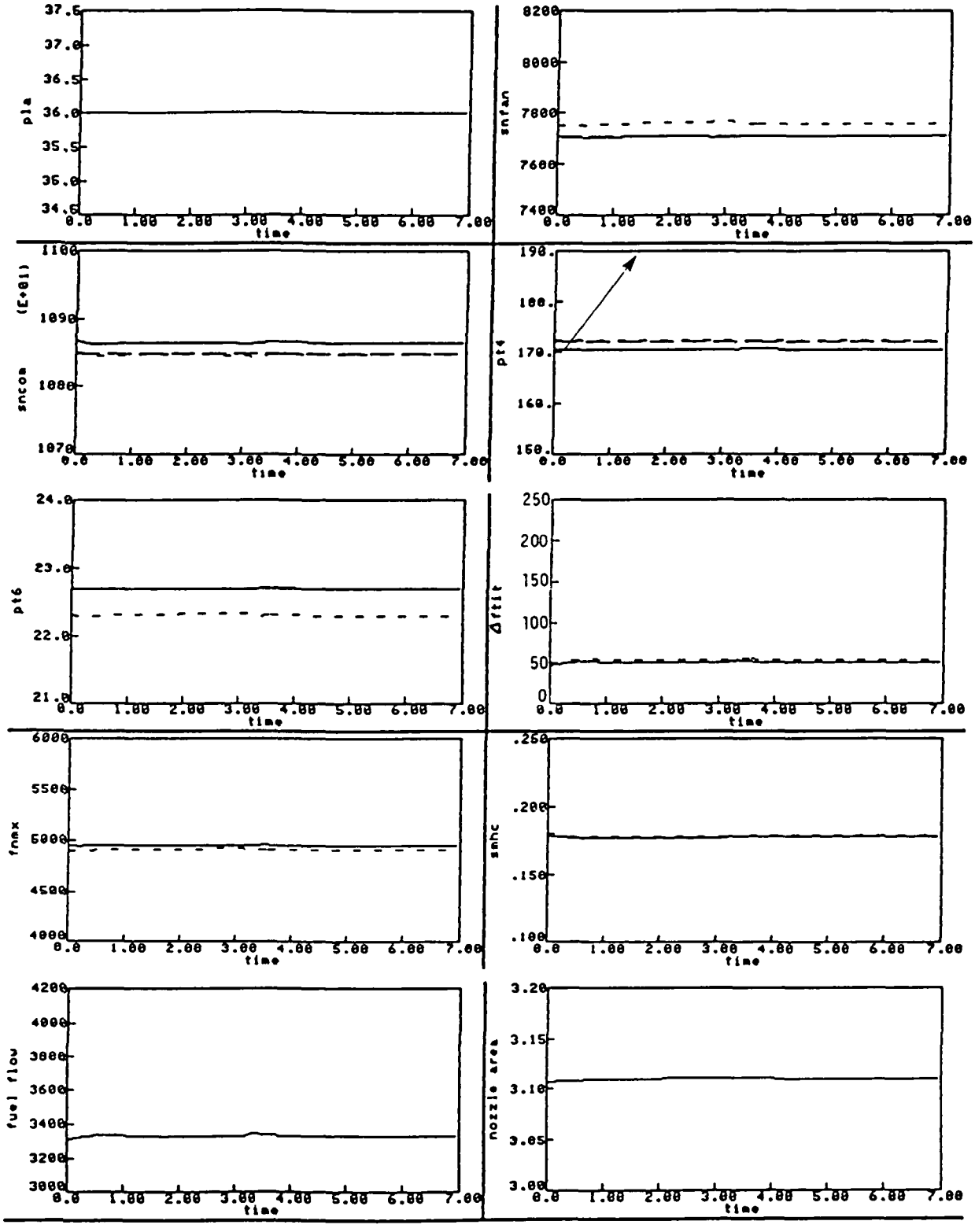

Figure 5-13b Transient Results for Revision 2 with PT4 Failure (+15 psia/second) at the Flight Condition OK/OM, PLA = 36.0 degrees Engine (————), Estimate (— — — —), Reference (——— ———)

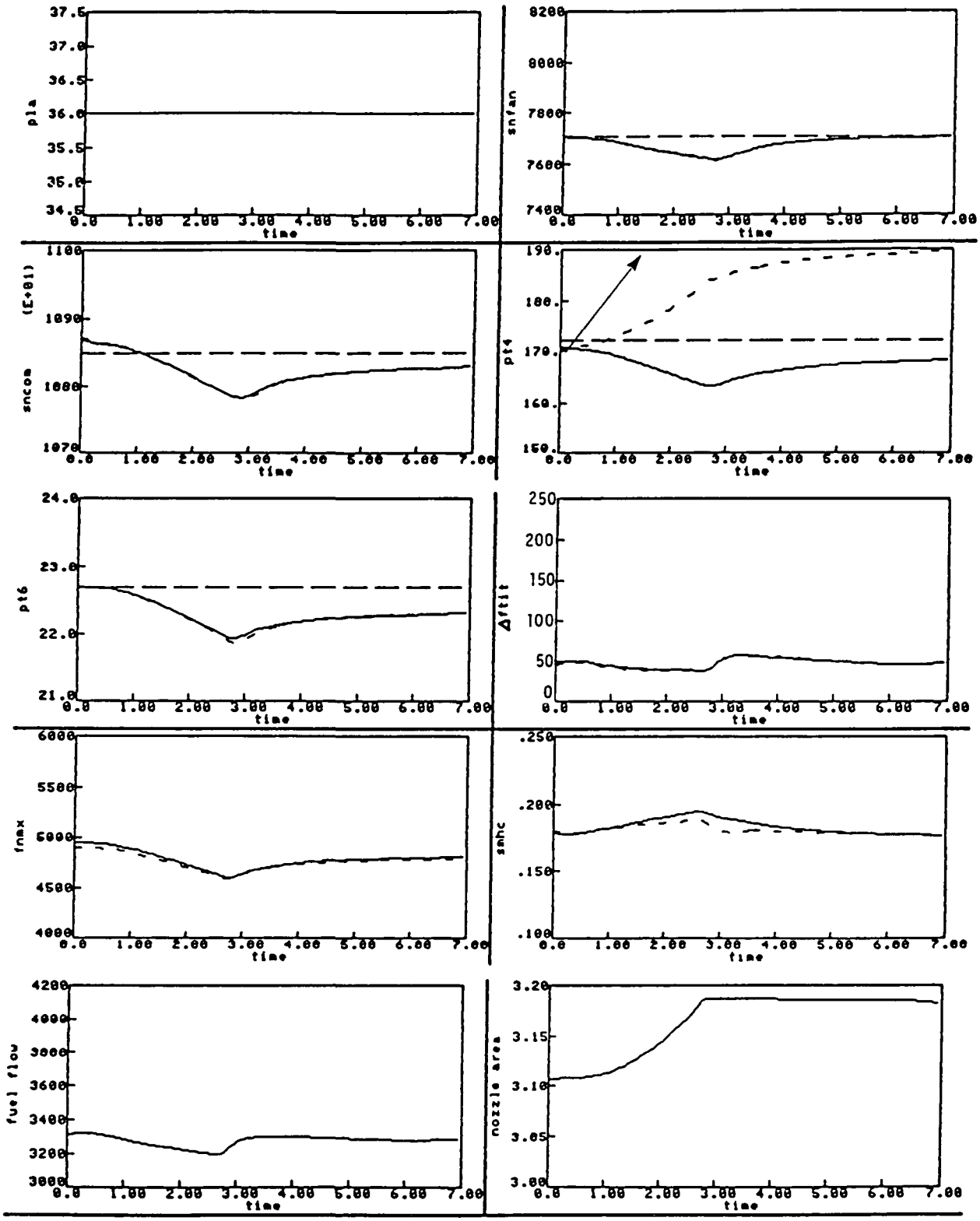

Figure 5-13c Transient Results for Revision 3 with PT4 Failure (+15 psia/second) at the Flight Condition OK/OM, PLA = 36.0 degrees Engine (————), Estimate (— — — —), Reference (——— ———)

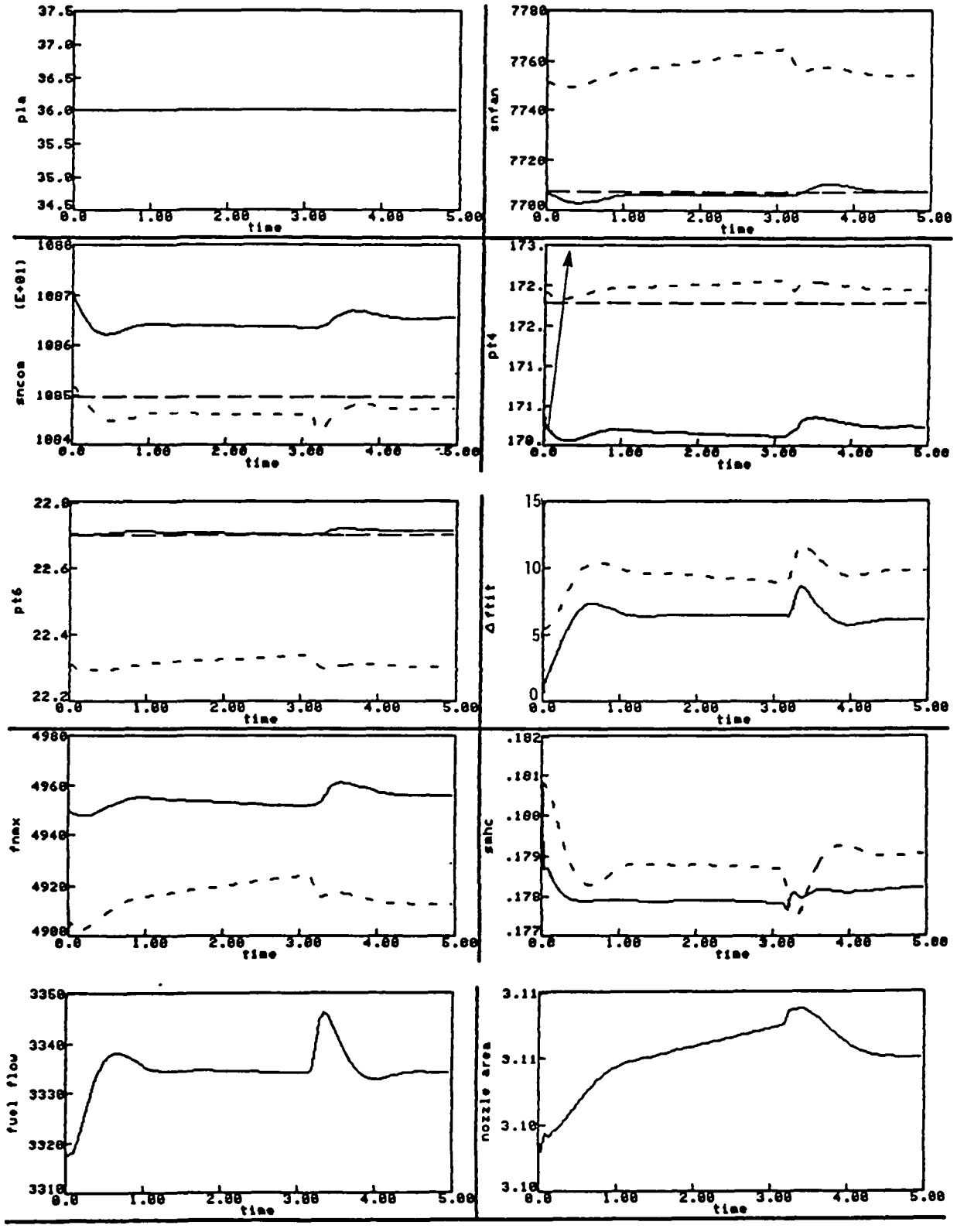

Figure 5-14 Transient Results for Revision 2 with PT4 Failure (+15 psia/second) at the Flight Condition OK/OM, PLA = 36.0 degrees Engine (————), Estimate (— — — —), Reference (——— ———)

increasing the respective gains to make the time constant corresponding to the PT6 integrator shorter. The results are shown for the revision 1 case in Figure 5-15, where N1 and PT6 are shown trimmed to their respective reference points.

For this particular failure case, Revision 2 is clearly the best of the three revisions.

5.2.3.5 PT6 Drift Failure At The Flight Condition 45k/0.9/83

A PT6 drift of +2 PSIA/sec was simulated at the flight condition of 45K/.9/83. The failure was induced at t=0.1 seconds. Figures 5-16a through 5-16c show the engine and estimator output responses for the three revisions. It is noted that PT6 is not initialized at the reference schedule value since nozzle area is saturated to its minimum position. The failure characteristics are as follows.

	Time to Detect	Time to Isolate	False Alarm	Misses
Revision 1	2.524	0.226	none	none
Revision 2	2.490	0.260	none	none
Revision 3	0.486	2.190	none	none

The detection time for Revision 3 is short and the isolation time is long compared to Revisions 1 and 2, for reasons discussed earlier.

The slower integral trim action of Revision 3, compared to Revision 1 and 2, can be seen in the low rotor speed (SNFAN) response. Also, the slow integral trim action on PT6 (in this case increasing nozzle area to reduce PT6 estimate to the Reference schedule) is evident in all three revisions. As with the previous failure case, the failure accommodation transients are minimal for Revision 2.

5.2.3.6 PT4 Drift Failure At The Flight Condition 45k/0.9/83

A PT4 drift failure was simulated at the flight condition 45K/0.9/83, with a drift rate of 20 PSIA/second. The failure was induced at 0.1 seconds. Figures 5-17a through 5-17c demonstrate the engine and the estimator output responses for the three revisions. PT6 is not initialized at the reference schedule value since nozzle area is saturated to its minimum position. The failure performance of the three revisions is as follows.

	Time to Detect	Time to Isolate	False Alarm	Misses
Revision 1	1.996	0.120	none	none
Revision 2	2.028	0.156	none	none
Revision 3	0.496	1.492	none	none

A general comparison of the failure accommodation transients for the three revisions shows Revision 2 to again be the best performer.

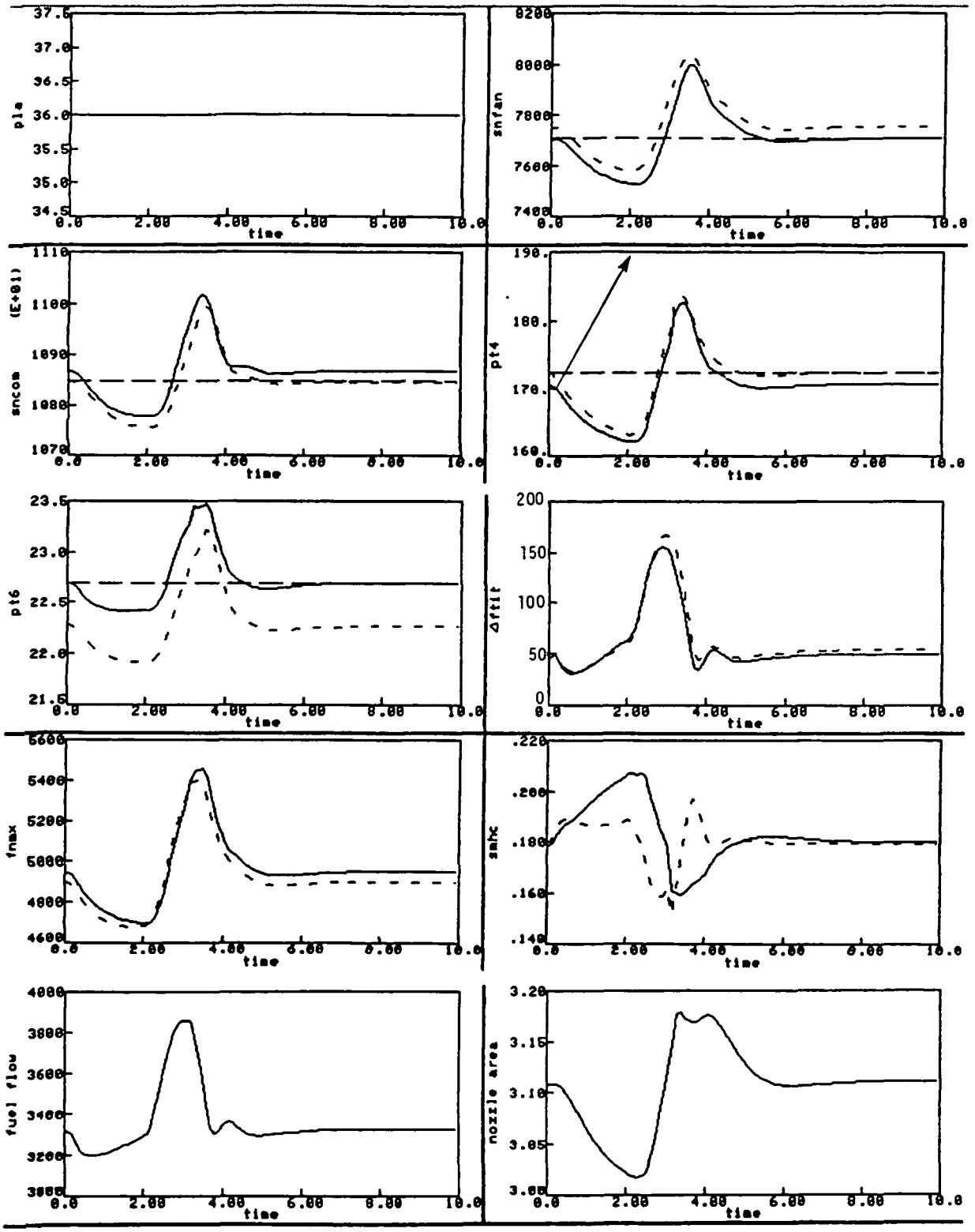

Figure 5-15 Transient Results for Revision 1 with Modified Integral Gains, PT4 Failure (+15 psia/sec) at the Flight Condition OK/OM, PLA = 36.0 degrees. Engine (————), Estimate (— — — —), Reference (——— ———)

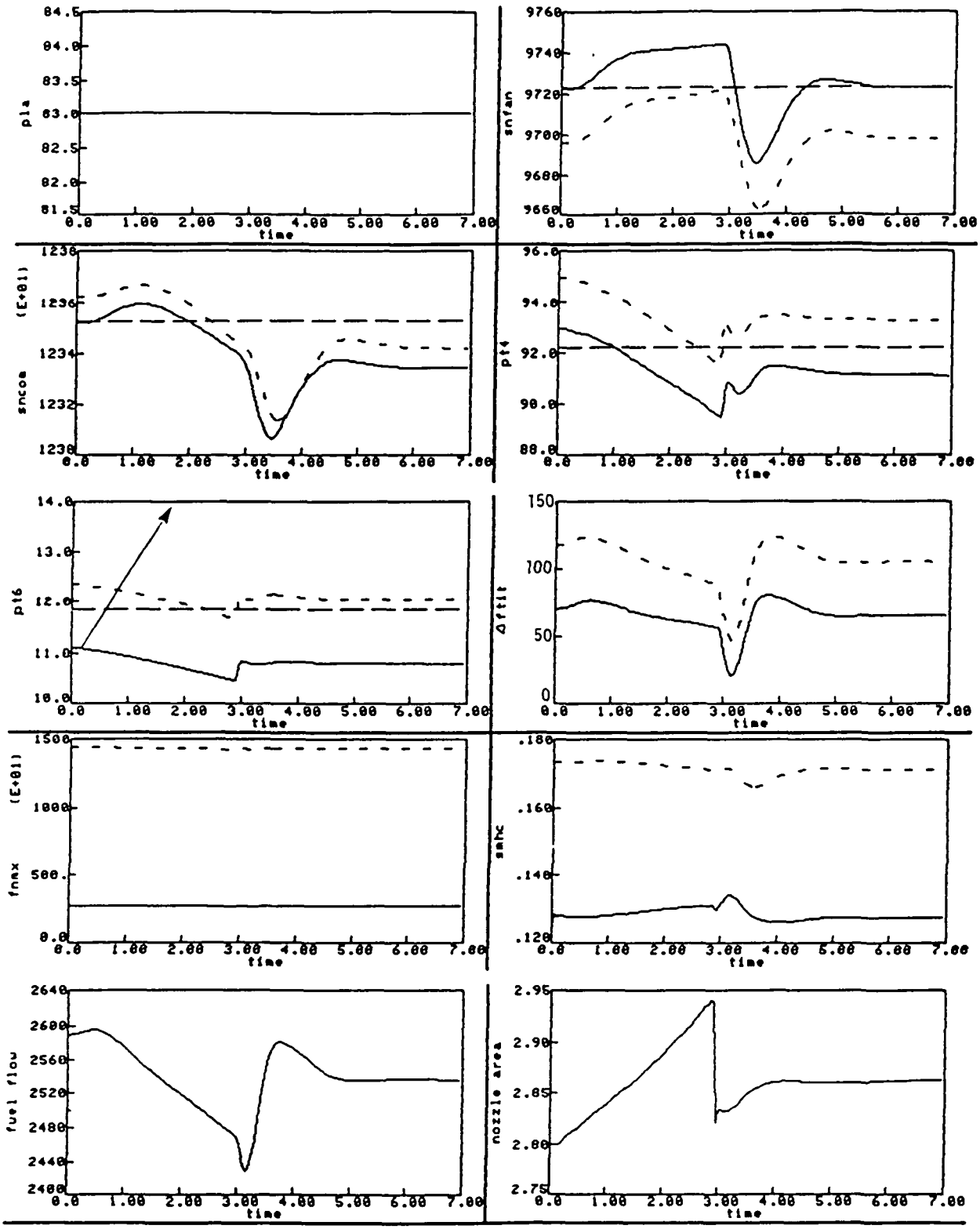

Figure 5-16a Transient Results for Revision 1 with PT6 Failure (+2 psia/second) at the Flight Condition 45K/0.9M, PLA = 36.0 degrees. Engine (————), Estimate (— — — —), Reference (——— ———)

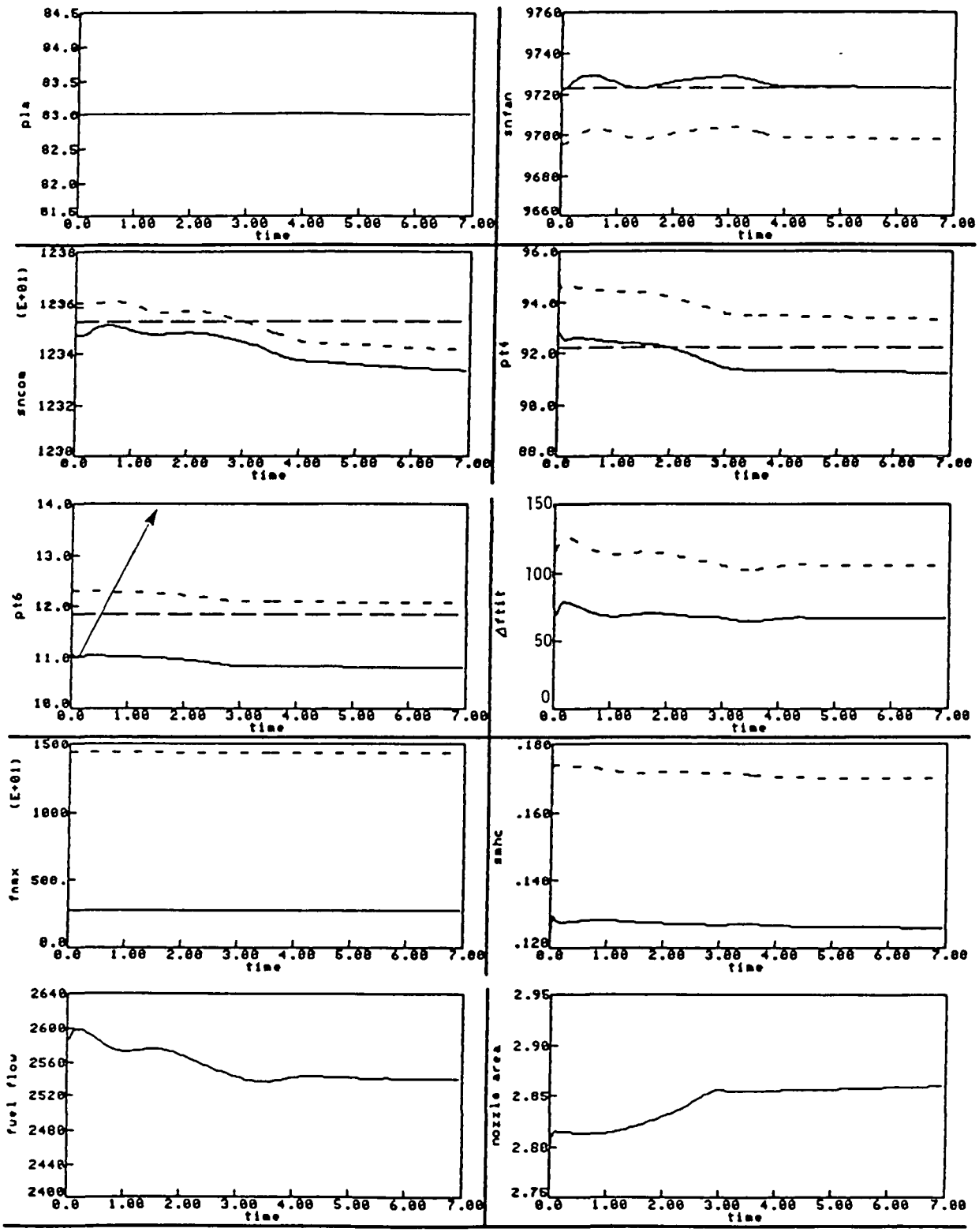

Figure 5-16b Transient Results for Revision 2 with PT6 Failure (+2 psia/second) at the Flight Condition 45K/0.9M, PLA = 36.0 degrees Engine (————), Estimate (— — — —), Reference (——— ———)

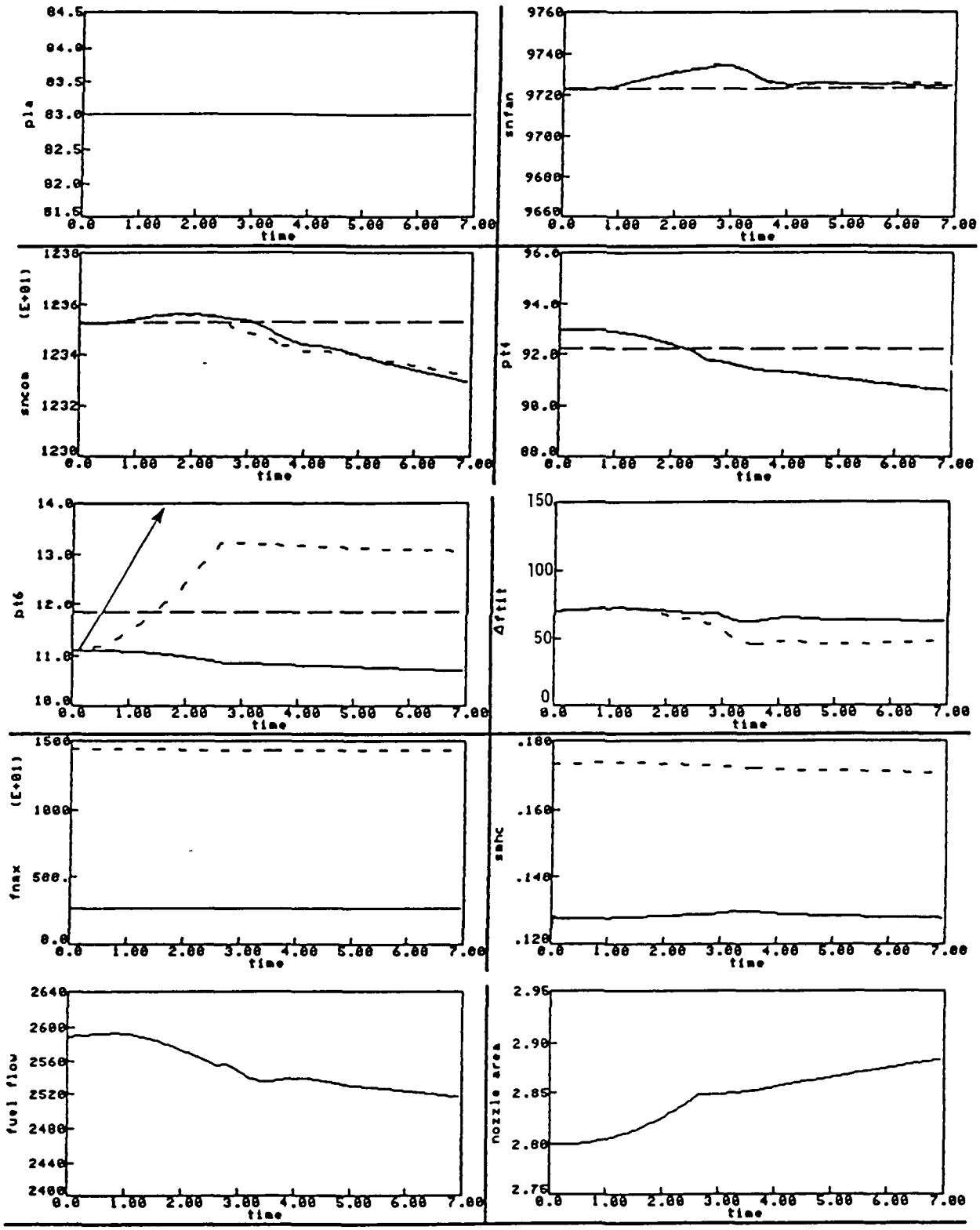

Figure 5-16c Transient Results for Revision 3 with PT6 Failure (+2 psia/second) at the Flight Condition 45K/0.9M, PLA = 36.0 degrees Engine (————), Estimate (— — — —), Reference (——— ———)

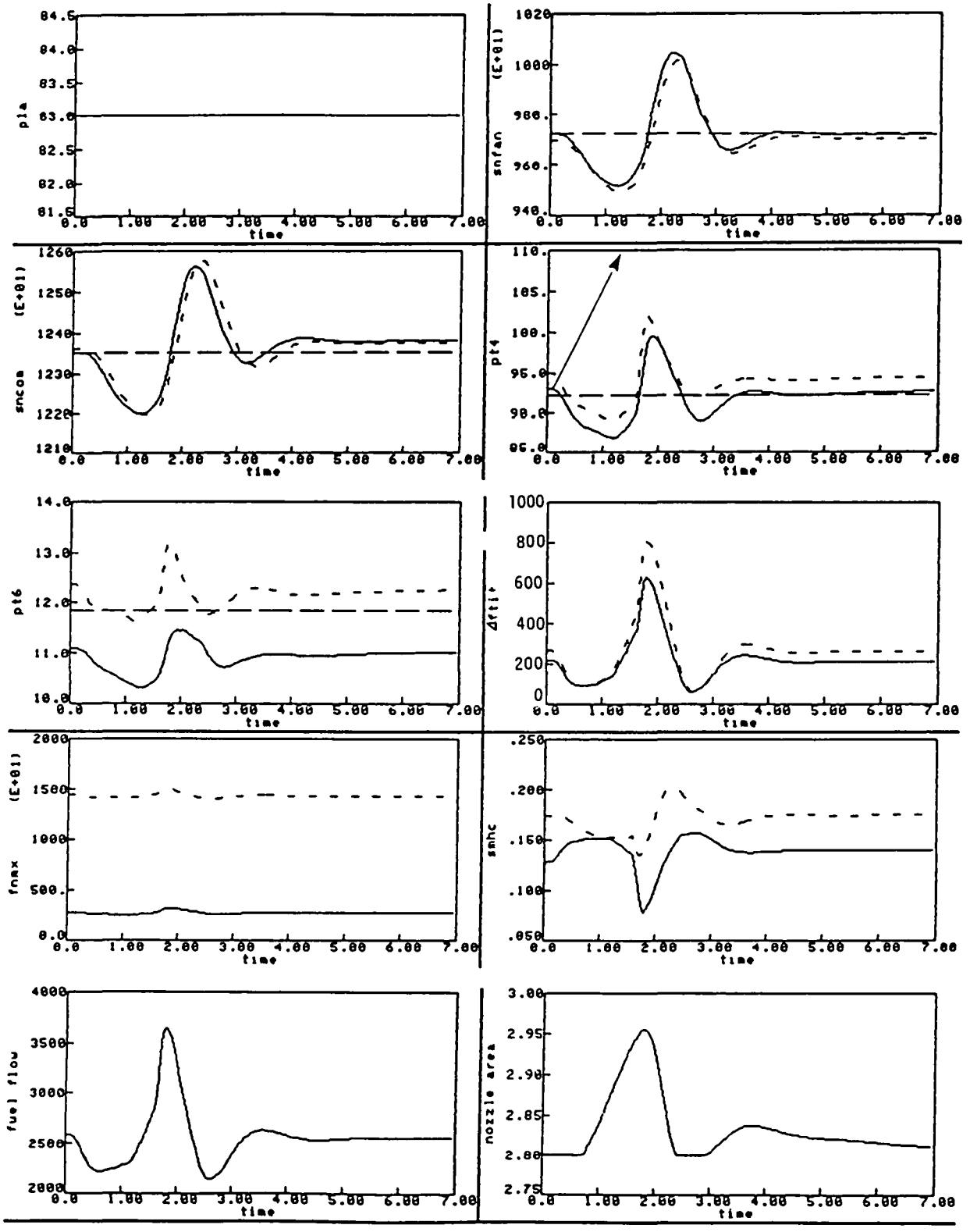

Figure 5-17a Transient Results for Revision 1 with PT4 Failure (+20 psia/second) at the Flight Condition 45K/0.9M, PLA = 83.0 degrees Engine (————), Estimate (— — — —), Reference (—— ——)

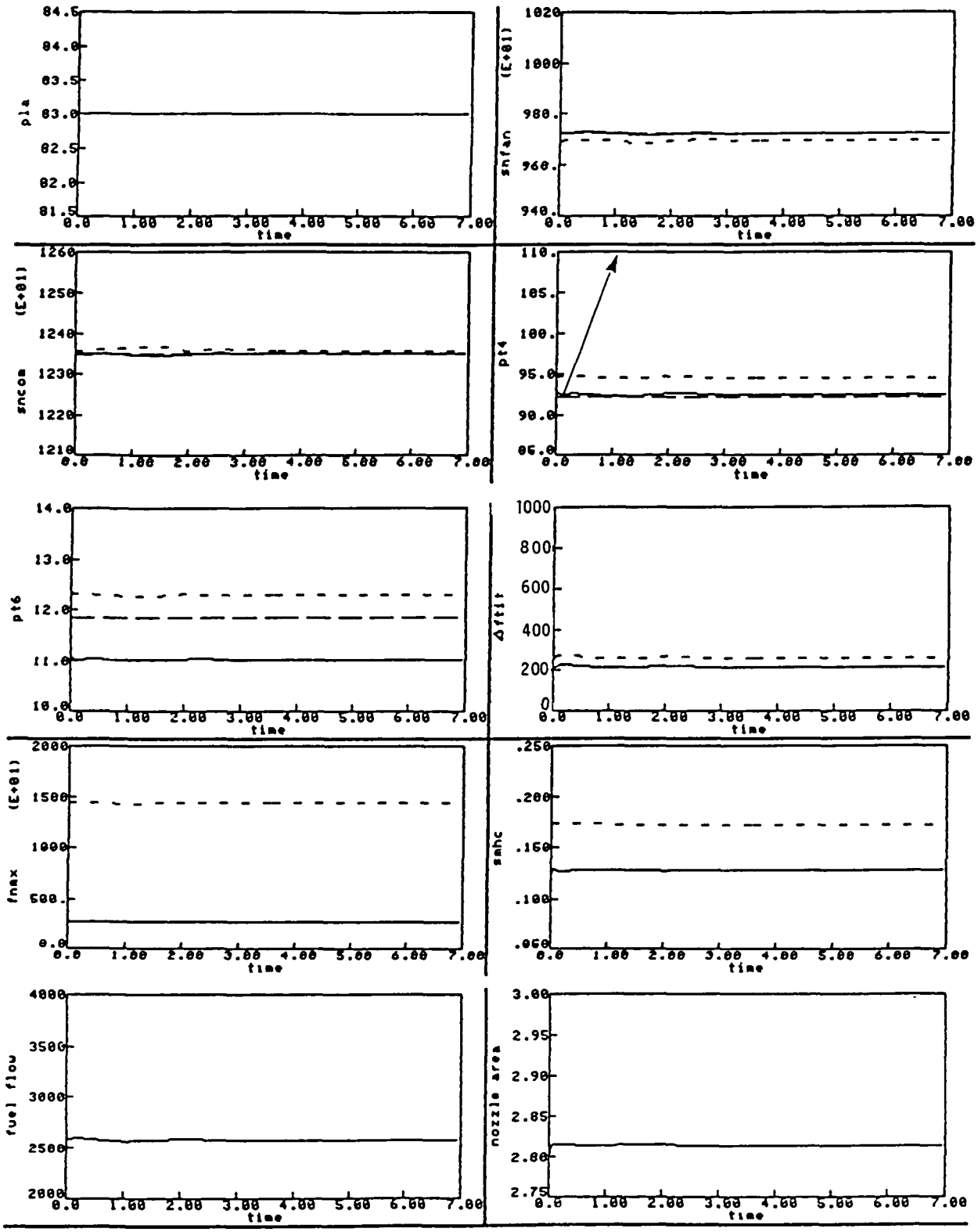

Figure 5-17b Transient Results for Revision 2 with PT4 Failure (+20 psia/second) at the Flight Condition 45K/0.9M, PLA = 83.0 degrees Engine (————), Estimate (— — — —), Reference (——— ———)

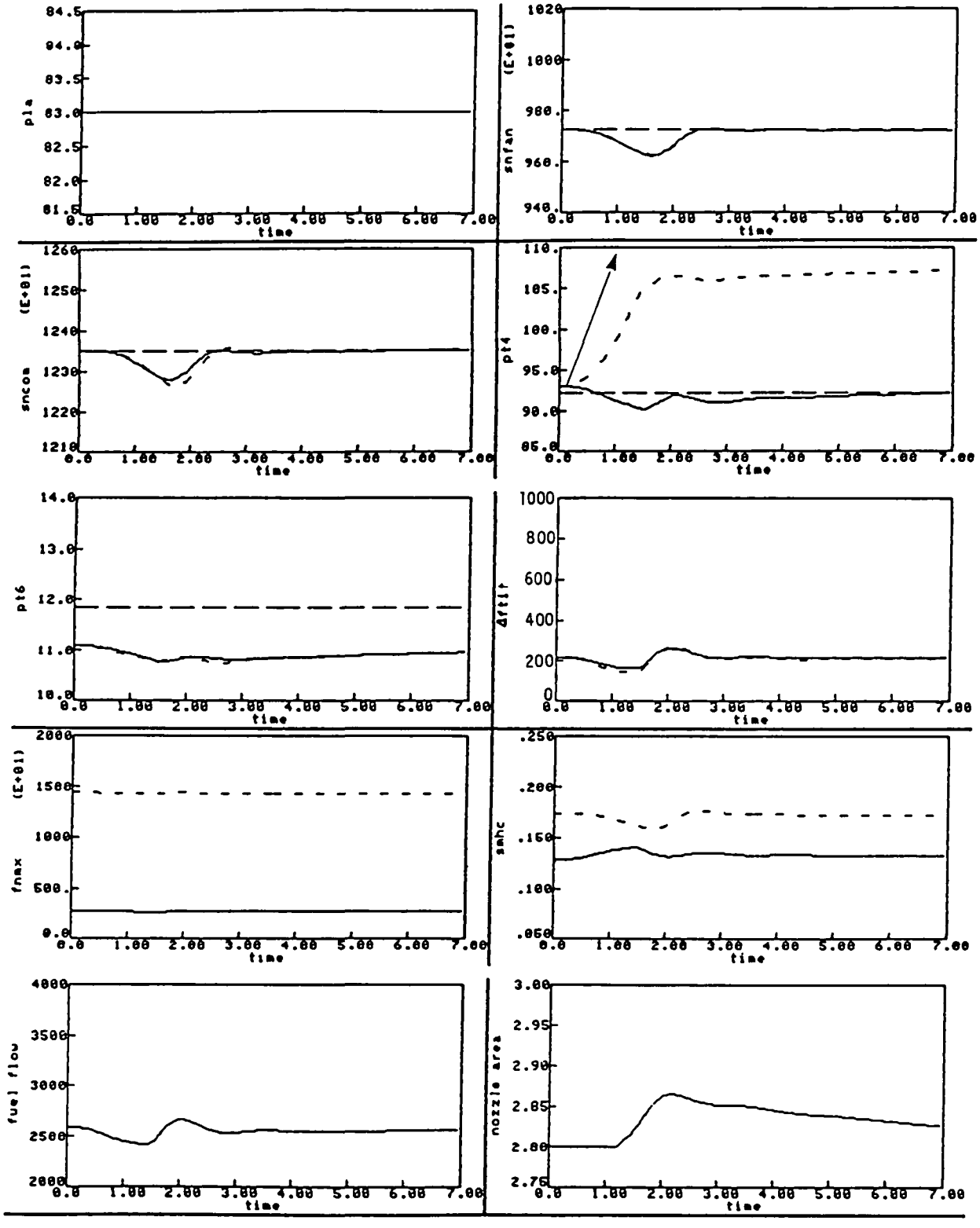

Figure 5-17c Transient Results for Revision 3 with PT4 Failure (+20 psia/second) at the Flight Condition 45K/0.9M, PLA = 83.0 degrees Engine (————), Estimate (— — — —), Reference (——— ———)

5.2.3.7 N2 Drift Failure At The Flight Condition 20K/0.3/83

An N2 drift failure of 2000 RPM/sec was induced at t = 0.1 second. The engine and estimator output responses are demonstrated in Figures 5-18a through 5-18c. The failure detection and isolation times for each revision are as follows.

	Time to Detect	Time to Isolate	False Alarm	Misses
Revision 1	0.672	0.204	none	none
Revision 2	0.748	0.200	none	none
Revision 3	0.172	0.684	none	none

All three revisions demonstrate comparable performance for this failure case.

5.3 EVALUATION SUMMARY

The conclusions summarized here are based on the results of the failure performances presented in the previous section.

(a) All three revisions achieve the primary goal of eliminating the engine steady state hang-off errors in the fan speed, N1, and augmentor pressure, PT6. In the case of no failure, all revisions have the same steady state operating point. The augmentor pressure converges to its reference point at a slow rate determined by the time constant of the integrators in the multivariable control logic.

(b) Revisions 1 and 2 are far less complex than Revision 3. Revisions 1 and 2 require modification in several lines of code whereas Revision 3 requires design of integral gains and supplementing the filter with integral trim logic.

(c) The residuals are integrated to zero in Revision 3 but they are large in Revisions 1 and 2, as they are in the baseline DIA algorithm.

(d) All three revisions detected and isolated the simulated failures. No false alarms were issued and there were no misses.

(e) In the cases of hard failures (see Figures 5-9b through 5-9d and Figures 5-11a through 5-11c), the three revisions have comparable responses. The accommodation transients in all cases are alike. The hangoff in the fan speed (Figures 5-9b through 5-9d) and in compressor speed (Figures 5-11a through 5-11c) after failure isolation is comparable in all cases. In the case of an N2 hard failure, Revision 1 (Figure 5-11a) has more excursions in the inputs and outputs than Revisions 2 and 3.

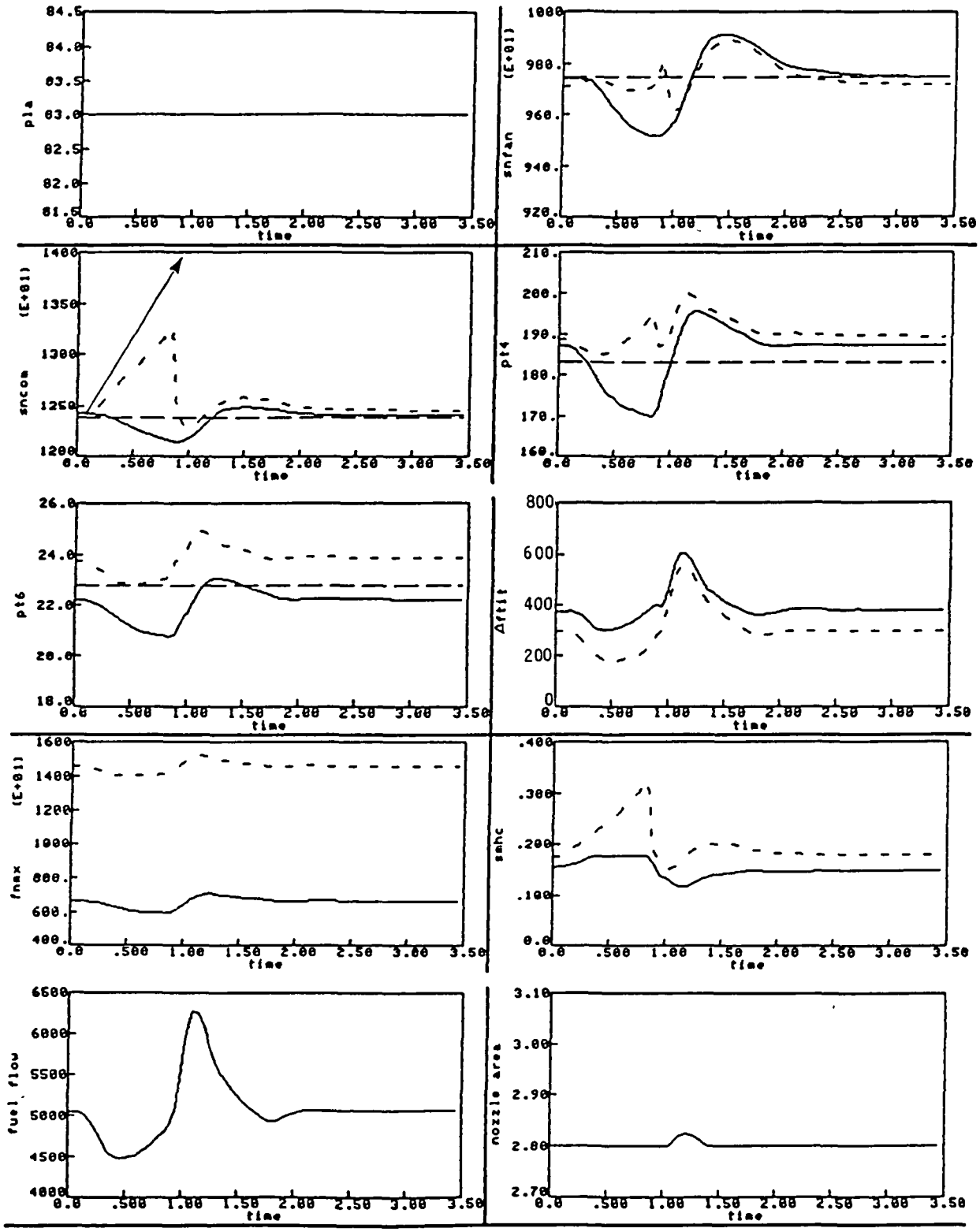

Figure 5-18a Transient Results for Revision 1 with N2 Failure (+2000 rpm/second) at the Flight Condition 20K/0.3M, PLA = 83.0 degrees Engine (————), Estimate (— — — —), Reference (——— ———)

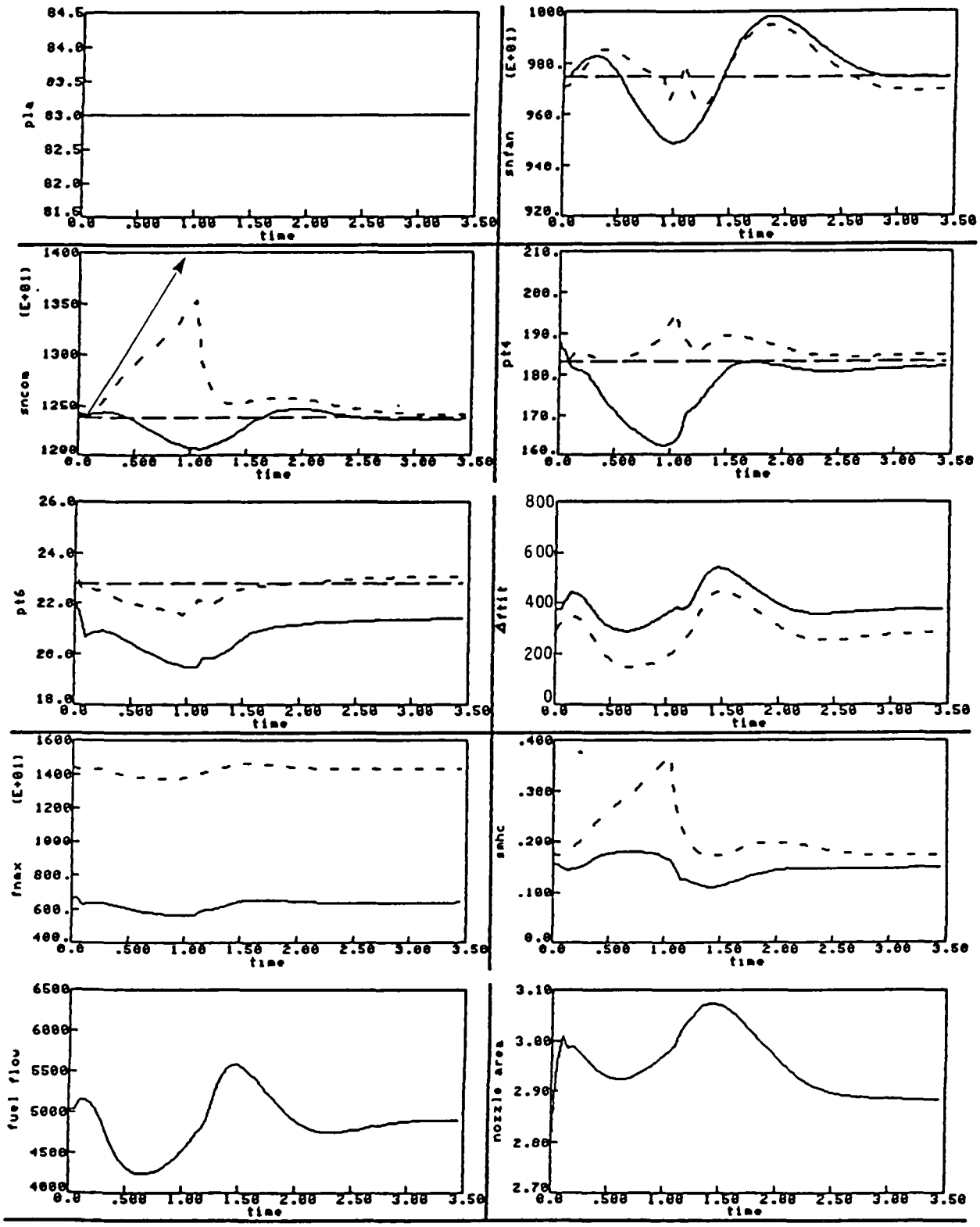

Figure 5-18b Transient Results for Revision 2 with N2 Failure (+2000 rpm/second) at the Flight Condition 20K/0.3M, PLA = 83.0 degrees Engine (————), Estimate (— — — —), Reference (——— ———)

C-2

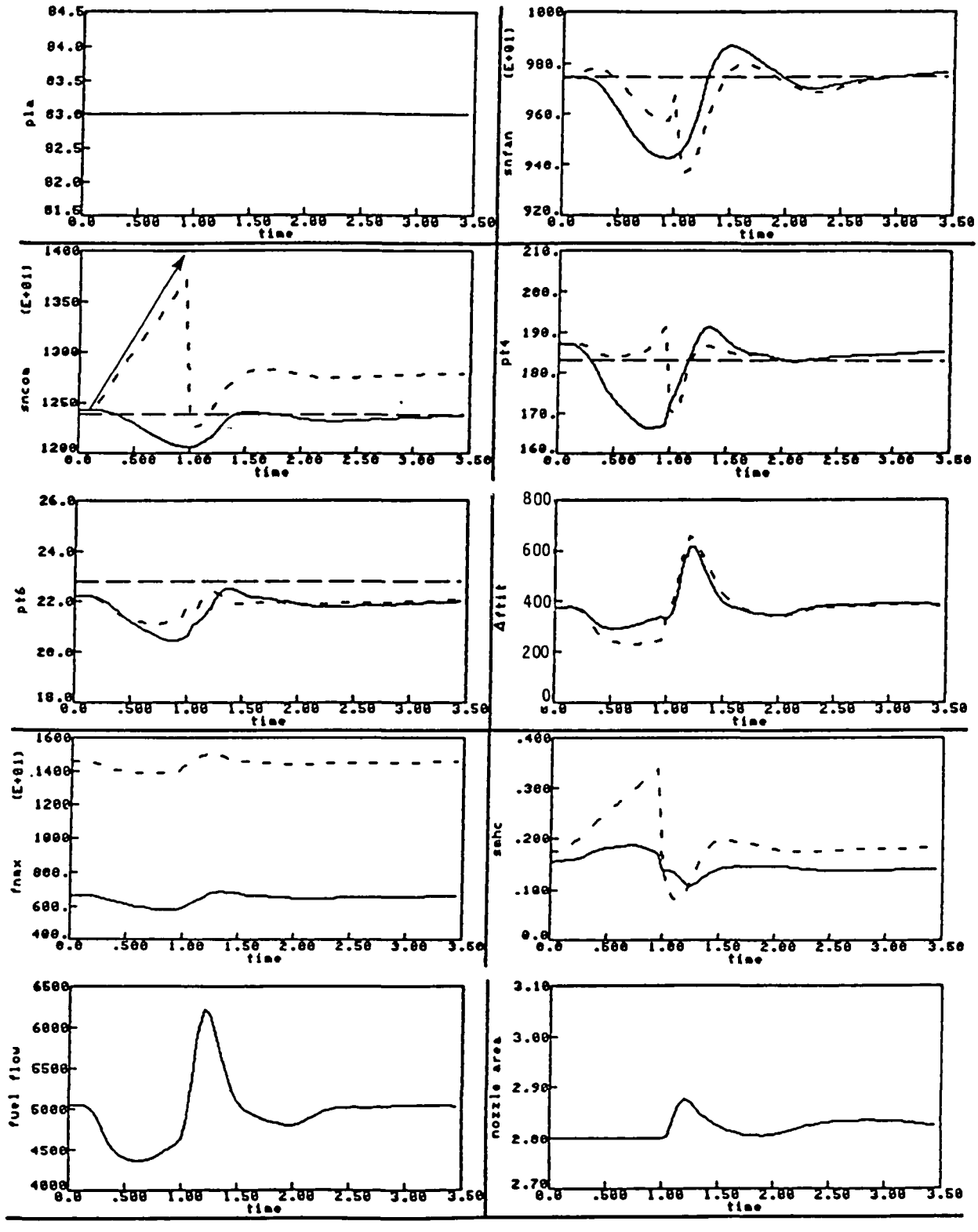

Figure 5-18c Transient Results for Revision 3 with N2 Failure (+2000 rpm/second) at the Flight Condition 20K/0.3M, PLA = 83.0 degrees Engine (————), Estimate (— — — —), Reference (——— ———)

(f) In all the high and low rate drift failures that were simulated, the accommodation transient is visible. This transient is comparable in all three revisions for N1 and N2 high-rate drift failures (see Figures 5-12a through 5-12c and 5-18a through 5-18c, respectively). For the PT4 and PT6 simulated failures (see Figures 5-13, 5-16 and 5-17), the drift in the outputs of Revision 2 is small. This results from the filter gains associated with PT4 and PT6 being small which means that the failure affects the estimates at a very slow rate. The accommodation transient for Revision 2 is also smaller than Revisions 1 and 3.

g) The improved detection capability of Revision 3 (for drift failures) was offset by a potential increased sensitivity to false alarms. This is a result of the isolation filters being the same in all revisions.

h) The additional integrators tied to the filter in Revision 3 introduce more dynamics resulting in the slowing down of the system. This can be observed in Figures 5-13, 5-16 and 5-17.

5.4 DEVELOPMENT OF REVISED FILTER GAIN MATRIX

Polynomial curve fits of the elements of the filter gain matrix K were developed for use with the full envelope simplified nonlinear model of the F100 engine. An error analysis was performed which compares the K matrix obtained from the polynominal schedule with the individual K matrices, designed for the representative flight points.

5.4.1 Filter Gain Design

Filter gains can be designed by using either the linear engine models obtained from the thermodynamic simulation (Section 3.2), or by computing the linear models at given flight points from the polynomial curve fits of the linear model matrices (Section 3.5). The latter method was used in order to be consistent with the actual implementation in which the filter will utilize the simplified nonlinear engine model implemented with the polynomial curve fits. Linear models were computed from the polynomial curve fits at the flight points given in Table 5-3. It was noticed from the linear model data that there are several flight points where the model matrices are the same for all power points. This is shown in Table 5-3 using brackets. The elimination of duplicate models reduces the number of models available for gain design from 109 to 76.

The polynomial curve fits of the F, $F^{-1}G$, H and D matrix elements yields matrices with correction factors applied. The filter gain design can be performed either by using the "corrected" matrices or the "uncorrected" matrices. Figures 5-19 and 5-20 demonstrate the corrected and uncorrected F(1,1) element of the F matrix, respectively, calculated from the polynomial curve fits. The corrected matrix data show reduced scatter compared to the uncorrected set and was used in the design of the filter gain matrices. This

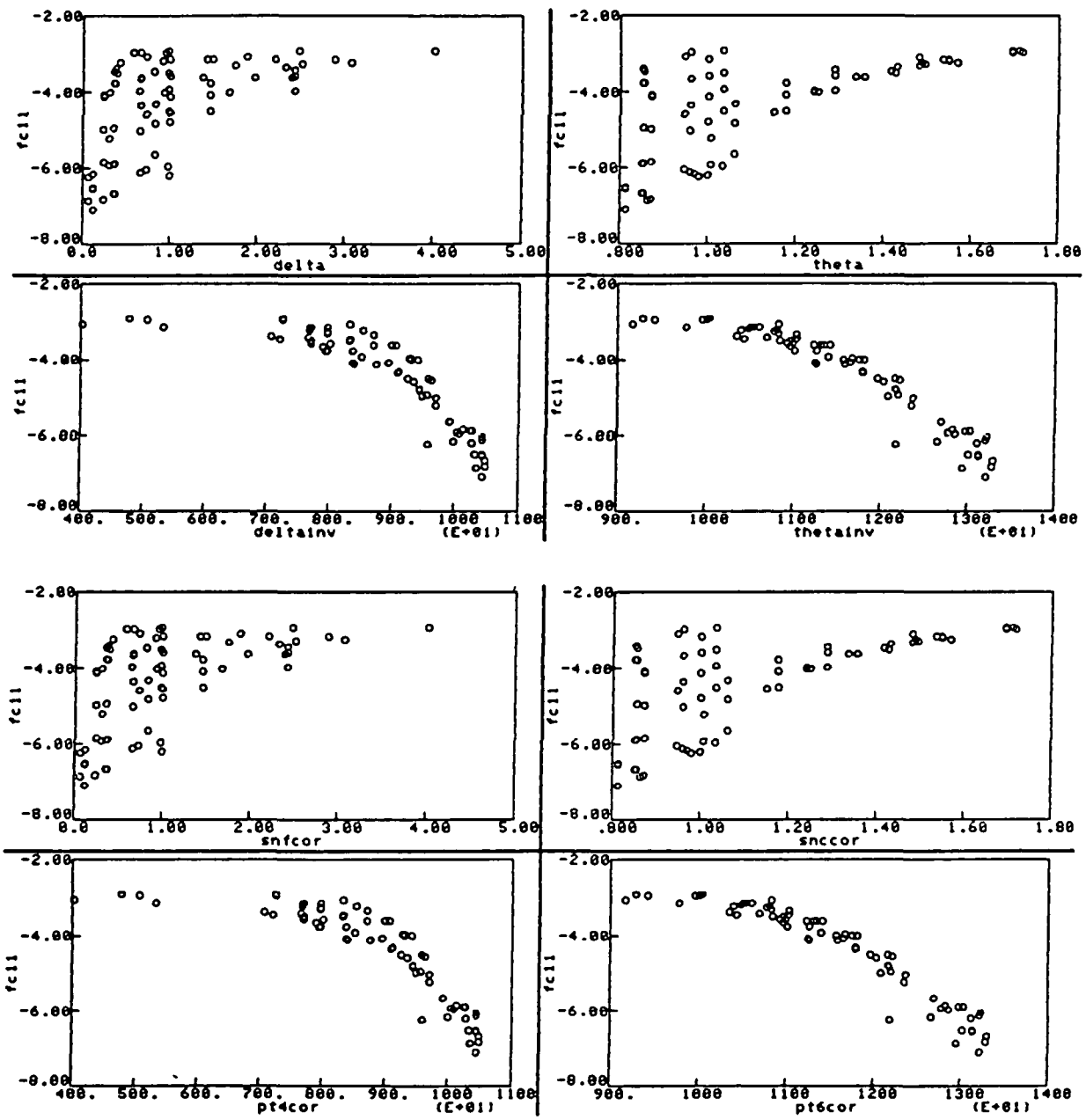

Figure 5-19 Point Plots of the Corrected F(1,1) Element of F Matrix Obtained From the Polynomial Schedule

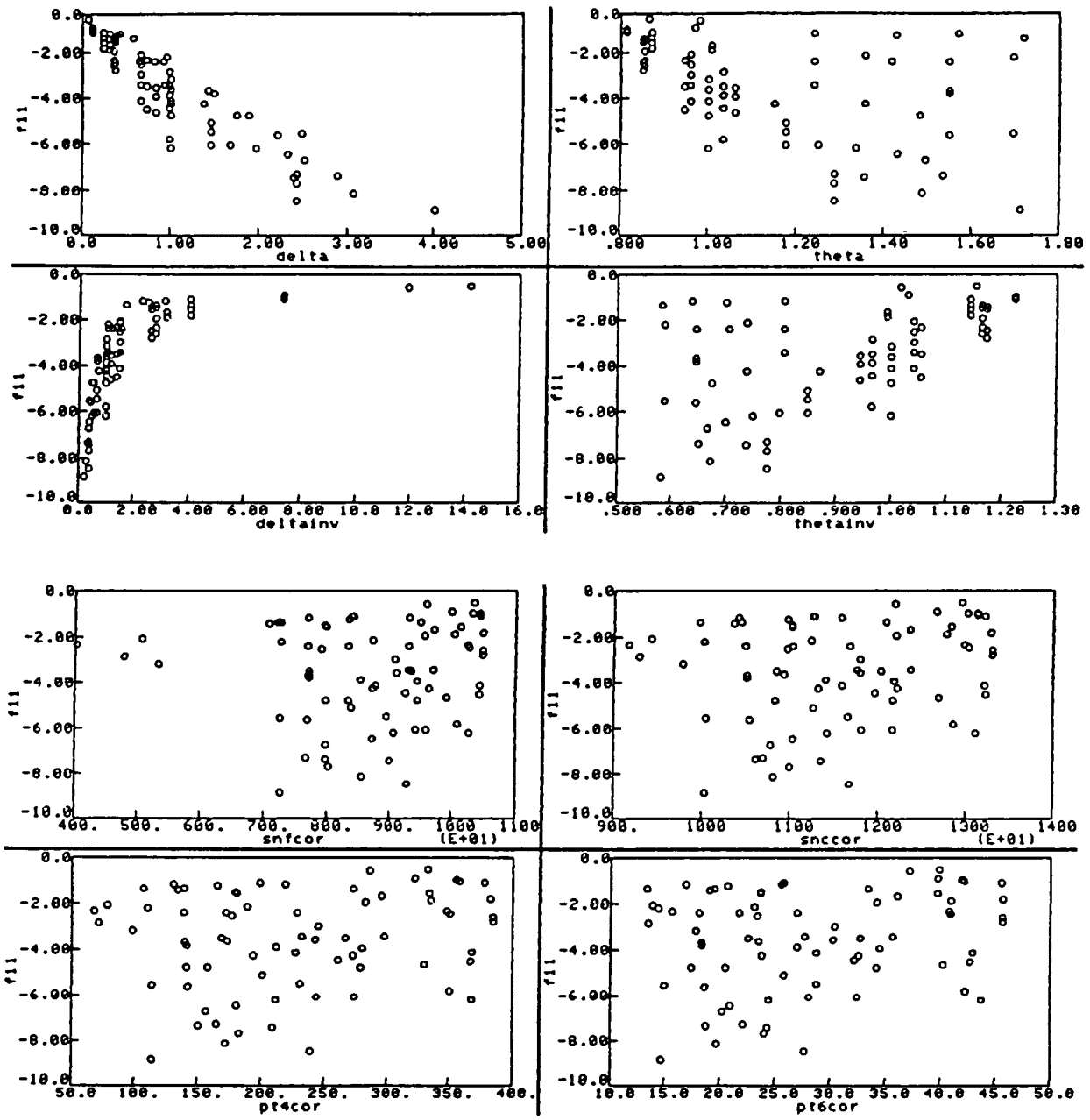

Figure 5-20 Point Plots of the Uncorrected F(1,1) Element of F Matrix Obtained From the Polynomial Schedule

decision was influenced by the idea that the corrected models might have eigenvalues which would have less scatter if plotted against similar corrected bias parameters. This would make it possible to determine the models with eigenvalues which are close to each other and to group such models together. A computer program was written to compute eigenvalues of the corrected and uncorrected matrices. A visual check of the eigenvalues of the corrected and uncorrected set of matrices was made and the above was found to be true. It was observed that there were groups of models for which the eigenvalues were quite similar. Seven such groups of models were identified and are shown in Table 5-4.

There were seven linear models which did not fall in any of the seven groups because their eigenvalues were large compared to the range of eigenvalues of the models in the seven groups. These are model numbers 66, 67, 72, 73, 76, 85 and 96 (Table 5-4). These models were ignored in the filter gain design. However, transient operation of the filter was checked at some of these flight conditions to verify filter stability.

A representative model was chosen in each group to be used for design of the filter gain matrix for that group. These models are shown circled in Table 5-4. The filter gain designed for the representative model was used to check the closed loop eigenvalues of other models in the same group. The open loop eigenvalues are the eigenvalues of F matrix and closed loop are eigenvalues of (F + K H) matrix. These models in each group for which the closed loop eigenvalues were checked are underlined in Table 5-4. Results of the filter gain design and validation for group 2 are shown in Table 5-5.

TABLE 5-3

FLIGHT POINTS FOR LINEAR MODEL DATA

Altitude (Ft)	Mach No.	PLA (Deg.)
0	0	24., 36., 52., 67., 83.
0	1.2	60., 70., 83.
10000	0.3	20., 56., 83.
10000	0.75	20., 36., 52., 67., 83.
15000	1.25	60., [74., 83.]
15000	1.6	74., 83.
20000	0.75	20., 36., 52., 67., 83.
20000	1.5	[74., 83.]
20000	1.9	[74., 83.]
25000	1.75	[74., 83.]
28000	1.25	60., 74., 83.
30000	0.6	24., 36., 67., 83.
30000	2.0	[74., 83.]
32000	2.2	[74., 83.]
35000	0.8	20., 36., 52., 67., 83.
35000	1.6	[74., 83.]
35000	2.2	[74., 83.]
35000	2.5	[74., 83.]
41000	2.2	74., 83.
41000	2.3	[74., 83.]
42500	1.8	[74., 83.]
42500	2.2	[74., 83.]
45000	0.9	24., 40., 52., 67., 83.
45000	2.5	[74., 83.]
49000	2.3	[74., 83.]
50000	1.3	[74., 83.]
50000	1.8	[74., 83.]
50000	2.3	[74., 83.]
52500	0.65	20., 36., 52., 67., 83.
55000	2.1	[74., 83.]
56000	2.0	[74., 83.]
59000	2.3	[74., 83.]
65000	1.2	60., [74., 83.]
65000	1.8	[74., 83.]
65000	2.5	74., 83.
70000	0.85	[20., 36., 52., 67., 83.]
70000	2.1	[74., 83.]
75000	1.2	[60., 74., 83.]
75000	2.3	74., 83.
75000	2.5	[74., 83.]

Table 5-4

Grouping of Linear Models With Similar Eigensystem

Group	Model Numbers*
1	1, 2, 3, 6, 7, 8, 12
2	29, 31, 40, 42, 51, 53, 55, 56, 57, 61, 68, 70, 76, 83, 87, 94
3	9, 13, 14, 17, 18, 20, 22, 27, 60
4	4, 10, 15, 19, 24, 25, 33, 34, 36, 37, 44, 45, 46, 49, 50, 101, 106, 108
5	5, 11, 16, 26, 35, 92
6	38, 39, 47, 48, 63, 64, 65
7	78, 79, 80, 81, 82, 89

* Model numbers correspond to the linear models in Table 5-3. For example, Model no. 1 is the linear model at 0 feet altitude, 0 Mach number, and 24 degrees PLA.

TABLE 5-5

Design and Validation Results of the Gain Matrix for Model No. 29 (Group 2)

Model No.	Open loop Eigenvalues	Gain Matrix					Closed loop Eigenvalues
29	-2.46+j0.53	-7.0318	1.2727	-3.8909	-0.6267	0.5500	-10.14
(design)	-2.46-j0.53	0.2545	-6.1115	-0.4551	0.0234	0.0127	- 8.05
point)	-1.17	0.0012	-0.0190	-0.0012	0.0001	0.0000	- 1.17
	-0.41	-0.0165	-0.0489	-0.0142	-0.0015	0.0016	- 0.40
42	-2.39	-7.0318	1.2727	-3.8909	-0.6267	0.5500	-10.15
	-2.20	0.2545	-6.1115	-0.4551	0.0234	0.0127	- 7.70
	-1.23	0.0012	-0.0190	-0.0012	0.0001	0.0000	- 1.24
	-0.44	-0.0165	-0.0489	-0.0142	-0.0015	0.0016	- 0.43
56	-2.79+jo.39	-7.0318	1.2727	-3.8909	-0.6267	0.5500	-10.61
	-2.79-jo.39	0.2545	-6.1115	-0.4551	0.0234	0.0127	- 8.18
	-1.82	0.0012	-0.0190	-0.0012	0.0001	0.0000	- 1.83
	-0.59	-0.0165	-0.0489	-0.0142	-0.0015	0.0016	- 0.62
94	-2.68+jo.35	-7.0318	1.2727	-3.8909	-0.6267	0.5500	- 9.96
	-2.68-jo.35	0.2545	-6.1115	-0.4551	0.0234	0.0127	- 7.27
	-1.12+jo.04	0.0012	-0.0190	-0.0012	0.0001	0.0000	- 2.09
	-1.12-jo.04	-0.0165	-0.0489	-0.0142	-0.0015	0.0016	- 0.91

5.4.1.1 Sensitivity Analysis

A sensitivity analysis of the eigenvalues of the closed loop system to the filter gain matrix elements was conducted using an SCT in-house computer program. The seven gain matrices designed for each group (Table 5-4) were used for this analysis. The elements of the gain matrix which show negligible effect on eigenvalues are: K33, K43, K34, K44, K35 and K45. They also show negligible change in the dc gains. These elements were set to zero in the K matrices for all the groups and the closed loop eigenvalues were checked. They showed no significant change as shown in Tables 5-6a and 5-6b for model 1 (group 1) and model 39 (group 6), respectively.

TABLE 5-6a

EIGENVALUE SENSITIVITY TO GAIN MATRIX ELEMENTS FOR MODEL 1
(Group 1)

Gain Matrix					Closed loop Eigenvalues
-5.3550	-2.9653	-2.7026	-0.5184	0.3321	-8.5011
-0.8896	-3.4383	-1.1883	-0.0858	0.1634	-4.9807
-0.0269	-0.0417	-0.0203	-0.0026	0.0028	-1.9299
-0.0073	-0.0204	-0.0078	-0.0007	0.0012	-0.6985
-5.3550	-2.9653	-2.7026	-0.5184	0.3321	-8.5011
-0.8896	-3.4383	-1.1883	-0.0858	0.1634	-4.9820
-0.0269	-0.0417	0.0000	0.0000	0.0000	-1.9299
-0.0073	-0.0204	0.0000	0.0000	0.0000	-0.6965

TABLE 5-6b

EIGENVALUE SENSITIVITY TO GAIN MATRIX ELEMENTS FOR MODEL 39
(Group 6)

Gain Matrix					Closed loop Eigenvalues
-17.0563	-4.4392	-1.5790	-0.9692	-1.2022	-25.3128
-7.7686	-17.7455	-8.6375	-0.4601	4.2235	-20.8330
-0.0335	0.0121	0.0082	-0.0013	-0.0062	-4.7546
0.0097	0.0454	0.0236	0.0015	-0.0093	-1.5875
-17.0563	-4.4392	-1.5790	-0.9692	-1.2022	-25.3117
-7.7686	-17.7455	-8.6375	-0.4601	4.2235	-20.8344
-0.0335	0.0121	0.0000	0.0000	0.0000	-4.7535
-0.0097	0.0454	0.0000	0.0000	0.0000	-1.5894

5.4.2 Curve Fitting of the Gain Matrices

A regression analysis program was used to generate polynomial curve fits of the gain matrix elements. The seven filter gain matrices designed for each of the seven groups were used to generate polynomial models. Curve fits were not generated for the elements of the gain matrix which were found to have negligible effect on the eigensystem and the dc gains of the closed loop system. These elements were set equal to the mean value of the corresponding elements in the seven gain matrices. Table 5-7 shows the resulting polynomial fit.

TABLE 5-7
SCHEDULE OF NORMALIZED K MATRIX

```
K(1,1)=0 1199E+2*D1ORT1-0 2347*XPT6-0.2577E+1*DL1**2-9.309
K(2,1)=-0 7734*RT1OD1-0 3869E+1*TH1I**2+2.513
K(3,1)=-0 1406E-1
K(4,1)= 0 1676E-1*DL1I-0.1379E-2*DL1I**2-0 2418E-1
K(1,2)=  4919E+1*TH1+ 1198E-1*D1ORT1-8 672
K(2,2)=- 4401E+1*DL1I- 2263E-1*XPT4+.4183*DL1I**2+ 8881E-1
K(3,2)=  7774E-2*RT1OD1- 4108E+3/XN1+ 2716E-1
K(4,2)=  1729E-1*RT1OD1- 1159E+1/XPT6+ 1061E-1
K(1,3)=-2 617
K(2,3)=- 8336*RT1OD1- 17*XPT6+2 810
K(3,3)=- 1587E-2
K(4,3)=  2585E-2
K(1,4)=- 9646
K(2,4)=- 2344*DL1I- 1419E-1*XPT6+ 2697E-1*DL1I**2+ 3979
K(3,4)=- 1440E-2
K(4,4)=  2246E-3
K(1,5)=- 2596E+1*TH1+ 1009E-2*XN1-.2499E-1*XPT4+ 4191
K(2,5)=- 1364*DL1I**2+ 1397E+1*DL1I*TH1I-.1699
K(3,5)=-.1031E-2
K(4,5)=- 2983E-2
```

5.4.3 Error Analysis

The error analysis of the fit of the elements of K matrix includes plotting the computed values from the schedule against the actual value of each element. Representative plots are shown in Figures 5-21a through 5-21d for the K11, K21, K12, K22 matrix elements with a 45 degree line and 1 and 2 bands (see section 3.5). Table 5-8 presents a tabulation of the statistical quantities R^2, R, σ_y, and $\sigma_{y/x}$.

5.4.4 Validation Transients For The Combined Filter/Model

To evaluate the effectiveness of the filter gains in estimating sensor outputs, several transient runs were made with the model/filter out of the control loop (running "piggyback") and the filter gains are zero. The model responses were compared to the nonlinear engine simulation and with the model responses when the filter gains are not zero. Figures 5-22 through 5-24 show the model responses at three different flight conditions, where the model is running "piggyback" and the filter gains are zero. Figures 5-25 to 5-27 show the transients, where the model is running "piggyback" but the filter gains are not zero. The flight conditions for Figures 5-25 to 5-27 are the same as Figures 5-22 to 5-24, respectively. Although the model tracks the simulation closely with the gain set equal to zero, it can be seen that the errors are further reduced with the non-zero gains.

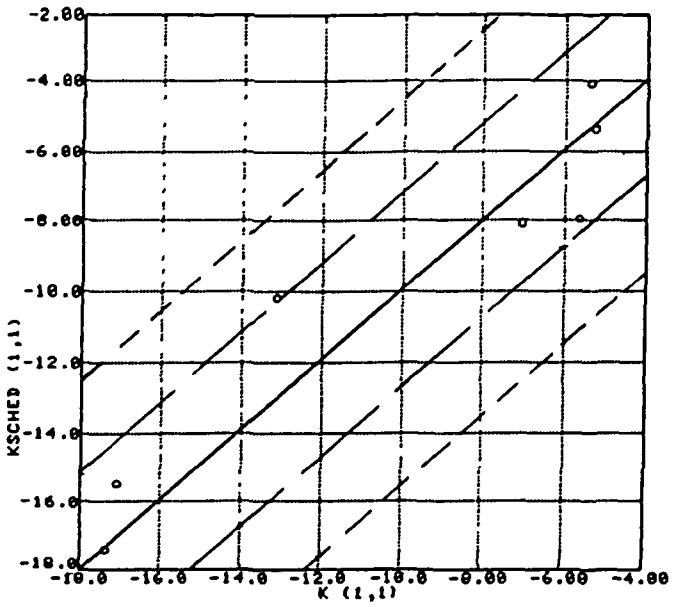

Figure 5-21a Error Analysis of K_{11} Element

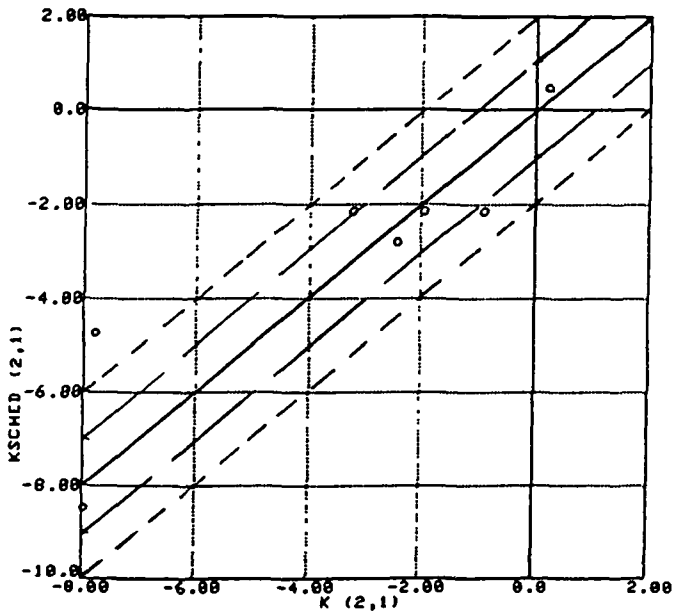

Figure 5-21b Error Analysis of K_{21} Element

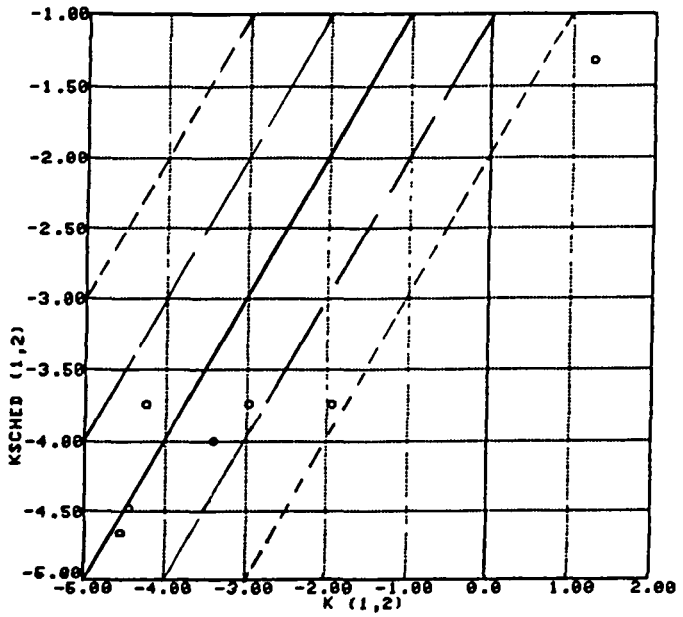

Figure 5-21c Error Analysis of K_{12} Element

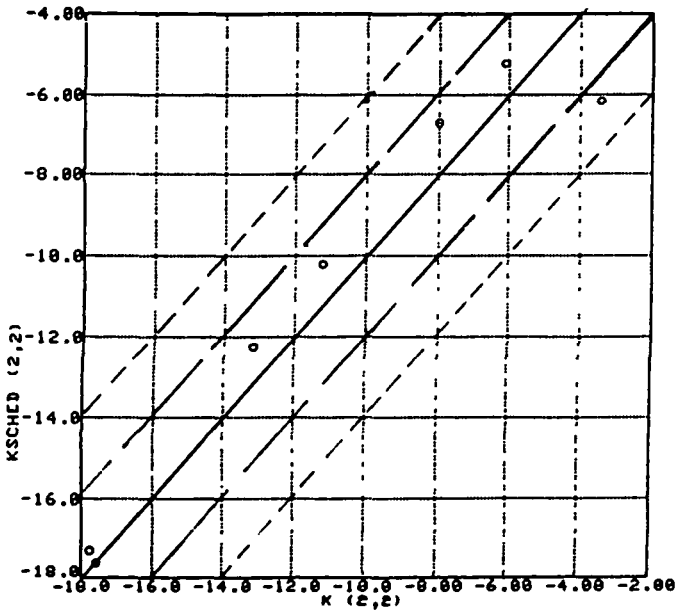

Figure 5-21d Error Analysis of K_{22} Element

TABLE 5-8

ERROR ANALYSIS OF K MATRIX ELEMENTS

Matrix Element	R^2	R	Mean	σy	$\sigma y/x$	$\frac{\sigma y/x}{\sigma y}$
K11	0.704	0.839	- 9.251	4.865	2.794	0.574
K21	0.8313	0.912	- 2.468	2.935	0.919	0.313
K31	0	0	- 0.141E-1	0.147E-1	0.148E-1	1.009
K41	0.8072	0.898	- 0.169E-2	0.162E-1	0.711E-2	0.439
K12	0.8122	0.901	- 1.839	2.261	0.979	0.433
K22	0.8156	0.903	-10.41	4.874	2.093	0.429
K32	0.855	0.925	- 0.779E-2	0.251E-1	0.956E-2	0.381
K42	0.874	0.935	- 0.223E-2	0.458E-1	0.163E-1	0.355
K13	0	0	- 2.617	1.36	1.373	1.009
K23	0.824	0.905	- 3.596	3.14	1.317	0.419
K33	0	0	- 0.159E-2	0.111E-1	112E-1	1.009
K43	0	0	0.259E-2	0.186E-1	0.188E-1	1.009
K14	0	0	- 0.965	0.659	0.665	1.009
K24	0.801	0.895	- 0.347	0.239	0.107	0.466
K34	0	0	- 0.144E-2	0.191E-2	0.193E-2	1.009
K44	0	0	- 0.225E-3	0.159E-2	0.161E-2	1.009
K15	0.712	0.844	0.484	0.849	0.481	0.567
K25	0.725	0.852	1.689	1.839	1.018	0.554
K35	0	0	- 0.1031E-2	0.486E-2	0.491E-2	1.009
K45	0	0	- 0.298E-2	0.839E-2	0.847E-2	1.009

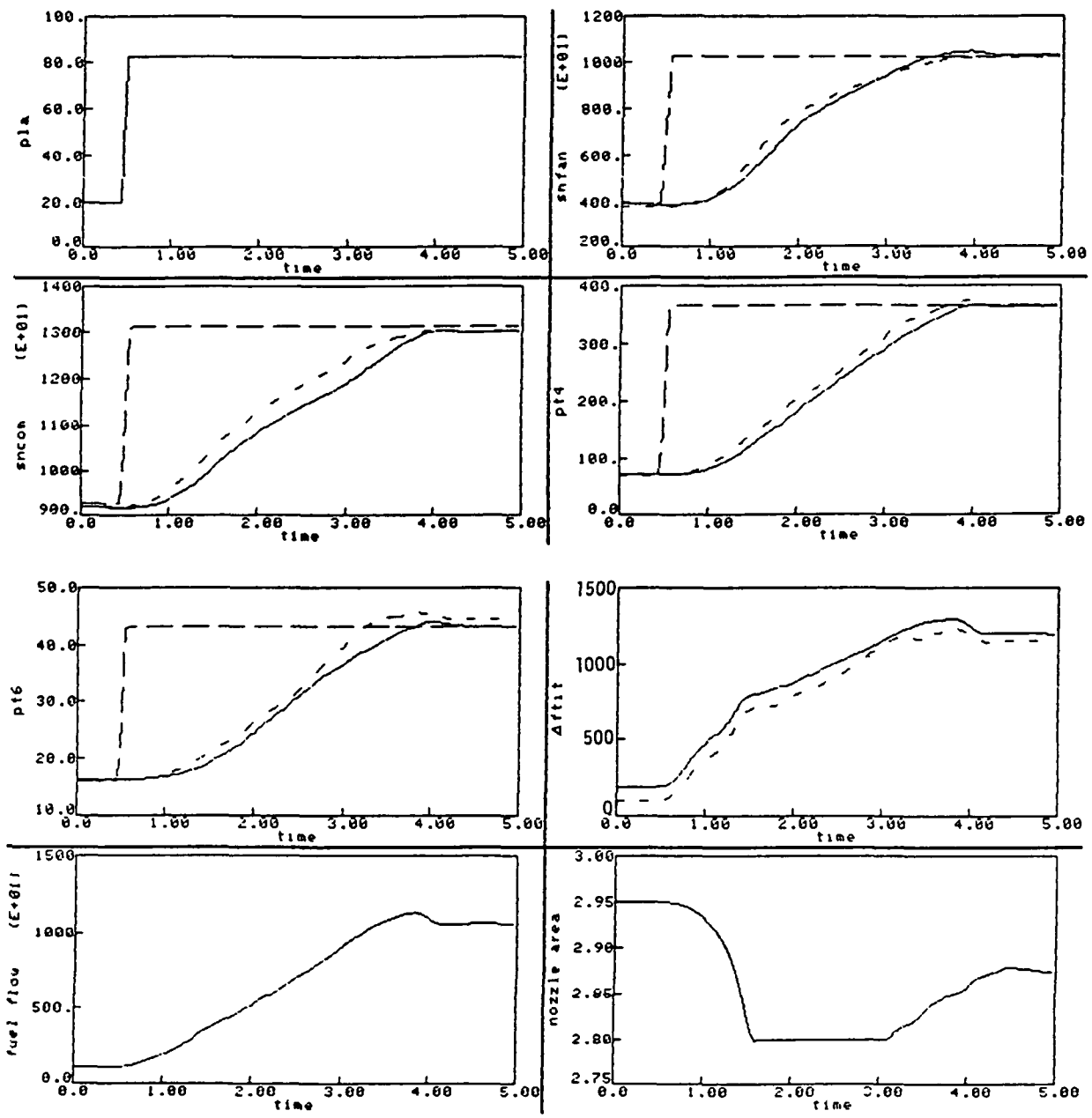

Figure 5-22 Transient Responses of the New Model Running "Piggyback" With Zero Filter Gains, for PLA Step from 20.0 Degrees to 83.0 Degrees at Altitude = 0 ft and Mach No. = 0. Engine (————), Model Output (— — — —), Reference (——— ———)

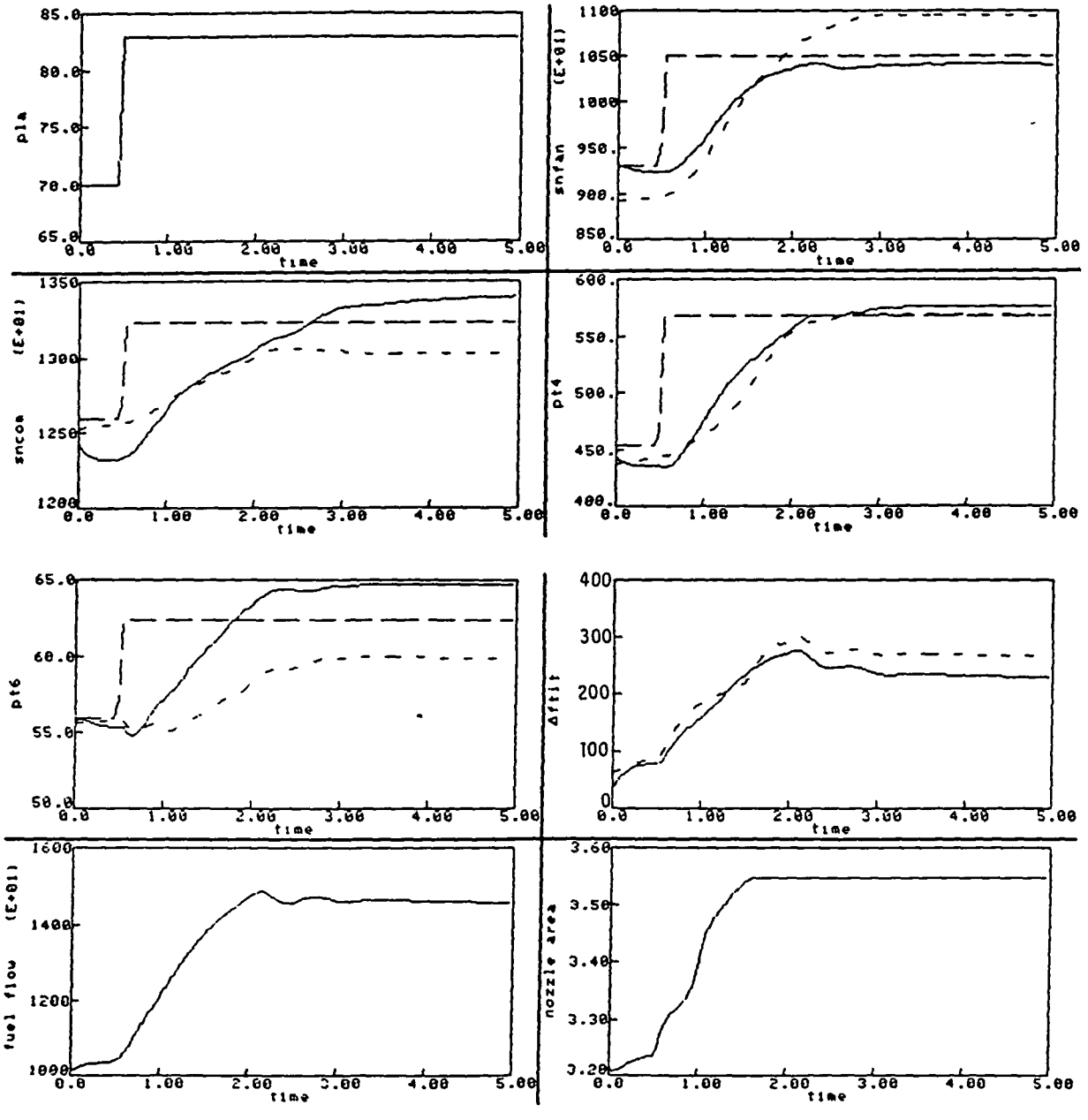

Figure 5-23 Transient Responses of the New Model Running "Piggyback" With Zero Filter Gains, for PLA Step from 70.0 Degrees to 83.0 Degrees at Altitude = 0 ft and Mach No. = 1.2. Engine (————), Model Output (— — — —), Reference (———— ————)

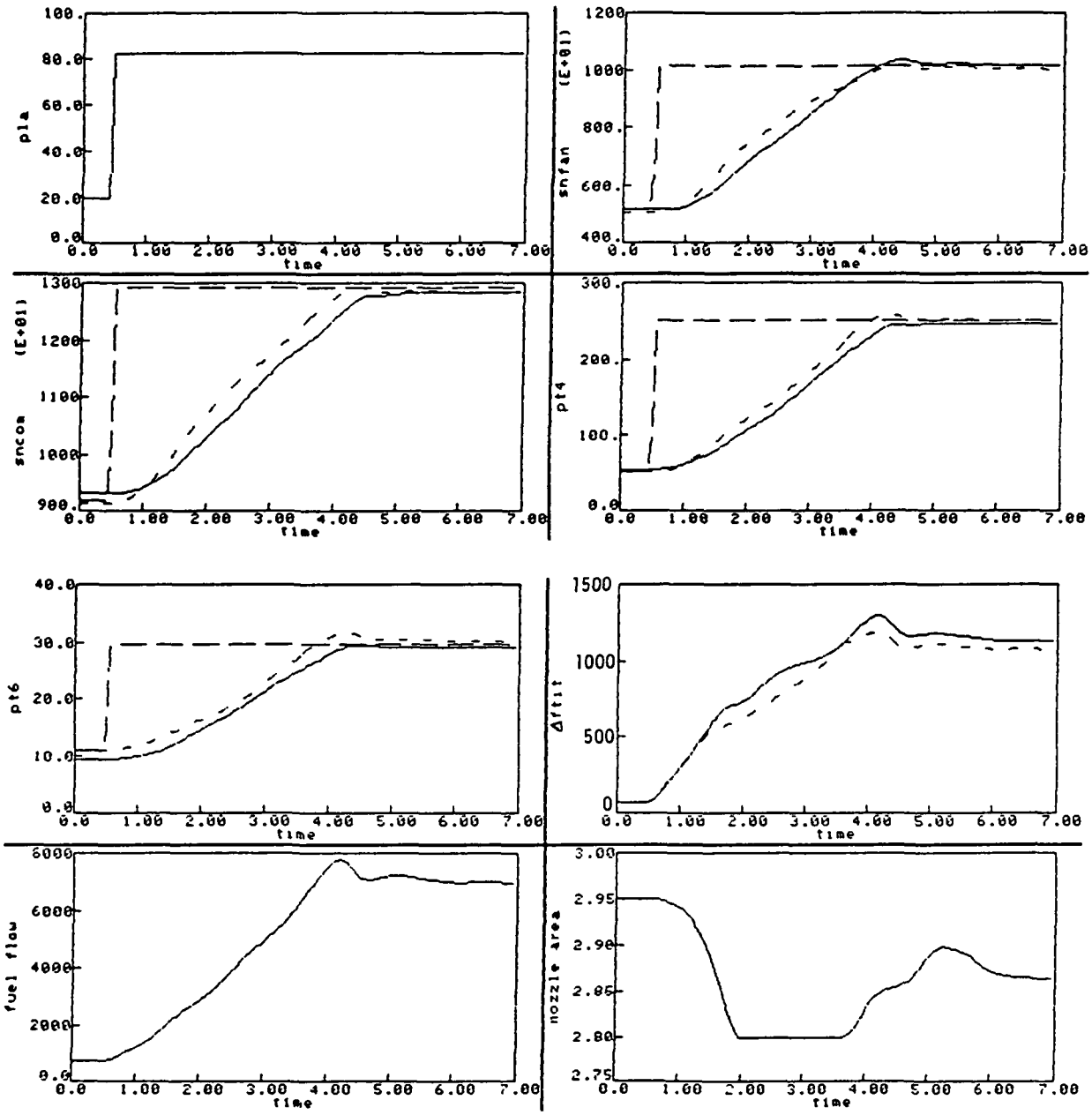

Figure 5-24 Transient Responses of the New Model Running "Piggyback" With Zero Filter Gains, for PLA Step from 20.0 Degrees to 83.0 Degrees at Altitude = 20000 ft and Mach No. = 0.75. Engine (————), Model Output (— — — —), Reference (——— ———)

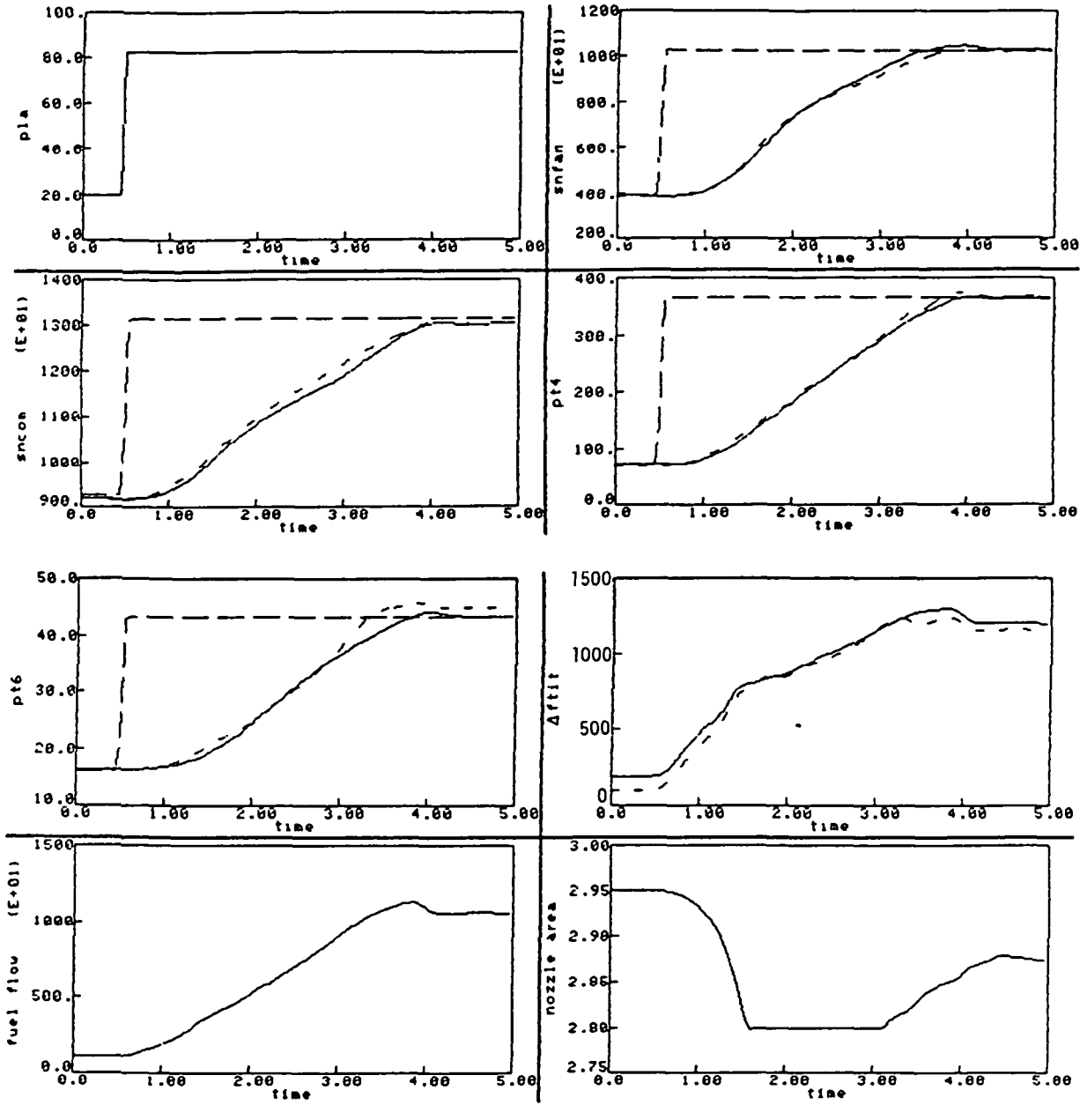

Figure 5-25 Transient Responses of the New Model Running "Piggyback" With Nonzero Filter Gains, for PLA Step from 20.0 Degrees to 83.0 Degrees at Altitude = 0 ft and Mach No. = 0. Engine (————), Model Output (— — — —), Reference (———— ————)

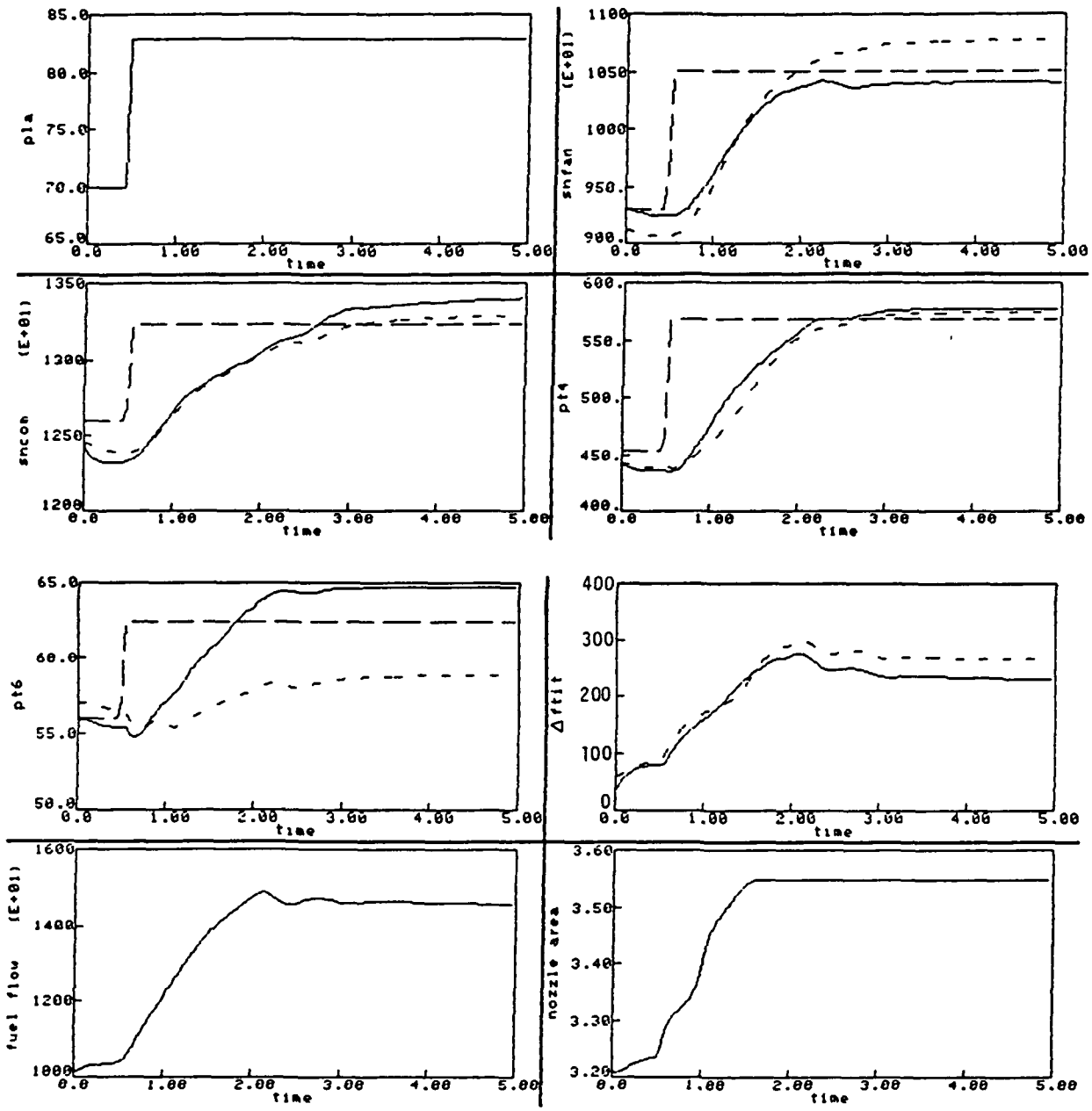

Figure 5-26 Transient Responses of the New Model Running "Piggyback" With Nonzero Filter Gains, for PLA Step from 70.0 Degrees to 83.0 Degrees at Altitude = 0 ft and Mach No. = 1.2. Engine (———), Model Output (— — — —), Reference (——— ———)

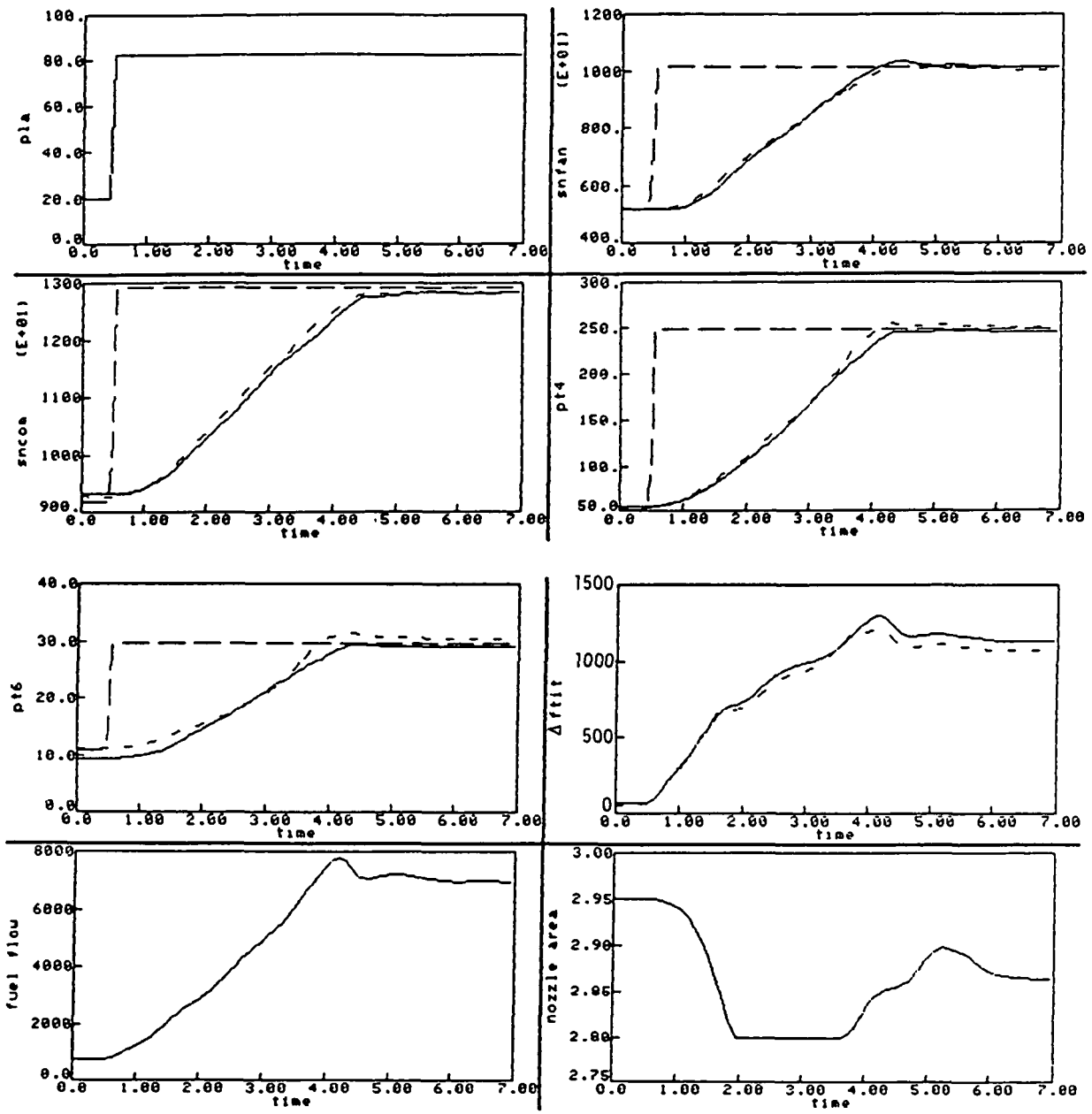

Figure 5-27 Transient Responses of the New Model Running "Piggyback" With Nonzero Filter Gains, for PLA Step from 20.0 Degrees to 83.0 Degrees at Altitude = 20000 ft and Mach No. = 0.75. Engine (————), Model Output (— — — —), Reference (———— ————)

5.5 MICROPROCESSOR REQUIREMENTS FOR THE DIA ALGORITHM

Microprocessor implementation requirements in terms of the cycle time and memory space occupied by the DIA algorithm were determined for implementation of the algorithm on an INTEL 8086 microprocessor. The goal was to meet the requirements of 15 msec cycle time and 8000 sixteen bit words (or 16k bytes) of memory space.

The approach taken to determine the microprocessor requirements was to obtain data for implementation of the algorithm on a VAX 11/780 at SCT's Resource Center. This data included memory usage and the cycle time. As part of the F100 Multivariable program, the control algorithm was programmed on an INTEL 8086 microprocessor by NASA LeRC. Therefore, the cycle time and memory space data was available for the control algorithm. Microprocessor implementation requirements for the DIA algorithm were estimated using data from both sources.

The following runs were made on the VAX system:

(i) F100 engine only
(ii) F100 engine + MVCS logic
(iii) F100 engine + MVCS logic + DIA logic

From (i) and (ii) the execution time for the MVC logic can be determined for the VAX system. From (ii) and (iii) the time taken by the DIA algorithm can be determined. The execution times are presented in Table 5-9. A comparison of the execution times indicate that the execution time requirement for the DIA algorithm may exceed the goal of 15 msec.

TABLE 5-9

CYCLE TIMES FOR THE MVC AND DIA ALGORITHMS

	MVCS Logic	DIA Logic
VAX 11/780	41 msec	46 msec
INTEL 8086	17 msec	19 msec

The multivariable control and DIA related routines were separately compiled on the VAX system to determine their memory usage. A comparison is presented in Table 5-10 which shows that the memory usage for the DIA algorithm should meet the goal.

TABLE 5-10

MEMORY USAGE FOR THE MVC AND DIA ALGORITHMS

	MVCS Logic	DIA Logic
VAX 11/780	19k bytes	16k bytes
INTEL 8086	13k bytes	11k bytes

SECTION 6

DETAILED EVALUATION OF THE SELECTED DIA ALGORITHM REVISION

A detailed evaluation of the revised detection, isolation and accommodation (DIA) algorithm was conducted by simulating various sensor failure scenarios at 15 flight operating points, using the nonlinear F100 engine and Multivariable Control (MVC) simulation. Where applicable failure scenarios existed from the referenced contract (NAS3-22481), comparisons were made to show the benefits of the algorithm revisions. The following paragraphs present the results of the evaluation.

6.1 Evaluation Approach

The approach used in developing the evaluation test plan was to demonstrate that the selected revision to the DIA algorithm addressed the shortfalls which were identified in the referenced contract.

As a first step, the fifteen flight operating points from the referenced contract were modified to arrive at an improved set of test conditions to conduct the evaluation. The flight operating points were modified to better span the flight envelope and to demonstrate modeling accuracy while still maintaining sufficient common flight operating conditions to enable a comparison with the evaluation completed under the referenced contract.

Figure 6-1 shows a flight envelope which indicates both the flight conditions at which the linear models were generated (see Section 3.1) and the flight operating points from the referenced contract. As shown, the flight operating points which were selected under the referenced contract do not completely span the envelope. Also, many points fall on or near a linear model point and therefore do not demonstrate the accuracy of the functional relationships which were developed for full flight envelope use.

Figure 6-2 shows the same flight envelope with the flight operating points as selected for this contract for the detailed evaluation. These conditions were selected to better span the outskirts of the flight envelope and also to be sufficiently far away from the linear models such that the accuracy of the simplified nonlinear model could be evaluated. In the selection of these flight operating points, it was noted that the reference point schedules in the multi-variable control are valid to an altitude of 65000 feet. Therefore, this was a limiting factor in the selection of the flight operating points.

6.2 Evaluation Results

6.2.1 Steady State Comparison

Steady State failure effects were evaluated at the fifteen flight operating points selected for this evaluation. The failures were induced by applying a constant bias to the sensor to be failed. The magnitude of the biases applied to the sensor values were:

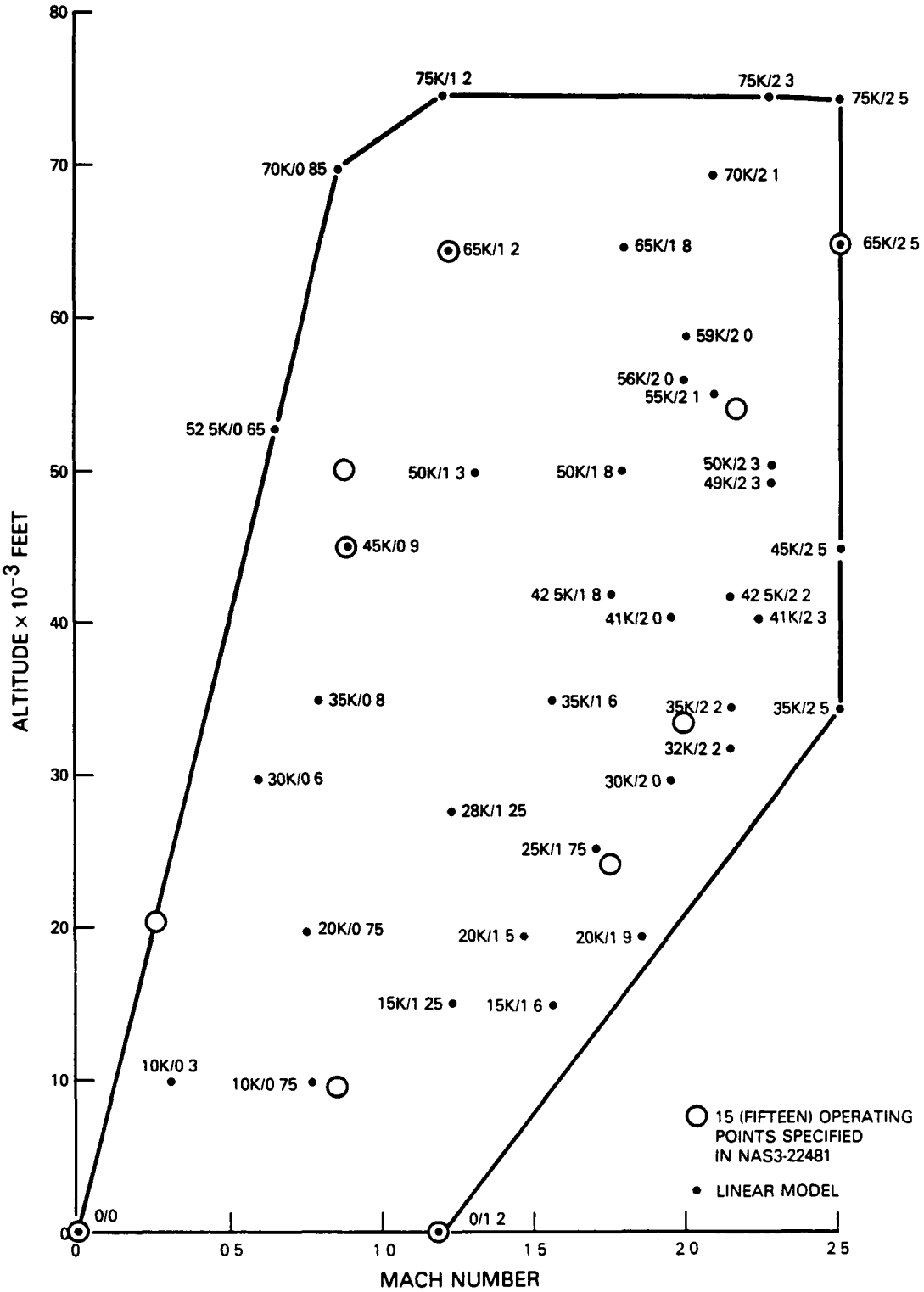

Figure 6-1 F100 Flight Envelope Illustrating Fifteen Test Points Specified in NAS3-22481 Relative to Linear Model Points

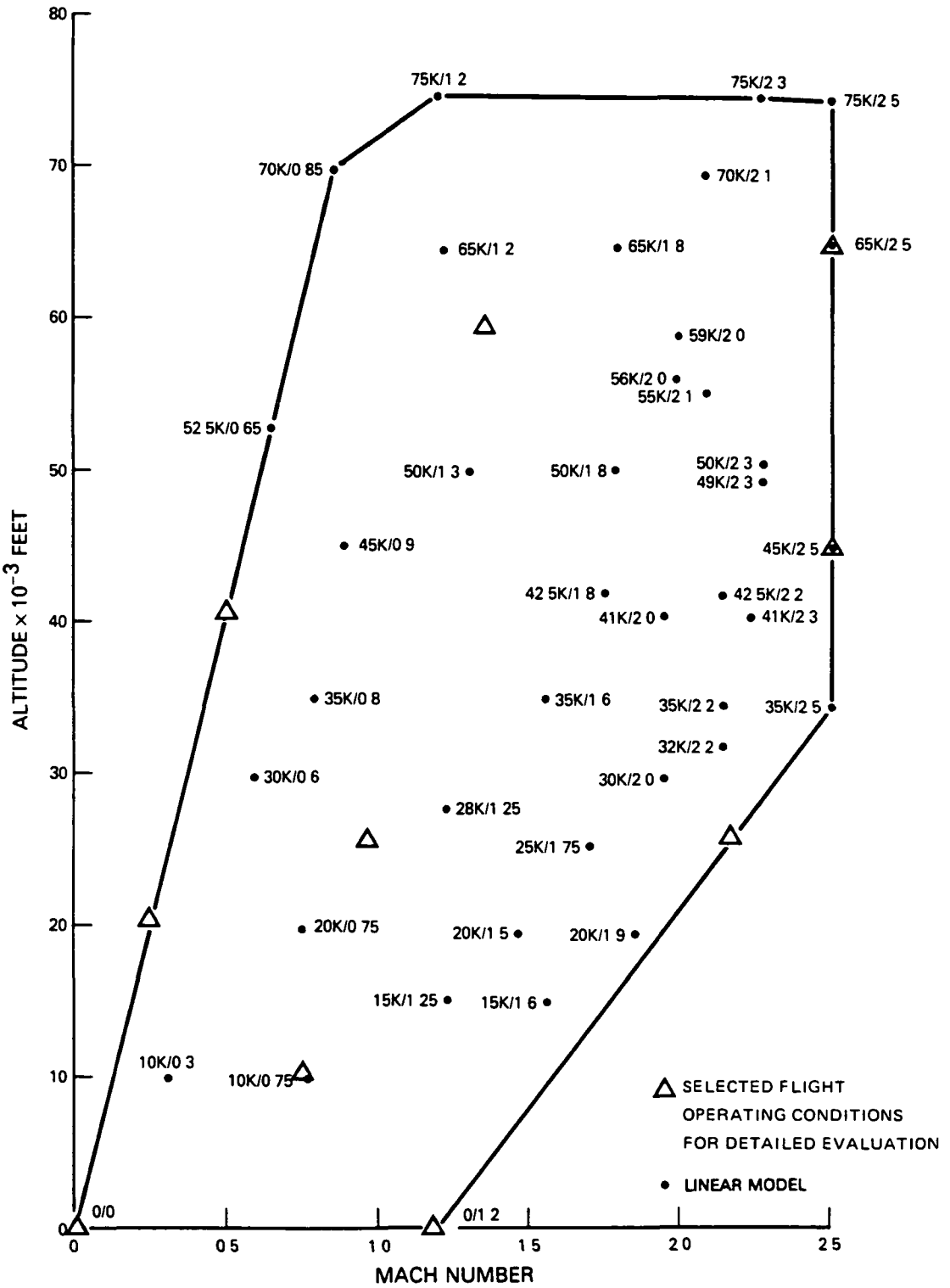

Figure 6-2 F100 Flight Envelope Illustrating Selected Test Points Relative to Linear Model Points

Fan Speed (N1) - 2000 RPM
Compressor Speed (N2) - 2000 RPM
Augmentor Total Pressure (PT6) - 35 psi
Burner Pressure (PT4) - 100 psi
Fan Turbine Inlet Temperature (FTIT) - 500°F

Since the purpose of this test was to observe the accommodation accuracy of the algorithms, the biases were set arbitrarily large to ensure failure detection. After the failure was detected, isolated, and accommodated and the failure transient decayed, the estimation error in the affected sensor was recorded as well as changes in thrust, and fan and compressor surge margins. The estimation errors were calculated by taking the difference between the actual parameter and the estimator outputs. Where similar test cases existed from the referenced contract, comparisons were made with the appropriate data for both the DIA algorithm and parameter synthesis algorithm from the previous contract.

Table 6-1 presents the results of this evaluation. As seen in this table, the revised DIA algorithm has comparable estimation errors to the baseline DIA algorithm from the referenced contract. This was anticipated since the steady state schedules within the filter's engine model were not modified as part of this program. In general, the percent change in thrust, from the correct steady state level, with the revised algorithm is significantly less than that with the baseline algorithm since the revised algorithm eliminates the effect of filter biases.

The previous contract showed that neither the DIA algorithm nor the parameter synthesis technique provided adequate FTIT protection when operating on the synthesized or estimated value. Both of the FTIT failure cases examined with the revised algorithm showed adequate FTIT protection for hard over failure. The DIA performance of the FTIT estimator will be discussed further in subsequent sections.

6.2.2 Typical Failure Transients

When the steady state failures were induced, the resulting engine perturbation transients were observed. Figure 6-3 shows a comparison of failure transients between Parameter Synthesis, the baseline Advanced DIA algorithm and the revised DIA algorithm for an N2 out-of-range failure induced at time=3.0 seconds. It can be seen that when the failure is induced, the revised DIA algorithm follows the N2 sensor (failed high) until the failure is detected and isolated. The N2 sensor is then replaced with the estimated N2 resulting in the failure transient shown.

The resulting thrust comparisons show the revised DIA algorithm and the Parameter synthesis technique both at the desired thrust level prior to the failure. Since the baseline DIA algorithm feeds back estimates to the multivariable control in the case of no failures, the estimator biases result in a steady state hangoff. A 468 pound thrust error is shown prior to the failure. When the failure is induced, the Parameter Synthesis shows a larger

TABLE 6-1

STEADY STATE COMPARISONS OF REVISED DIA ALGORITHM,
BASELINE DIA ALGORITHM AND PARAMETER SYNTHESIS WITH FAILURES INDUCED

FAULT OPERATING PT.	PARAMETER FAILED	REVISED DIA ALGORITHM				BASELINE DIA ALGORITHM				PARAMETER SYNTHESIS			
		ESTIMATION ERROR IN FAILED PARAMETER	THRUST CHANGE %	CHANGE IN FAN SURGE MARGIN	CHANGE IN COMP SURGE MARGIN	ESTIMATION ERROR IN FAILED PARAMETER	THRUST CHANGE %	ΔSMF %	ΔSMC %	ESTIMATION ERROR IN FAILED PARAMETER	THRUST CHANGE %	ΔSMF %	ΔSMC %
0/0 24°	N1 –	+ 55	+ 2.1	– 0.1	~ 0	+ 100	+ 5 3	– 0 15	+ 1 2	– 156	– 6.2	– 0.02	– 1 0
0/0 40°	P6 –	+ 0.06	+ 0.1	~ 0	~ 0								
0/0 83°	P4 –	– 4.2	~ 0	~ 0	~ 0	– 5 5	– 3 1	+ 2.1	– 0.15	– 5 0	– 1 3	+ 1.2	+ 0.5
0/1.2 83°	FTIT +	– 22 5°F	– 1	+ 0.1	~ 0								
10K/0 75 50°	N2 –	– 102	+ 0.6	– 0.1	+ 1								
10K/0 75 83°	N1 +	+ 60	~ 0	~ 0	~ 0	+ 15	– 2 2	+ 1 0	– 1 3	– 420	– 3 4	– 4.5	0
20K/0 3 40°	P6 +	– 0 33	+ 1% +	– 0.1	~ 0	– 0 49	– 4 9	+ 0 5	– 0 4	– 0 15	0	– 0.1	– 0.25
20K/0 3 83°	N2 +	– 70	+ 0 15	– 0.2	– 0.3	– 70	– 5 5	+ 4 23	– 1 3	– 30	– 0.15	+ 0.02	+ 0 3
25K/1 0 83°	FTIT –	+ 4 23	~ 0	+ 0 1	~ 0								
25K/2 2 83°	N2 +	+ 370	~ 0	~ 0	+ 2								
40K/0 6 40°	P4 +	– 6 3	– 47 6	+ 3	– 2								
40K/0 6 83°	N1 +	+ 550	+ 7 5	+ 2.5	– 0.2								
45K/2 2 83°	N2 –	– 25	~ 0	– 0 1	– 0 2								
60K/1 2 83°	P6 –	– 0 36	– 0 9	+ 0 3	– 0 1	– 0 18	+ 7 1	+ 2 5	– 1 1	+ 0 47	+ 0 4	+ 0 4	– 0 6
65K/2 5 83°	P4 +	+ 21	+ 0 2	~ 0	~ 0								

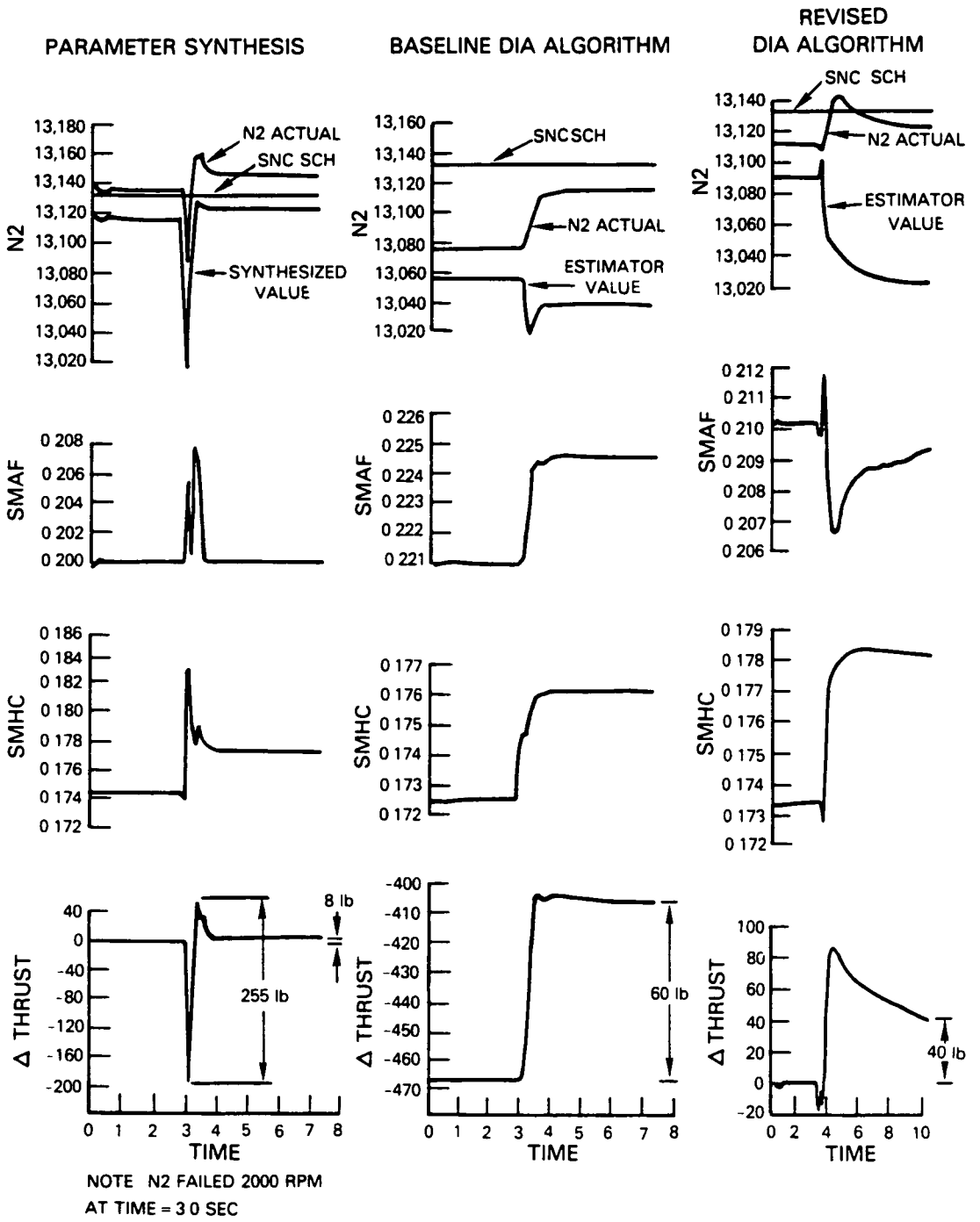

Figure 6-3 Failure Transient Comparisons for an N2 Failure at Sea Level Static, 83 Degrees Power Lever Angle

thrust perturbation than the baseline and revised DIA algorithms. This is to be expected since the Parameter Synthesis algorithm switches from the failed sensor value to the estimate when the failure is detected and isolated, whereas the baseline and revised algorithms reconfigure the filter to eliminate the failed sensor from the estimator calculations. (In the revised DIA algorithm, the estimated N2 is always fed back to the LQR portion of the control mode.) The revised algorithm exhibits a similar magnitude thrust transient as the baseline algorithm but will settle to a lower magnitude steady state error since the actual values of N1 and PT6 are being fed back to the integral portion of the control mode.

Figure 6-4 shows a comparison of N1 sensor failure transients between the baseline DIA algorithm and the revised DIA algorithm. The baseline DIA algorithm shows steady state N1 hangoff error prior to the failure between the actual N1 and the schedule value whereas this error is eliminated with the revised algorithm, since the actual values of N1 and PT6 are fed back to the integral portion of the control mode. After the N1 sensor failure is detected, isolated and accommodated, both the baseline and revised algorithms feed estimated N1 to the integral mode and, therefore, exhibit similar hangoff errors.

6.2.3 Detection/Isolation Accuracy

To evaluate the detection and isolation performance of the revised DIA algorithm, slow sensor drifts were simulated at the fifteen flight operating points. When the failure was detected and isolated, the magnitudes of the biases and thrust variation were recorded as tabulated in Table 6-2. For the most part, the detection accuracy was shown to be generally equal between the baseline DIA algorithm and the revised DIA algorithm.

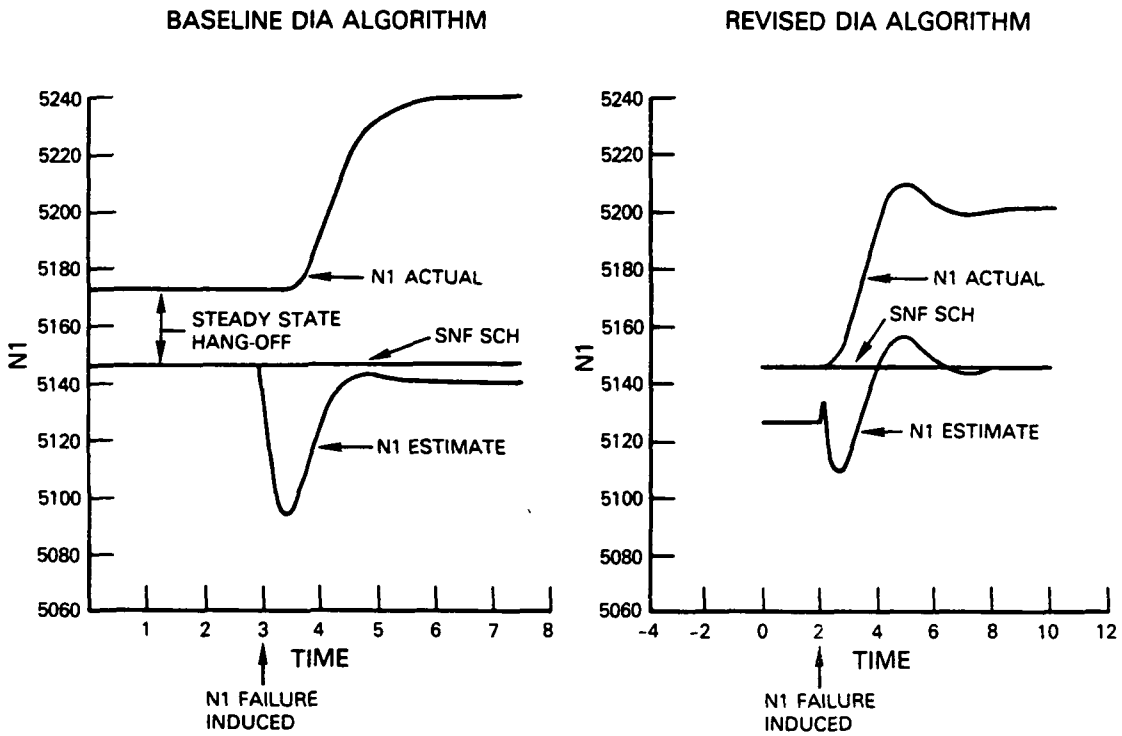

Figure 6-4 Comparisons of N1 Failure Transients Between Baseline DIA Algorithm and Revised DIA Algorithm

TABLE 6-2

STEADY STATE RESULTS OF SLOW DRIFT
FAILURE TRANSIENTS

FLIGHT OPERATING POINT	FAILURE	REVISED DIA ALGORITHM				PARAMETER SYNTHESIS		BASELINE DIA ALGORITHM	
		PARAMETER BIAS BEFORE DIA	ΔFNT BEFORE DIA	TIME FOR DIA	COMMENTS	BIAS BEFORE DIA	ΔFNT	BIAS BEFORE DIA	ΔFNT
0/0 24° PLA	P6	7 5 PSI (42%)	– 4 5%	0 490 SECONDS	–	+ 12 7	– 3 5%	+ 5 68	+ 0 1%
0/0 40° PLA	N1	1333 RPM (12 1%)	– 44 5%	1 994 SECONDS	–				
0/0 83° PLA	PT4	46.5 PSI (12 7%)	– 0 1%	3 080 SECONDS	FILTER NOISY DURING FDIA	+ 32 PSI	– 5 6%	+ 44 3	– 0 2%
0/1 2 83° PLA	FTIT	90°F (5.2%)	-2.2%	2.53 SECONDS	–	+ 78°F	– 20 3	+ 114°F	0%
10K/0 75 50° PLA	PT4	40 5 PSI (19 6%)	– 0 2%	2 664 SECONDS	–				
10K/0 75 83° PLA	PT6	9 PSI (21 8%)	– 1 5%	0 572 SECONDS	–				
20K/0 3 40° PLA	N2	UNDETECTED		UNDETECTED	UNSTABLE DIVERGING		– 3 2	+ 1419	– 6 5%
20K/0 3 83° PLA	N2(–)	UNDETECTED		UNDETECTED	UNSTABLE	– 390	+ 2 3	UNDETECTED	+ 10 5%
20K/0 3 83° PLA	N2	1415 (11 4%)	– 4 5%	3 518 SECONDS	–	+ 473 RPM			
25K/1 0 83° PLA	PT4	46 5 PSI (18 1%)	– 0 2%	3 066 SECONDS	–				
25K/2 2 83° PLA	PT4	FALSE ALARM	–	–	PT4 & PT6 FALSE ALARMS PRIOR TO FAILURE				
40K/0 6 40° PLA	N2	MISS	> – 48%	–	2000 RPM DRIFT MISS				
40K/0 6 83° PLA	PT6	6 75 (63 7%)	– 0 5%	0 448 SECONDS	SYS OCCILITORY AFTER FAILURE INDUCED				
45K/2 2 83° PLA	P4	– 56 4 (– 24 5%)	– 0 16%	3 750 SECONDS	–				
60K/1 2 83° PLA	N2	2000 (15 8%)	– 19 4%	5 016 SECONDS	DRIFT CAUSED SYSTEM TO GO UNSTABLE				
65K/2 5 83° PLA	P6	– 3 75 (– 27 4)	+ 24 7%	0 400 SECONDS	FTIT FALSE ALARM IN 0 25 P6 DIA @ 0 4 SEC				

Figures 6-5 and 6-6 show time histories of pertinent engine performance parameters responding to a PT4 drift failure with the baseline and revised DIA algorithms, respectively. A comparison of the two results shows that the revised DIA algorithm performed similar to the baseline algorithm, and in most cases the accommodation transient was of a smaller magnitude. The results with the revised algorithm did, however, exhibit an apparent oscillatory mode on fuel flow as can be seen from the PT4 and compressor surge margin (SMHC) plots. The cause of this stability problem was not determined, but may result from an interaction between the filter with the revised gain matrix and the multivariable control mode. It is not felt to be a result of the algorithm revision (for eliminating hang-off errors). This problem should be evaluated in more detail during NASA's hybrid simulation evaluation.

Figures 6-7 and 6-8 show time histories of pertinent engine performance parameters responding to a negative N2 drift failure with the baseline DIA algorithm and the revised DIA algorithm, respectively. Both versions of the DIA algorithm failed to detect the failure for a 2000 RPM drift. This is due to the fact that the design of the Kalman filter gains results in a high weighting being placed on the N1 and N2 sensors, since they are predominant states in the simplified nonlinear engine model. Thus, the estimator tracks the failed sensors and the residuals do not increase sufficiently to indicate a failure. In the revised algorithm design, a conscious effort was made to more evenly distribute the weighting of the gain matrix among the input parameters, however, the weighting on the rotor speed still remained large relative to the other parameters. An evaluation of further adjustments to filter gain matrix elements during NASA's hybrid simulation evaluation would be beneficial.

Figures 6-9 and 6-10 show time histories of pertinent engine performance parameters responding to a positive N2 drift with the baseline DIA algorithm and the revised DIA algorithm, respectively. As with the above negative N2 drift case, the positive drift results in the estimate following the failed sensor value. However, with this failure scenario, the failure was detected, isolated, and accommodated by both versions of the DIA algorithm after a 1400 RPM drift. In both cases, the failure transients were similar. Transients in the estimator outputs are generally larger for the revised algorithm, since its estimator appears to be tracking the failed N2 sensor closer than the estimator for the baseline algorithm.

This study showed that the baseline DIA algorithm and the revised DIA algorithm respond similarly to slow drift failures. Even though the revised DIA algorithm Kalman filter gains were designed to more evenly distribute the weighting for the input parameters, the rotor speeds still remained dominant relative to the other inputs. As a result, the DIA algorithms were not effective in isolating N1 and N2 drifts. It is therefore concluded that either the filter gains should be adjusted to reduce the weighting on parameters which are the dominant states of the engine model within the DIA algorithm or other means should be provided for in-range drift failure coverage.

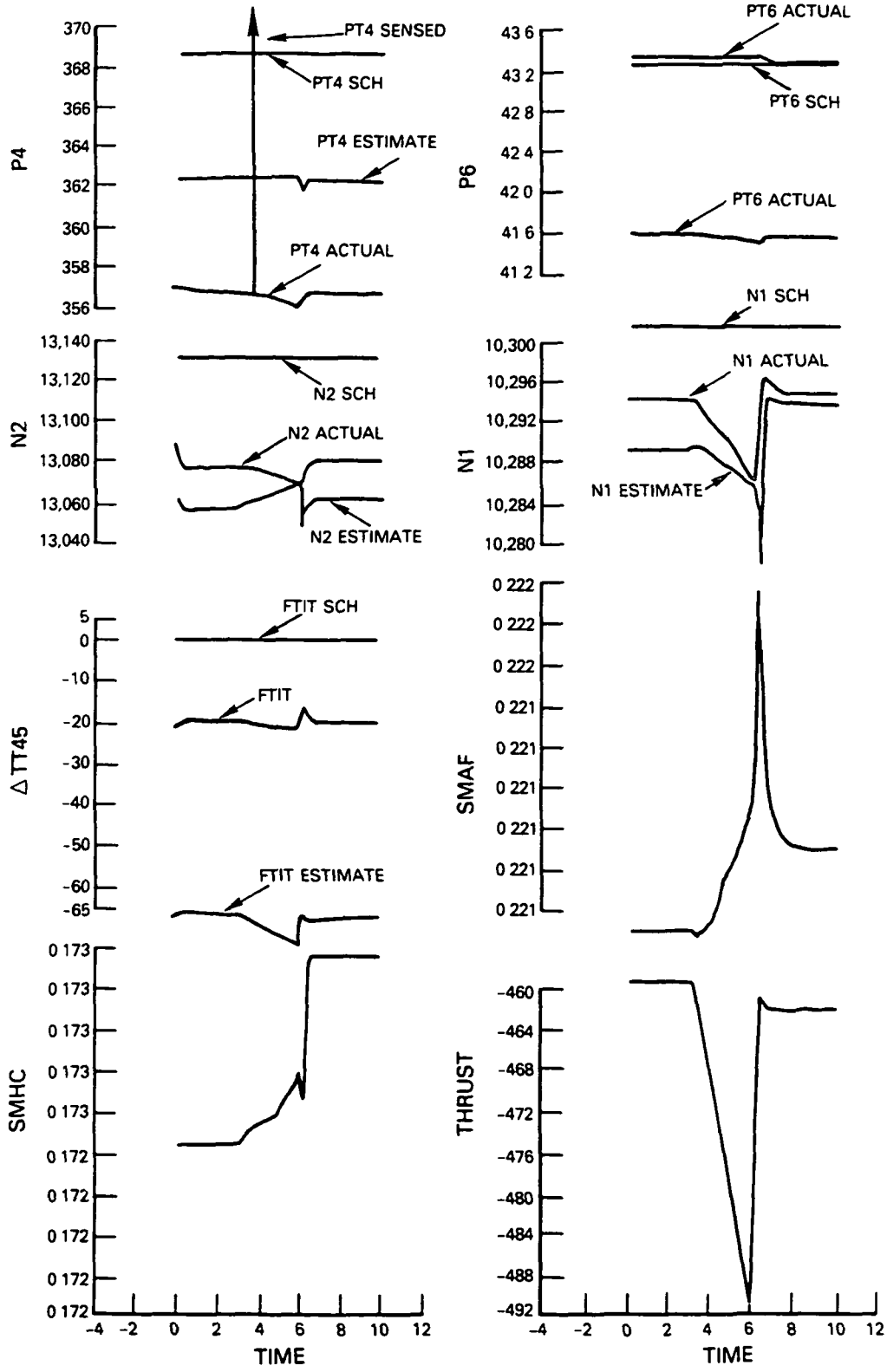

Figure 6-5 Transient Results with the Baseline DIA Algorithm for a PT4 Sensor Drift (15 psi/sec) Sea Level Static 83° PLA

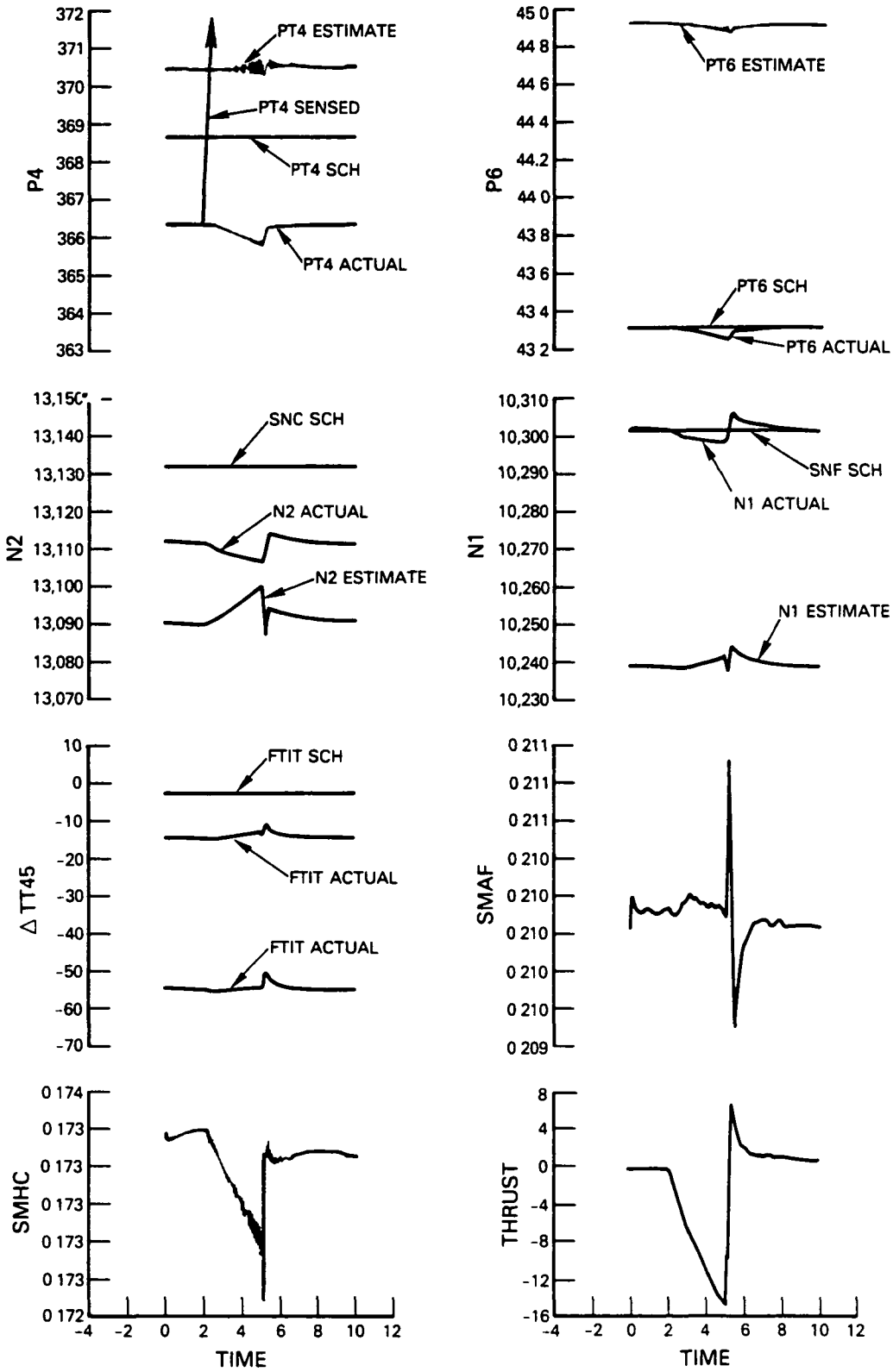

Figure 6-6 Transient Results with the Revised DIA Algorithm for a PT4 Sensor Drift (15 psi/sec) Sea Level Static 83° PLA

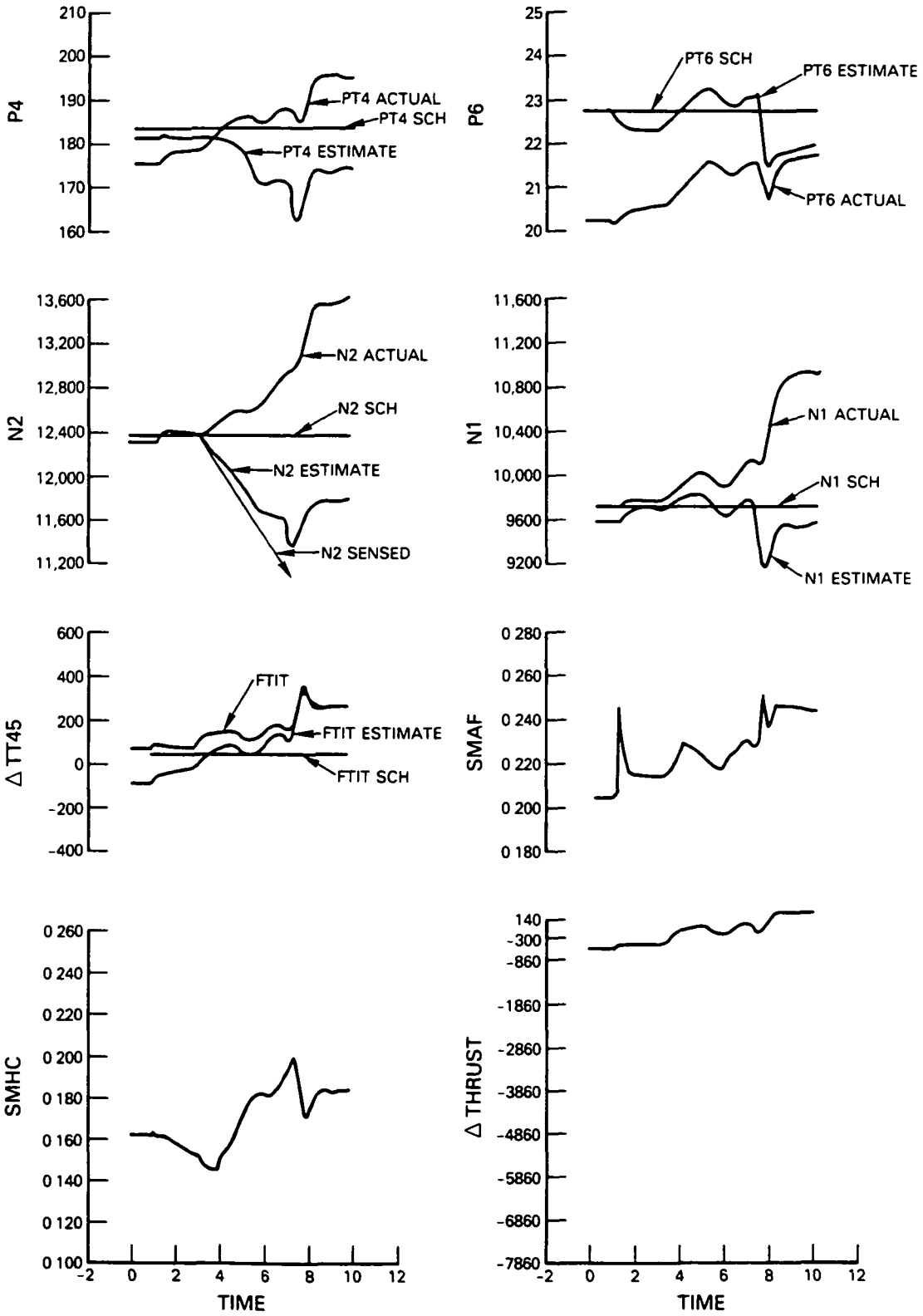

Figure 6-7 Transient Results with the Baseline DIA Algorithm for an N2 Sensor Drift (-400 rpm/sec) 20K/0.3 Mn, 83° PLA

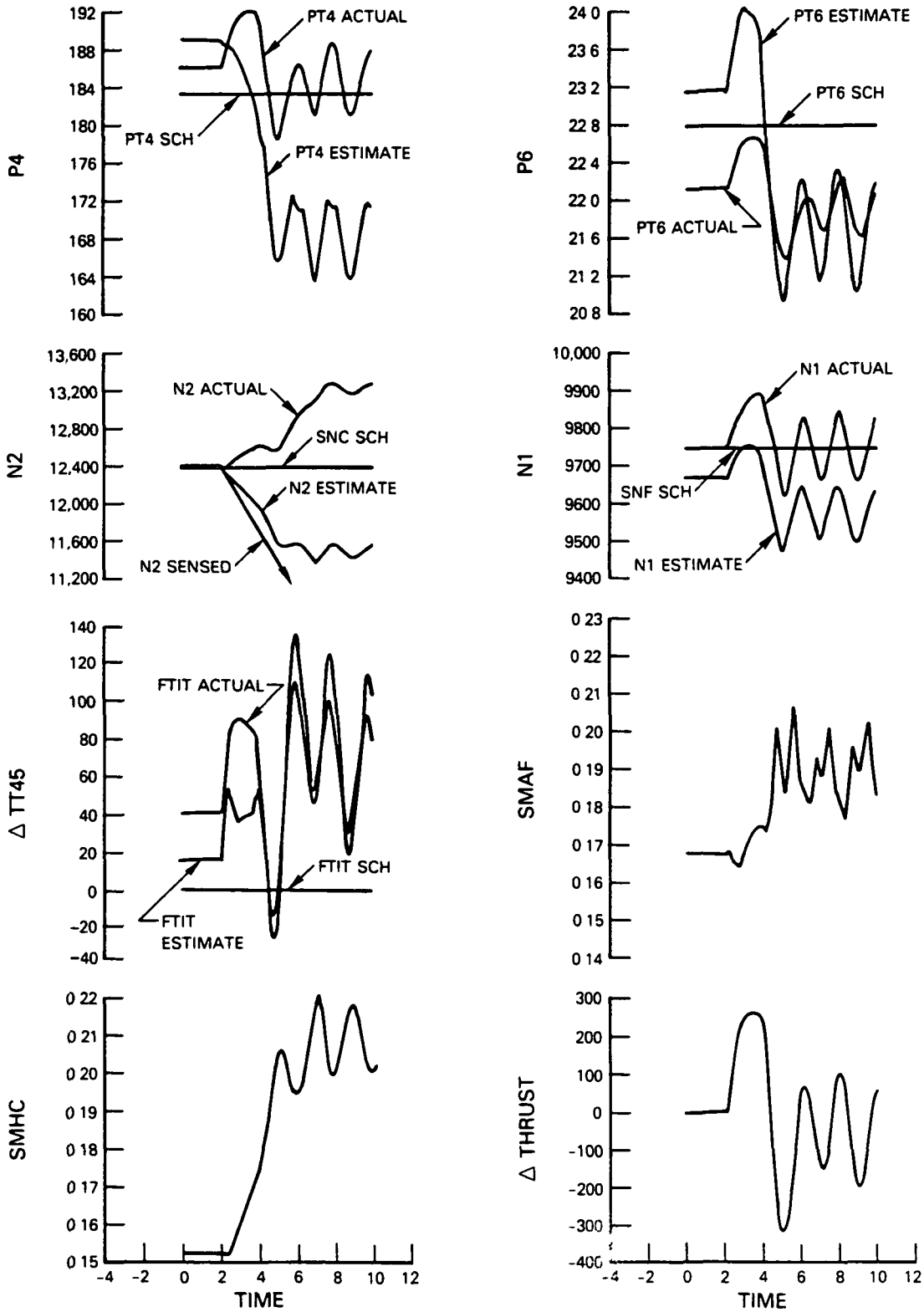

Figure 6-8 Transient Results with the Revised DIA Algorithm for an N2 Sensor Drift (-400 rpm/sec) 20K/0.3 Mn, 83° PLA

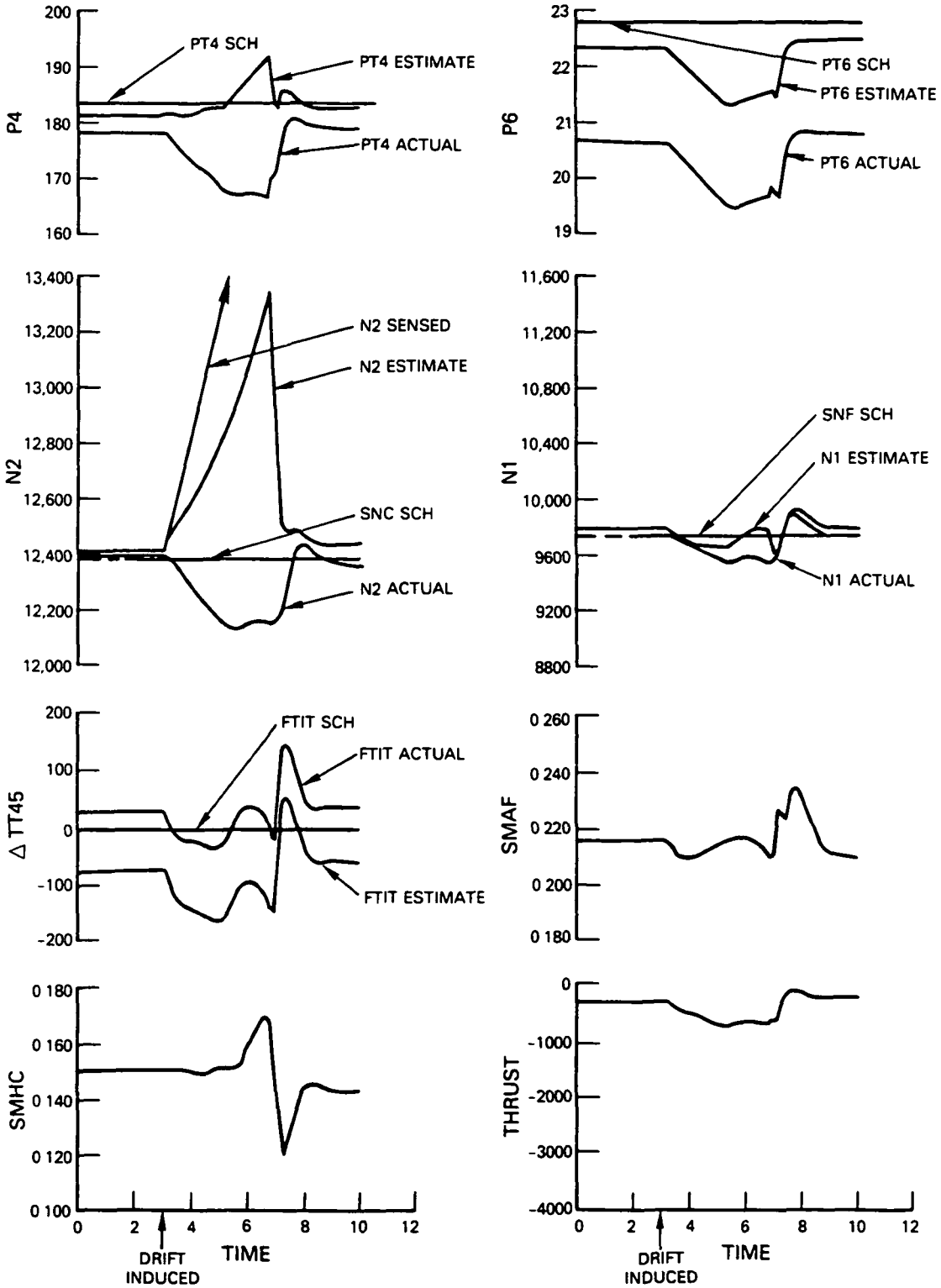

Figure 6-9 Transient Results with the Baseline DIA Algorithm for an N2 Sensor Drift (+400 rpm/sec) 20K/0.3 Mn, 83° PLA

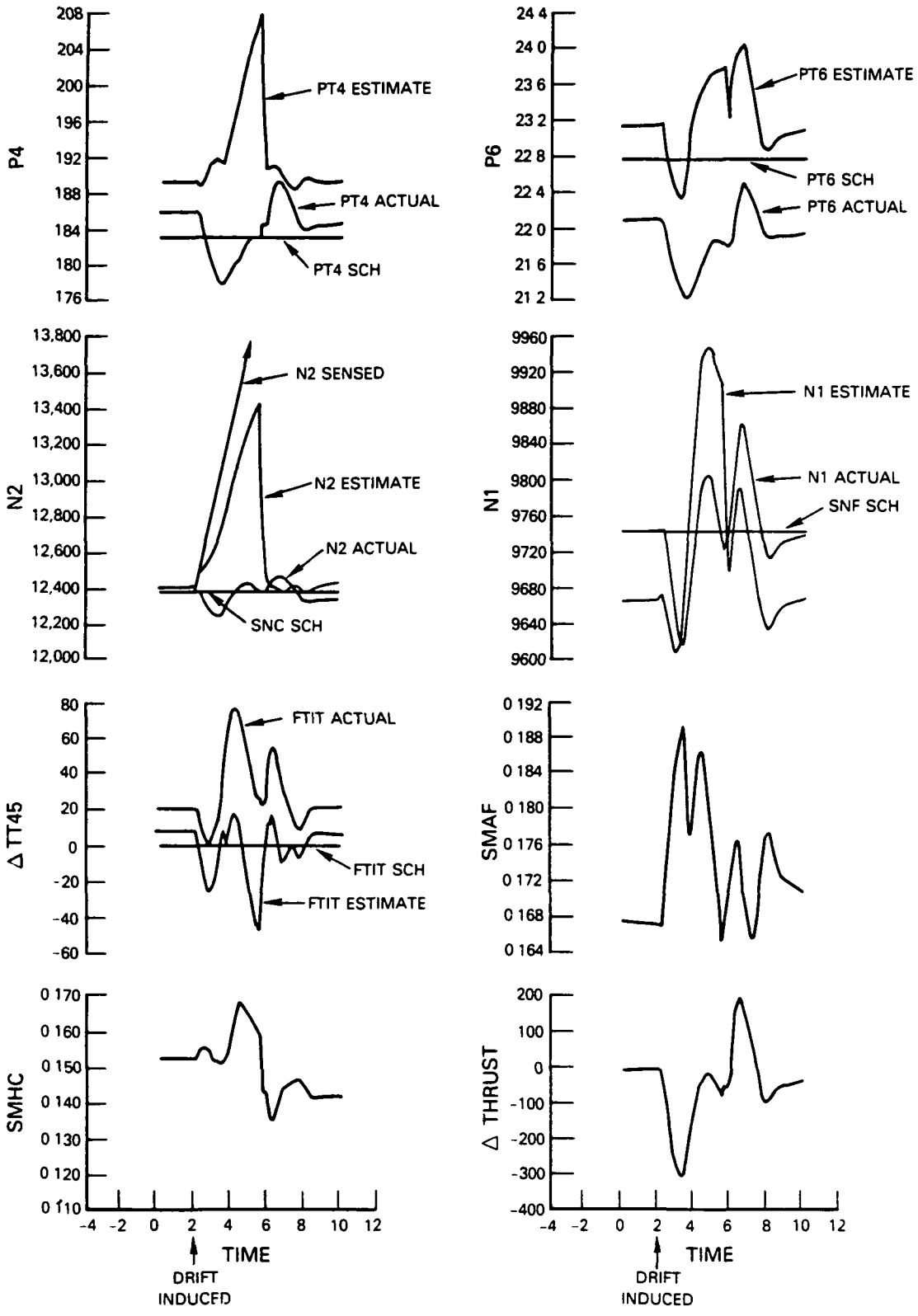

Figure 6-10 Transient Results with the Baseline DIA Algorithm for an N2 Sensor Drift (+400 rpm/sec) 20K/0.3 Mn, 83° PLA

6.2.4 Transient Failure Comparisons

Sensor failures were induced during large perturbation transients to compare transient detection and isolation capability as well as observe the engine's transient behavior when operating with the accommodation of a failed sensor. Figure 6-11 shows the resulting transient response to a large perturbation acceleration transient when operating on a failed PT4 sensor at sea level static for the baseline DIA algorithm and the revised DIA algorithm. Both versions of the DIA algorithm performed well.

Figure 6-12 shows the resulting transient response to a large perturbation deceleration transient when operating on a failed N2 signal at 20000 feet/0.3 Mn. The transient responses of the two versions of the algorithm are shown to have comparable trends. The "hangup" evident in the transient for the revised DIA algorithm is the result of the trim integrator clamping logic in the multivariable control mode.

6.2.5 Multiple Sensor Failures

Multiple sensor failures, consisting of PT4 and N2 sensor failures, were simulated at sea level static conditions to compare the two versions of the DIA algorithms capability to detect, isolate, and accommodate a second sensor failure. For this case, both the revised and baseline algorithms detected, isolated and accommodated both failures and demonstrated similar transient performance, as indicated by the thrust transients shown on Figure 6-13. This figure compares the thrust variations relative to the perfect sensor feedback case. As shown on this figure, the thrust for the revised algorithm case is slowly being trimmed down to a level within 40 pounds of its initial thrust level, whereas the baseline algorithm suffers a performance degradation of 57 pounds with the second failure.

Multiple sensor failure transient response was also evaluated for the two revisions of the DIA algorithm by simulating an N1/PT6 failure combination at sea level static 20° PLA conditions, followed by a snap PLA perturbation from 20° to 83°. These results are shown on Figures 6-14 and 6-15. The revised algorithm showed better transient response which results from improving the simplified nonlinear simulation within the DIA algorithms filter.

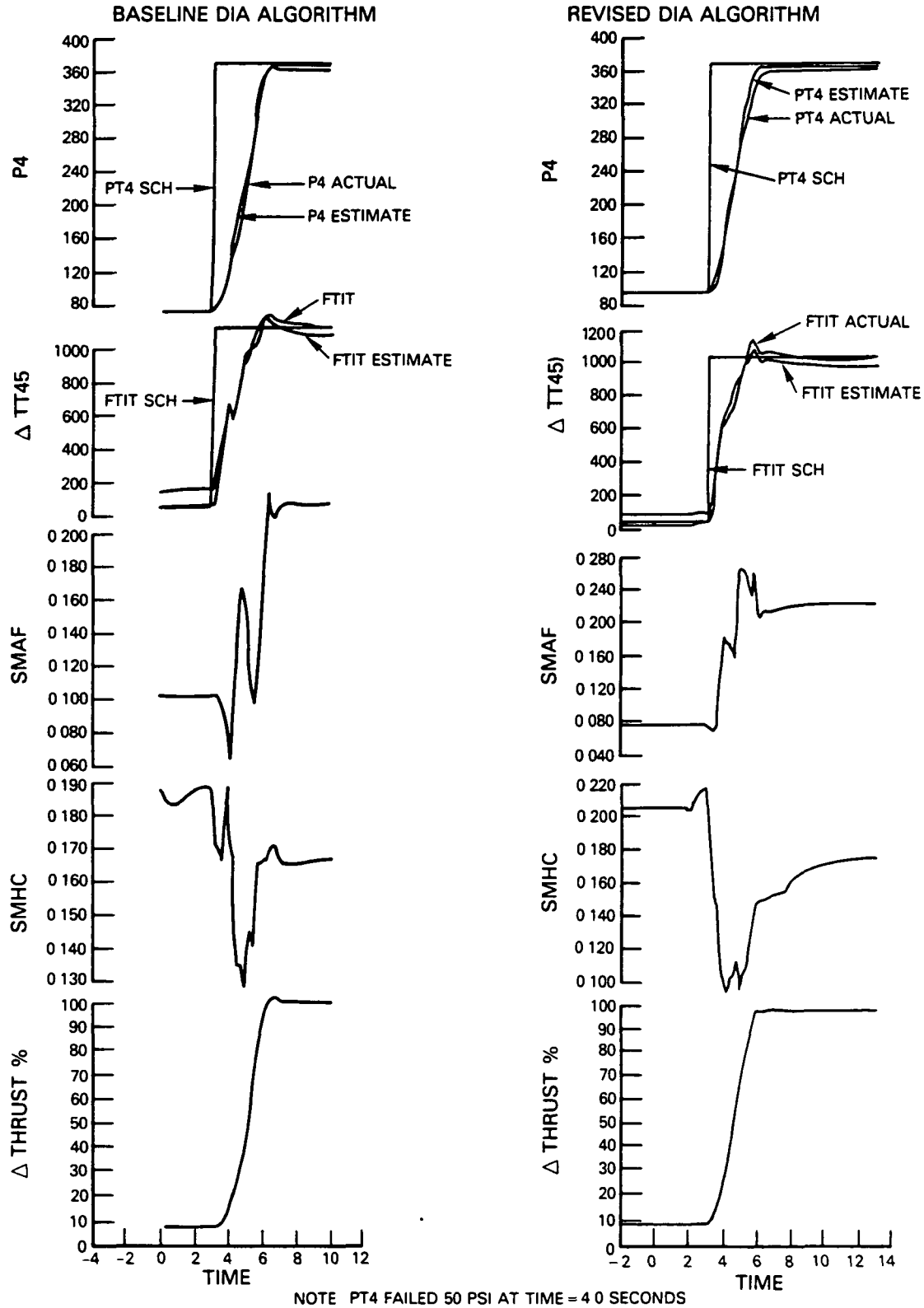

Figure 6-11 Failure Transient Comparisons for a PT4 Sensor Failure at Sea Level Static and 83° PLA

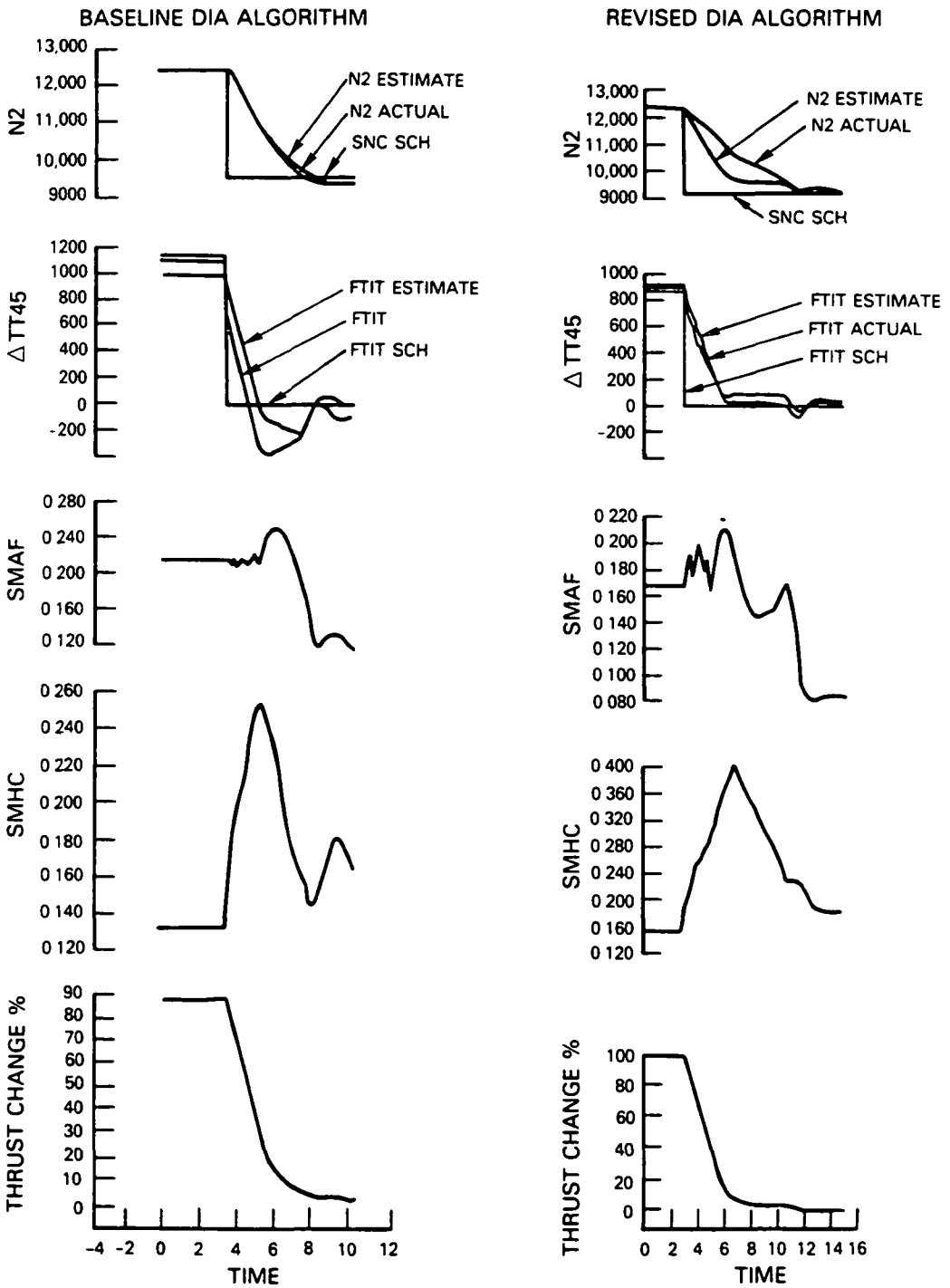

Figure 6-12 Failure Transient Comparisons at 20,000 ft/0.3 Mn and an 83° to 24° Snap Decel Occurring at 3 Seconds. An N2 failure was induced at time = 4.0 seconds.

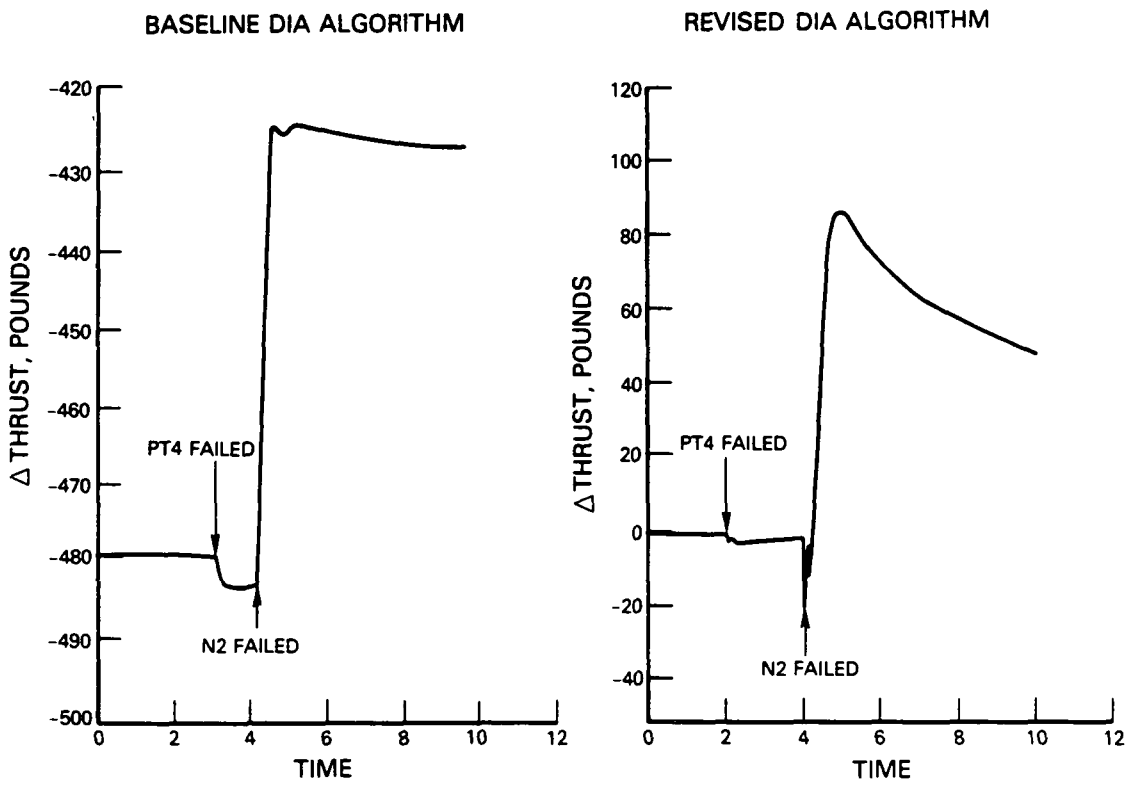

Figure 6-13 Thrust Transients Resulting from a Multiple Failure of the PT4 and N2 Sensors

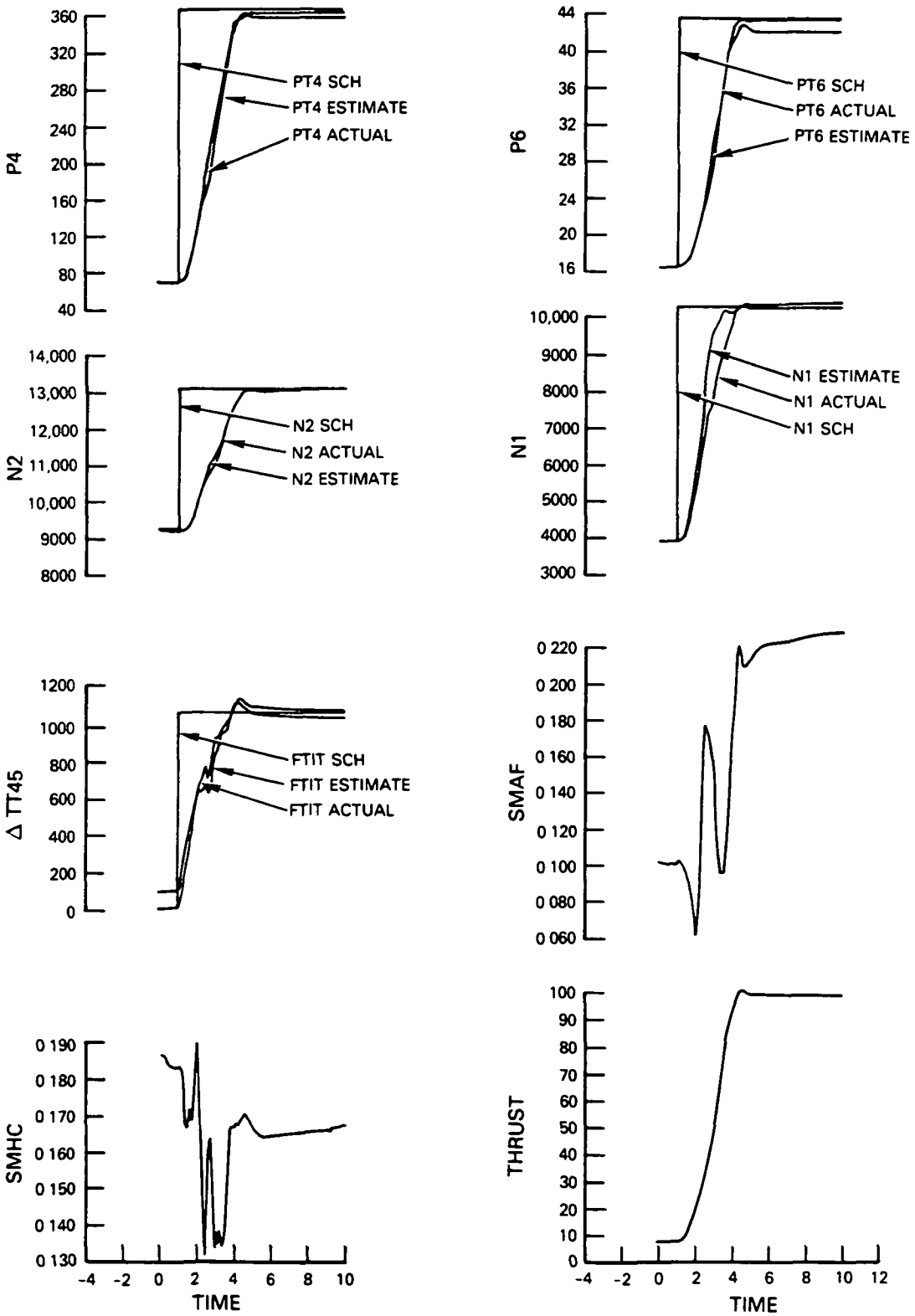

Figure 6-14 Thrust Transient Resulting from a PLA Snap from 20° to 83° Sea Level Static with PT6 and N2 Sensors Failed Operating with the Baseline DIA Algorithm

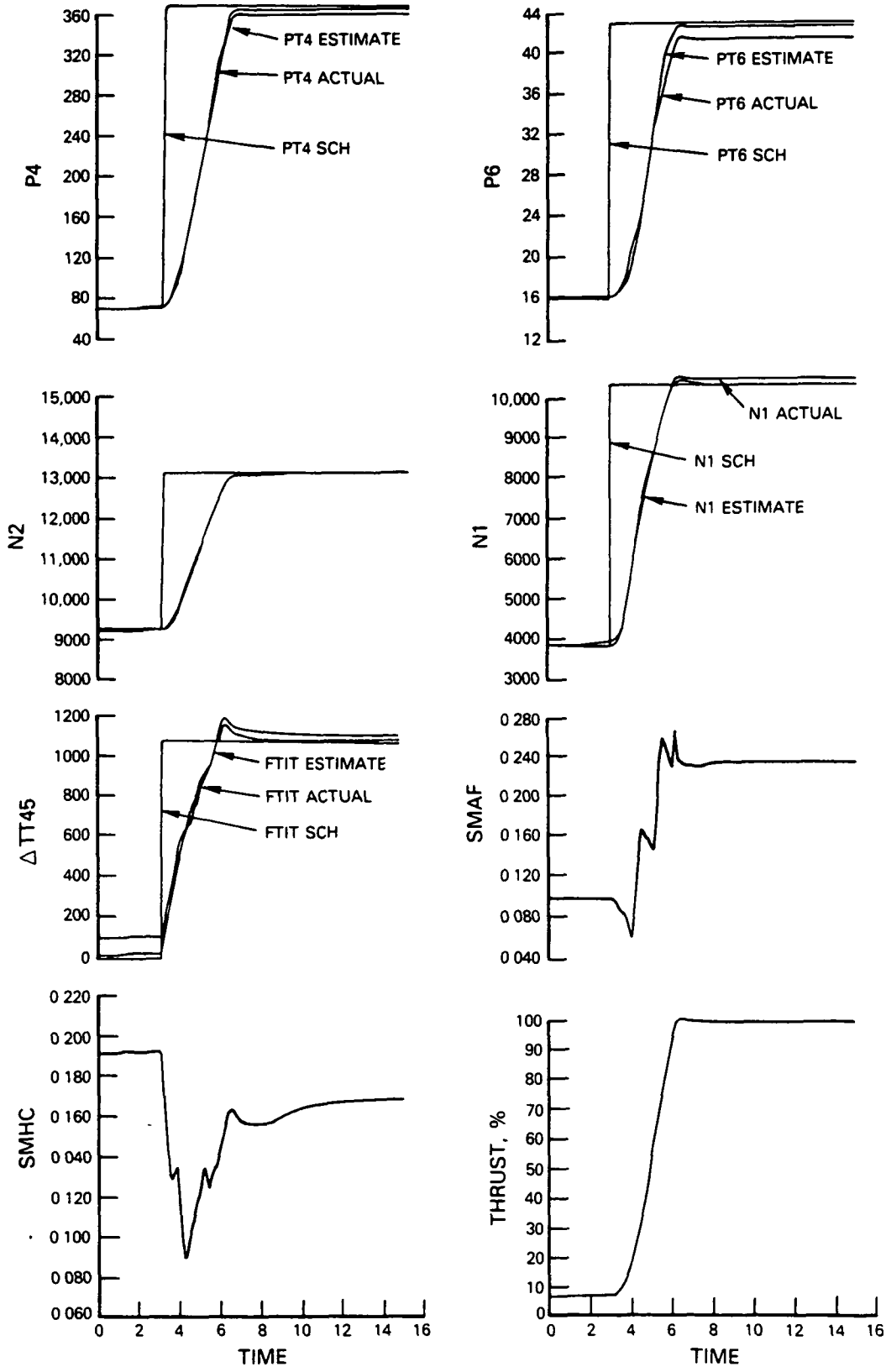

Figure 6-15 Thrust Transient Resulting from a PLA Snap from 20° to 33° Sea Level Static with PT6 and N1 Sensors Failed Operating with the Revised DIA Algorithm

SECTION 7

CONCLUSIONS

7.1 A comparative evaluation of the three potential revisions, to the sensor failure detection, isolation and accommodation (DIA) algorithm, for eliminating the effect of filter biases on the steady state operating point resulted in the following conclusions.

7.1.1 All three revisions are effective in eliminating the errors in the steady state operating points caused by biases on filter outputs, without affecting the DIA algorithm's capability to detect, isolate and accommodate sensor failures.

7.1.2 Revisions 1 and 2 are far less complex than Revision 3 which utilized supplementary trim integrators in the estimator and requires special manipulation of the detection threshold.

7.1.3 The Revision 3 version of the DIA algorithm results in slower convergence to steady state conditions due to the additional dynamic lag associated with the supplementary trim integrators in the estimator.

7.1.4 Revision 2 represents the best compromise in terms of complexity and performance for the three revisions evaluated, and was therefore selected for detailed evaluation on the nonlinear F100 engine/multivariable control (MVC) simulation.

7.2 A comparison of the revision 2 DIA algorithm with the baseline DIA algorithm on the detailed nonlinear F100/MVC simulation resulted in the following conclusions.

7.2.1 The revised DIA algorithm has similar magnitude estimation errors compared to the baseline algorithm since the simplified nonlinear engine model steady state basepoints were not updated. However, by feeding back the actual values of low rotor speed (N1) and exhaust nozzle pressure (PT6) to the control integrators when there are no sensor failures, the effect of the estimation errors is eliminated. Improving the accuracy of the engine model steady state basepoints would reduce estimation errors, but these errors were retained in this program to allow an effective evaluation of the DIA algorithm revisions.

7.2.2 In general, detection, isolation and accommodation performance of the revised DIA algorithm was comparable to that of the baseline DIA algorithm. Improvements were obtained in the detection of hard failures of Fan Turbine Inlet Temperature (FTIT), due to improvements in the simplified engine model.

7.2.3 Both the revised and baseline DIA algorithms exhibited difficulties in detecting drifts in low and high rotor speeds (N1 and N2). Sizing of Kalman filter gain matrices results in a high weightings being placed on N1 and N2 speeds, even though a conscious effort was made for the revised DIA algorithm to reduce dependency on these dominant engine variables. As a result of this dependency, the filter tends to track these failed measurements and therefore makes it difficult to detect the failures. It is apparent that either further compromises must be made in sizing of the filter gain matrices, or alternative means to detect slow drift failures of these dominant parameters need to be incorporated in the DIA algorithm.

7.3 Microprocessor implementation requirements for the revised DIA algorithm were estimated at 19 msec for cycle time and 11K bytes of memory for an INTEL 8086 microprocessor.

7.4 Development of an improved simplified nonlinear F100 engine model for use in the DIA algorithm's filter resulted in the following conclusions.

7.4.1 Selecting flight operating points, at which to calculate linear models from the nonlinear simulation, based upon a criterion of a good spread of points on both Altitude/Mach Number and Total Pressure/Total Temperature envelopes, results in a good data base for developing good curve fits of model matrix elements.

7.4.2 The revised simplified nonlinear engine model provides significant improvements in dynamic accuracy over the previous model when compared to the detailed nonlinear simulation.

SECTION 8

RECOMMENDATIONS

8.1 The revised sensor failure detection, isolation and accommodation (DIA) algorithm, developed under this program, should be implemented on NASA Lewis Research Center's microprocessor system and operated with their hybrid simulation of the F100 engine to evaluate operation of the DIA algorithm in a real-time environment. As a part of this evaluation, it is recommended that the following areas be addressed to investigate problems identified in this program.

8.1.1 Evaluate adjustments to filter gains to reduce dependency on low and high rotor speeds (N1 and N2), such that detection of N1 and N2 drift failures will be improved.

8.1.2 Evaluate potential interaction problem between the filter and the Multivariable Control (MVC) mode as evidenced by fuel flow oscillations during the burner pressure (PT4) drift failure case.

8.1.3 Adjust simplified engine model steady state base points to be consistent with the F100 hybrid engine simulations steady state characteristics. Evaluate improvements in DIA performance resulting from improved steady state accuracy and resulting reduced estimation errors.

8.2 Subsequent to a hybrid simulation evaluation of the revised DIa algorithm implemented on NASA's microprocessor system, it is recommended that NASA conduct an engine test of the microprocessor-based DIA algorithm.

REFERENCES

1. Beattie, E. C., LaPrad, R. F., McGlone, M. E., Rock, S. M., Akhter, M. M., "Sensor Failure Detection System", NASA-CR-165515, August 1981.

2. DeHoff, R. L., Hall, W. E., Adams, R. J., and Gupta, N. K., "F100 Multivariable Control Synthesis Program -- Volume 1, Development of F100 Control System", AFAPL-TR-77-35, 1977.

3. DeHoff, R. L., Hall, W. E., Adams, R. J., and Gupta, N. K., "F100 Multivariable Control Synthesis Program -- Volume II, Appendices A through K", AFAPL-TR-77-35, 1977.

4. Miller, R. J. and Hackney, R. D., "F100 Multivariable Control System Engine Models/Design Criteria", Pratt & Whitney Aircraft Group, Government Products Division, AFAPL-TR-76-74, Nov. 1979.

5. Furnivel, G. M. and Wilson, Jr., R. W., "Regressions by Leaps and Bounds", Technometrics, 16(4) 1974, pages 499-511.

APPENDIX A

ADVANCED CONCEPT FOR DETECTING, ISOLATING, AND ACCOMMODATING SENSOR FAILURES IN GAS TURBINE CONTROL SYSTEMS

This appendix presents a detailed description of the advanced concept, developed under NASA Contract NAS3-22481, for detecting, isolating, and accommodating sensor failures in gas turbine engine control systems. The discussion is divided into the separate tasks of detection, isolation, and accommodation.

Detection

The detection scheme uses a simple threshold comparison check on the normal mode filter residuals to declare a hard failure. The Weighted Sum Square Residual (WSSR) test is used for soft failure detection. This technique uses filter innovations for decision making. The innovation sequence $\gamma(k)$ is white with known covariance if the model is perfect and there is no failure. In case of a failure the residual becomes

$$\gamma(k) = \text{white noise} + \text{effect of failure}$$

and the detector is used to identify the failure using a priori knowledge of white noise covariance and the new statistics. To detect a failure, one therefore has to compute the quantity $l(k)$ over the last N observations,

$$l(k) = \frac{1}{N} \sum_{j=k-N+1}^{k} \gamma(j)\, V^{-1}(j)\, \gamma(j)$$

where $V(j)$ is given by:

$$V(j) = H(j)\, P(j/j-1) H^{T}(j) + R$$

where $P(j)$ is the estimation error covariance of the state estimate $\hat{X}(j)$, $H(j)$ is the plant output matrix, and R is the measurement noise covariance matrix.

The quantity $l(k)$ is called the Weighted Sum Square Residual. For normal (nonfailure) operation, $l(k)$ is expected to remain small. However, in case of a failure, $l(k)$ will increase. If λ is the threshold value to make a decision between H_0 and H_1, we have

$$l(k) \begin{cases} < \lambda \text{ implies } H_0 \text{ true} \\ > \lambda \text{ implies } H_1 \text{ true} \end{cases}$$

The size of N and λ are design parameters, chosen to provide acceptable tradeoff between false alarms and misses.

Isolation

Isolation of soft failures is performed "off-line"; i.e., after the failure is detected, using a likelihood ratio test. Since M failure modes are hypothesized, M Kalman filters (bank of filters) are designed based on each failure mode. Each of the filters ignores one measurement and operates on the assumption that the channel containing the failure information has been ignored. When a failure occurs, the filter which ignores the failed channel stands out from all other filters and the likelihood ratio test is used to identify the failed channel filter.

The design parameters involved in this isolation process are the thresholds used to perform the likelihood ratio test. The techniques in Table A-1 can be used to select the threshold.

TABLE A-1

THRESHOLD SELECTION

Minimize Miss Probability for a Fixed False-Alarm Rate
Minimize Sum of Miss and False-Alarm Probabilities
Minimize the Bayes Risk

$$B = C_{00}\, P(H_0,H_0) + C_{01}\, P(H_0,H_1) + C_{10}\, P(H_1,H_0) + C_{11}\, P(H_1,H_1)$$

where

$P(H_i,H_j) = P_{Hi}\, P(H_j/H_i)$

H_i = hypothesis associated with failure mode i

C_{ij} = cost of accepting H_i when H_j is true

PH_j = a-priori probability that H_j is true

$P(H_i/H_j)$ = probability of accepting H_i given H_j is true

Accommodation

The normal mode filter serves as the accommodation filter for the no-failure case. In case of a hard failure, where the failure is detected and isolated simultaneously, the accommodation filter is reconfigured to eliminate the failed channel. One of the isolation filters which ignores the failed channel is used for this purpose. There may be small transients associated with switching filters. In case of soft failures, the normal mode filter provides estimates to the control logic while the failure is being isolated. After the isolation of the failure, the accommodation filter (the normal mode filter) is reinitialized and reconfigured using the "isolated" filter.

Once a failure has been detected and isolated, further tests for additional failures are performed on the accommodation filter. Each time a failure is isolated, the accommodation filter is reinitialized and reconfigured.

A detailed flow chart of this concept is shown in Figure A-1.

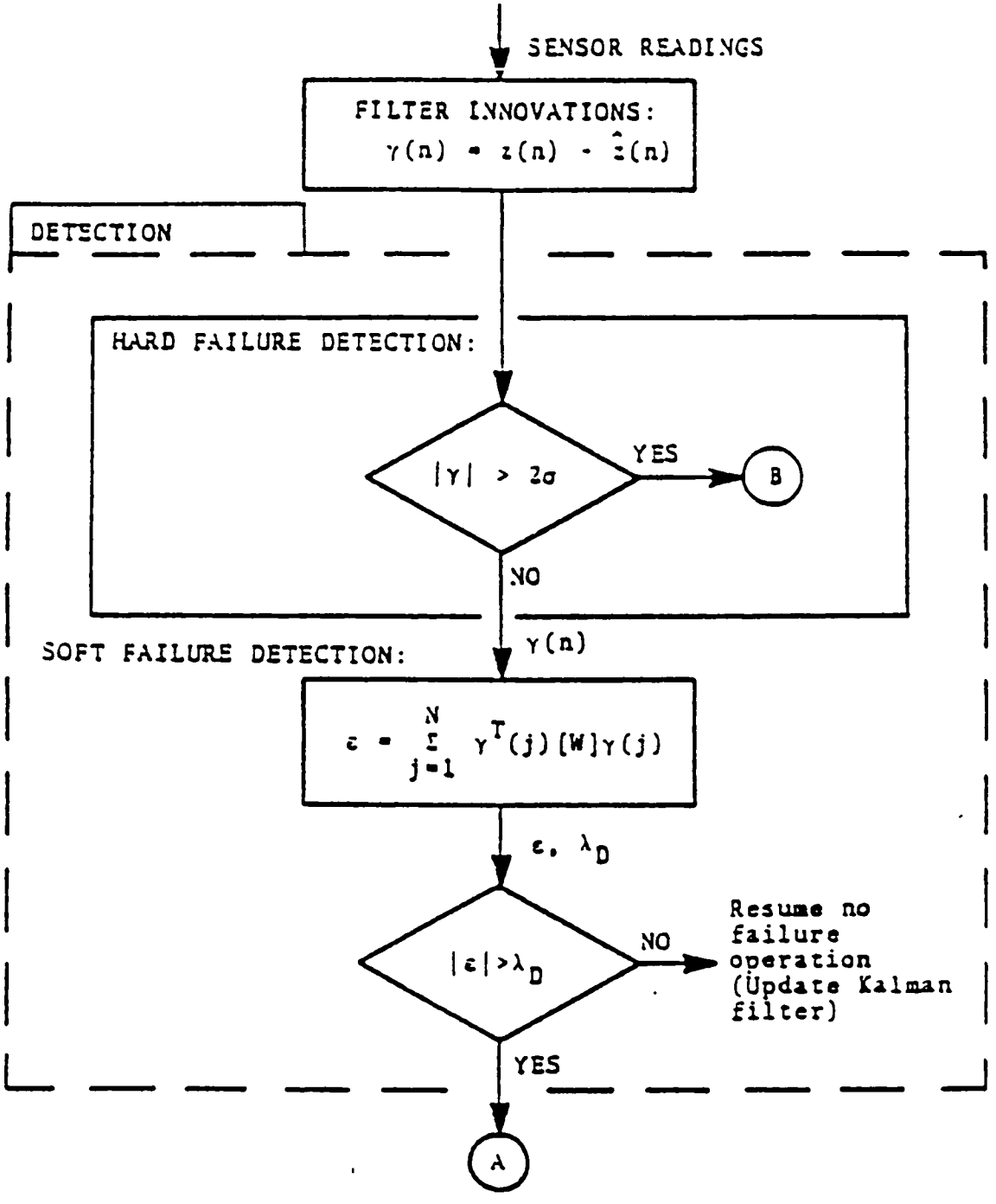

Figure A-1 Flow Chart of DIA Concept

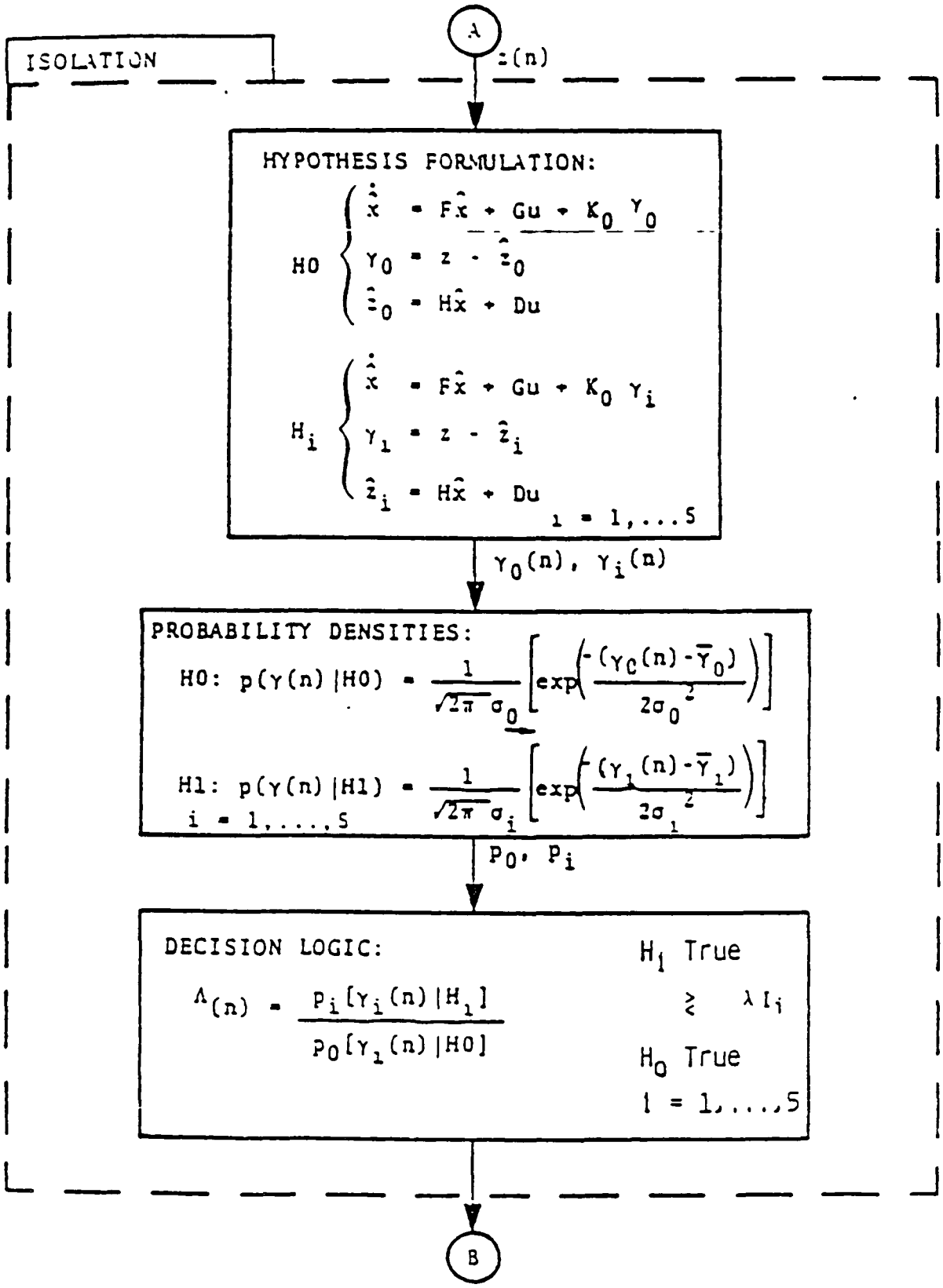

Figure A-1 Flow Chart of DIA Concept (Continued)

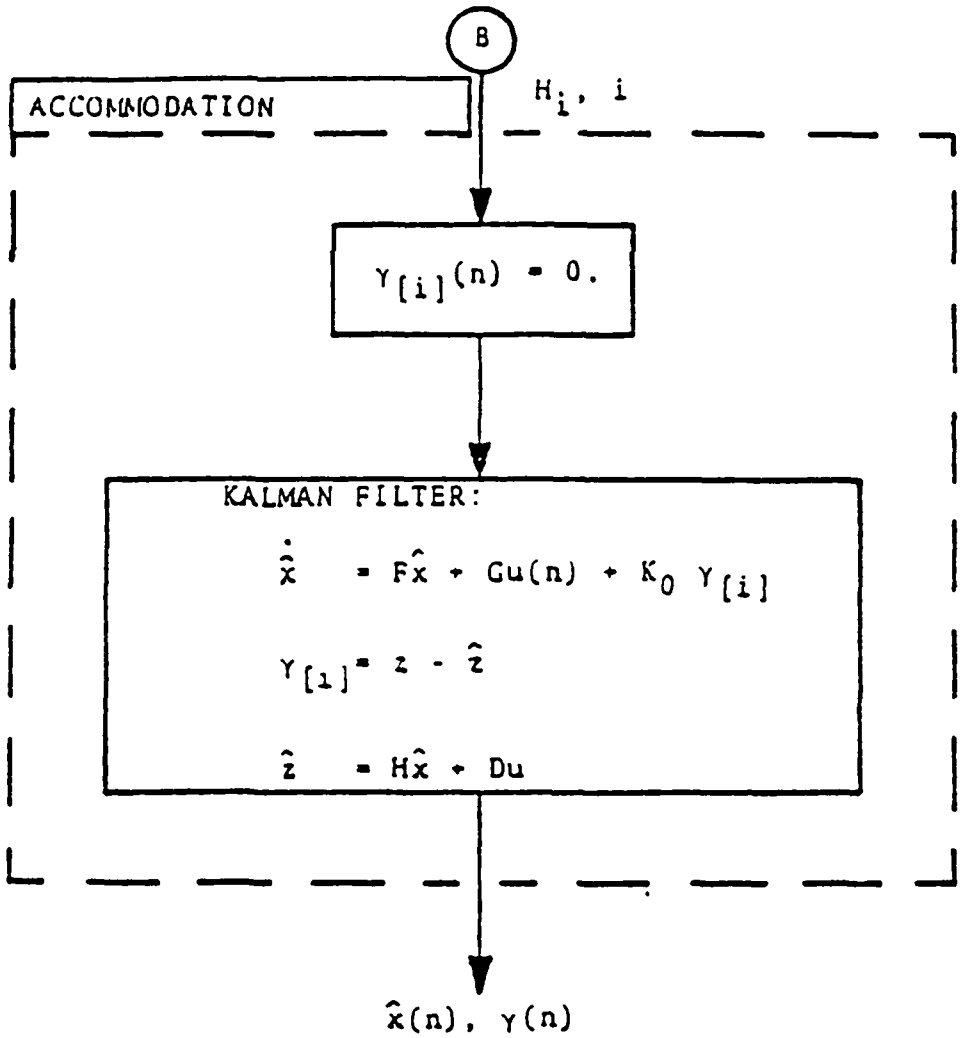

Figure A-1 Flow Chart of DIA Concept (Concluded)

DISTRIBUTION LIST

Adams, Milt 1
Airesearch Manufacturing Co.
402 S. 36 St. P.O. Box 5217
Phoenix, AZ. 85010

Aiken, William RJ-2 1
NASA Headquarters
Washington, D.C. 20546

Alexander, Bruno 1
General Electric Co.
1 Neumann Way
Cincinatti, OH 45215

Barron, Roger L. 1
General Research Corp.
7655 Old Springhouse Road
McLean, VA. 22102

Beale, Guy O. 1
Vanderbilt University
Box 1698, Station B
Nashville, TN 37235

Bortz, Alfred 1
Mellon Institute
4616 Henry Street
Pittsburgh, PA 15213

Bowditch, Dave 1
NASA Lewis Research Center
21000 Brookpark Rd. M.S. 86-1
Cleveland, OH 44135

Brown, Harold 1
General Electric - AEBG
552 Hickory Hill Lane
Cincinnati, OH 45215

Bruno, Roy 1
Advanced Technology Center
Allis-Chalmers
P.O. Box 512
Milwaukee, WI 53201

Burcham, Bill 1
NASA DFRC
P.O. Box 273
Edward, CA 93523

Burghart, James H. 1
Cleveland State University
Electrical Engineering Dept.
Cleveland, OH 44115

Caglayan, A. 1
Bolt, Beranek, and Newman, Inc.
50 Moulton Street
Cambridge, MA 02138

Carlin, Chris 1
Boeing Aerospace Co.
P.O. Box 3999
Seattle, WA. 98124

Cassidy, J. 1
General Electric Corp.
P.O. Box 43
Schenectady. NY 12345

Chen, C.S. 1
University of Akron
Akron, OH 44325

Cheng, L. 1
Mellon Institute
4616 Henry Street
Pittsburgh, PA 15213

Clark, Robert 1
University of Washington
311 E. E. Building FT-10
Seattle, WA 98195

Colladay, Ray R 1
NASA Headquarters
Washington, DC 20546

Cook, Gerald 1
Vanderbelt University
Nashville, TN 37240

Corley, Ralph 1
General Electric Company
Cincinnati, OH 45215

Cormier, D. 1
Davy McKee Corporation
6200 Oak Tree Blvd.
Cleveland, OH 44131

Devery, D. 1
NASA Langley Research Center
Hampton, VA 23665

Deyst, John 1
C. Stark Draper Lab., Inc.
68 Albany Street
Cambridge, MA 02139

Doeblin, E. 1
Ohio State University
206 W. 18 Avenue
Columbus, OH 43210

Donoughue, John 1
Cleveland State University
1983 E. 24 Street
Cleveland, OH 44115

Elliott, J.G. 1
Bendix Research Laboratories
Southfield, MI 48076

Erzberger, H. 1
NASA Langley Research Center
Hampton, VA 23665

Eterno, John 1
Scientific Systems, Inc.
54 Rindge Ave. Ext.
Cambridge, MA 02140

Facey, John RJP-2 1
NASA Headquarters
Washington, DC 20546

Fergurson, Roger 1
U.S. Army Applied Technology Labs.
Ft Eustis, VA 23604

Gai, Eli 1
C. Stark Draper Lab., Inc.
68 Albany Street
Cambridge, MA 02139

George, Edwin 1
General Research Corporation
7655 Old Springhouse Road
Mclean, VA 22102

Greenlee, Terry 1
Jaycor
P.O. Box 370 1401 Camino DelMar
Del Mar, CA 9 2014

Groumpos, Peter P. 1
Cleveland State University
1983 E. 24 Street
Cleveland, OH 44115

Gully, Sol W. 1
Alphatech
3 New England Execl. PK.
Burlington, MA 01803

Gupta, Narendra 1
Integrated Systems, Inc.
2 Palo Alto Square Suite 334
Palo Alto, CA 94304

Harrison, James 1
C. Stark Draper Lab., Inc.
68 Albany Street
Cambridge, MA 02139

Hatch, Robert A. 2
Garrett Turbine Engine
111 S. 34 Street
P.O. Box 5217
Phoenix, AZ 85010

Hermann, Wm. 1
Detroit Diesel Allison
P.O. Box 894
Indianapolis, IN 46206

Holt, Milt 1
NASA Langley Research Center
Hampton, VA 23665

Hudak, John 1
Mellon Institute
4616 Henry Street
Pittsburgh, PA 15213

Kerrebrock, Jack R 1
NASA Headquarters
Washington, DC 20546

Landingham, Hugh Van 1
Virginia Polytechnical Inst.
Blacksburg, VA 24061

Larimore, Wallace E. 1
Scientific Systems, Inc.
54 Rindge Ave. Ext.
Cambridge, MA 02140

Leros, Paul 1
Cleveland State University
1983 E. 24 Street
Cleveland, OH 44115

Levin, Jack RJH-2 1
NASA Headquarters
Washington, DC 20456

Lodaya, Mike 1
Bendix Energy Controls Div.
717 N. Bendix Drive
South Bend, IN 46620

Loparo, Ken 1
Case Western Reserve University
Cleveland, OH 44106

Madiwali, Appa 1
1150 McBride Avenue
Little Falls, NJ 07424

Mark, Herman 1
NASA Lewis Research Center
21000 Brookpark Rd. M.S. 77-1
Cleveland, OH 44135

Marvin, Mason 1
General Electric Company
1 Neumann Way
Cincinnati, OH 45215

McIver, Duncan RTH-6 1
NASA Headquarters
Washington, DC 20456

McLain, Richard 1
Detroit Diesel Allison
P.O. Box 894
Indianapolis, IN 46206

Mehra, Raman 1
Scientific Systems, Inc.
54 Rindge Ave. Ext.
Cambridge, MA 02140

Meissner, Charles W. 1
NASA Langley Research Center
M.S. 477
Hampton, VA 23665

Merrill, Walt 35
NASA Lewis Research Center
21000 Brookpark Road M.S. 100-1
Cleveland, OH 44135

Montgomery, Ray 1
NASA Langley Research Center
M.S. 152A
Hampton, VA 23665

Mulukutla, A.R. 1
General Electric Company
M/D H-42
Evendale, OH 45215

Myers, Larry 1
NASA Dryden FRC
P.O. Box 273
Edwards, CA 93523

Niessen, Frank 1
Hamilton Standard
M.S. 1A-3-2
Windsor Locks, CT 06096

Osani, Joe 1
General Electric
Box 81186
Cleveland, OH 44181

Peczkowski, Joe 1
Bendix Energy Controls Div.
717 N. Bendix Drive
South Bend, IN 46620

Powers, William F. 1
Ford Motor Company
P.O. Box 2053
Dearborn, MI 48121

Przybylko, Steve 1
Bendix Energy Controls Division
717 N. Bendix Drive
South Bend, IN 46620

Railey, Malcolm 1
University of Akron
2918 Bancroft
Akron, O H 44313

Rock, Steve 1
Systems Control Technology
1801 Page Mill Road
Palo Alto, CA 94303

Rosen, Cecil RTP-6 1
NASA Headquarters
Washington, DC 20456

Roth, Stephen P. 1
Pratt & Whitney Aircraft
M.S. B173
West Palm Beach, FL 33408

Sain, Mike 1
Notre Dame University
South Bend, IN 46556

Scott, Ronald 1
United Technology Research Corp.
W. Palm Beach, FL 33408

Skira, C. 1
AFWAL/POTC
Wright Patterson AFB, OH 45433

Slater, Gary 1
University of Cincinnati
Cincinnati, OH 45221

Small, Les 1
AFWAL/POTC
Wright Patterson AFB, OH 45433

Spang, Austin 1
General Electric Corporation
P.O. Box 43
Schenectady, NY 12345

Stewart, James 1
NASA Dryden FRC
E-EDC
Edwards, CA 93523

Stone, C.R. 1
Honeywell
M.S. A2340
2600 Ridgeway Road
Minneapolis, MN 55413

Swick, Robert 1
Detroit Diesel Allison
P.O. Box 894
Indianapolis, IN 46206

Szalai, Ken 1
NASA Dryden FRC
E-EDC
Edwards, CA 93523

Thomas, Allen 1
Union Carbide Corporation
Greenville, SC 29606

Tylee, J. Louis 1
EG&G Idaho, Inc.
P.O. Box 1625
Idaho Falls, ID 83415

VanderVelde, Wallace 1
M I T
77 Massachusetts Ave.
Cambridge, MA 02139

Vizzini, Russ 1
Naval Air Propulsion Center
PE-43
Trenton, NJ 08628

Walker, Bruce K. 1
M I T
77 Massachusetts Avenue
Cambridge, MA 02139

Warner, Dennis 1
Detroit Diesel Allison
P.O. Box 894
Indianapolis, IN 46206

Wells, Bill 1
Wright State University
Dayton, OH 45235

Willsky, Alan 1
M I T
77 Massachusetts Avenue
Cambridge, MA 02139

1. REPORT NO. NASA CR-168190	2. GOVERNMENT AGENCY	3. RECIPIENT'S CATALOG NO.
4. TITLE AND SUBTITLE SENSOR FAILURE DETECTION FOR JET ENGINES		5. REPORT DATE May 1983 6. PERFORMING ORG. CODE
7. AUTHOR(S) E.C.Beattie (PWA-CPD), R.F.LaPrad (PWA-CPD) S.M.Rock (SCT), M.M.Akhter (SCT)		8. PERFORMING ORG. REPT. NO. PWA 5891-18
9. PERFORMING ORG. NAME AND ADDRESS United Technologies Corporation Pratt & Whitney Aircraft Group Commercial Engineering		10. WORK UNIT NO. 11. CONTRACT OR GRANT NO. NAS3-23282
12. SPONSORING AGENCY NAME AND ADDRESS National Aeronautics and Space Administration Lewis Research Center 21000 Brookpark Road, Cleveland, Ohio 44135		13. TYPE REPT./PERIOD COVERED Contractor Final Report 14. SPONSORING AGENCY CODE

15. SUPPLEMENTARY NOTES
Project Manager: Dr. Walter Merrill, NASA-Lewis Research Center, Cleveland, Ohio 44135

16. ABSTRACT

Revisions to the Advanced Sensor Failure Detection, Isolation, and Accommodation (DIA) algorithm, developed under the "Sensor Failure Detection System" program (NAS3-22481), were studied during this program to eliminate the steady state errors due to estimation filter biases. Three algorithm revisions were formulated and a selection process led to choosing one revision for detailed evaluation. The selected version modifies the DIA algorithm to feedback the actual sensor outputs to the integral portion of the control for the no-failure case . In case of a failure, the estimates of the failed sensor output is fed back to the integral portion. The estimator outputs are fed back to the linear regulator portion of the control all the time. The revised algorithm was evaluated and the results compared to the "baseline" algorithm developed under the previous contract.

17. KEY WORDS (SUGGESTED BY AUTHOR(S))	18. DISTRIBUTION STATEMENT		
Sensors, Failure Detection, Failure Isolation, Failure Accommodation, Filtering Techniques, Kalman Filters, Linear Modeling	UNCLASSIFIED - UNLIMITED 38		
19. SECURITY CLASS (THIS REPT) Unclassified	20. SECURITY CLASS (THIS PAGE) Unclassified	21. NO. PGS	22. PRICE *

* For sale by the National Technical Information Service, Springfield, VA 22161

FOREWORD

This document was prepared by United Technologies Corporation, Pratt & Whitney Aircraft Group, Commercial Products Division, and Systems Control Technology (SCT), Inc., to meet the requirements for a Final Report under NASA Contract NAS3-23282, Sensor Failure Detection System.